Thesis

Magneto-optical spectroscopy of epitaxial graphene

CRASSEE, Iris

Abstract

In this thesis we experimentally study the infrared magneto-optical properties of single and multilayer epitaxial graphene grown on a SiC substrate. Which is a promising material due to the scalability of the production method. However, graphene grown on SiC is also very complex, due to grain boundaries, wrinkles and in the case of multilayer graphene a twisted stacking. The optical experiments reveal a giant Faraday rotation in highly doped single layer graphene of several degrees. The spectra also show clear evidence for plasmonic and magnetoplasmonic excitations. From the transmission and Faraday rotation spectra the optical conductivity and a.c. Hall conductivity – the optical analogue of the d.c. Hall conductivity – are obtained, respectively.

Reference

CRASSEE, Iris. *Magneto-optical spectroscopy of epitaxial graphene*. Thèse de doctorat : Univ. Genève, 2013, no. Sc. 4572

URN : urn:nbn:ch:unige-291903

UNIVERSITÉ DE GENÈVE
Département de Physique
de la Matière Condensée

FACULTÉ DES SCIENCES
Directeur de Thèse : A. B. Kuzmenko
Co-directeur de Thèse : D. van der Marel

Magneto-Optical Spectroscopy of Epitaxial Graphene

THÈSE

présenté à la Faculté des Sciences de l'Université de Genève
pour obtenir le grade de docteur ès Sciences, mention physique

par

Iris Frederike Juliette Crassee
de
Amstelveen (The Netherlands)

Thèse n° 4572

GENÈVE
Atelier de reproduction de la Section de Physique
2013

UNIVERSITÉ DE GENÈVE

FACULTÉ DES SCIENCES

Doctorat ès sciences
Mention physique

Thèse de *Madame Iris Frederike Juliette CRASSEE*

intitulée :

" Magneto-Optical Spectroscopy of Epitaxial Graphene "

La Faculté des sciences, sur le préavis de Messieurs A. KUZMENKO, docteur et directeur de thèse (Département de physique de la matière condensée), D. VAN DER MAREL, professeur ordinaire et codirecteur de thèse (Département de physique de la matière condensée), A. MORPURGO, professeur ordinaire (Département de physique de la matière condensée), A. PIMENOV, professeur (Institute of Solid State Physics, Vienna University of Technology, Vienna, Austria) et F. GUINEA, professeur (Instituto de Ciencia de Materiales de Madrid, Consejo Superior de Investigaciones Científicas, Madrid, España), autorise l'impression de la présente thèse, sans exprimer d'opinion sur les propositions qui y sont énoncées.

Genève, le 22 mai 2013

Thèse - 4572 -

Le Doyen, Jean-Marc TRISCONE

N.B.- La thèse doit porter la déclaration précédente et remplir les conditions énumérées dans les "Informations relatives aux thèses de doctorat à l'Université de Genève".

Abstract

English

Graphene, a monoatomic layer of carbon atoms arranged in a honeycomb lattice, was successfully isolated for the first time in 2004. Fueled by the exotic electronic and optical properties of this material, the scientific field of graphene research has exploded. Many of those exotic properties are a direct consequence of the relativistic, massless and chiral character of the charge carriers, the so-called Dirac fermions. Therefore, the monoatomic layer forms a solid-state playground to study quantum electrodynamics (QED), where the carriers follow the physics of QED, but at the convenient speed of 300 times smaller than the speed of light. In an externally applied magnetic field an anomalous Hall effect can be observed, due to the non-trivial Berry's phase. The electronic bands split up into Landau levels with a square-root dependence on magnetic field, unique for Dirac fermions.

Apart from the exciting possibilities to study relativistic physics in a solid, graphene also has many promising aspects for future technologies. It is the strongest known material and can withstand deformations up to $\sim$20%. The charge carrier mobilities found in graphene are remarkably high. Although they vary somewhat from sample to sample, mostly depending on the production method of the sample, mobilities of more than 200,000 $cm^2V^{-1}s^{-1}$ were reported. With the use of an electrostatic gate the ambipolar carrier density can be tuned, which opens up possibilities for switchable or tunable electronics. Also the optical properties of graphene attract attention for future applications. Importantly, it is transparent, offering possibilities to use it for transparent and flexible electrical contacts. With a gate the optical properties like absorption of light can be tuned. Moreover, due to its two dimensional character strong matter-light interactions and a high plasmon confinement are observed, in combination with the tunability, graphene offers a large potential for the fields of plasmonics and opto-electronics.

In this thesis we experimentally study the infrared magneto-optical properties of these ultimately thin films. The type of graphene investigated is single and multilayer epitaxial graphene grown on a SiC substrate. Which is a promising material due to the scalability of the production method. However, graphene grown on SiC is also very complex, due to grain boundaries, wrinkles and in the case of multilayer graphene a twisted stacking.

Many questions remain about the electronic structure and for instance the influence of stacking and of the growth process on its properties.

The experiments reveal a giant Faraday rotation in highly doped single layer graphene of several degrees. The spectra also show clear evidence for plasmonic and magnetoplasmonic excitations. From the transmission and Faraday rotation spectra the optical conductivity and a.c. Hall conductivity – the optical analogue of the d.c. Hall conductivity – are obtained, respectively. We study these collective modes using an effective medium approach and evaluate our results to existing theoretical calculations. Due to the high doping of single layer epitaxial graphene, the cyclotron resonance observed for magnetic fields up to about 10 T is semi-classical with a linear dependence on magnetic field. To probe individual Landau level excitations with a square-root dependence on magnetic field, typical for Dirac fermions, much higher magnetic fields are needed. In order to observe the crossover between the semi-classical cyclotron resonance and the quantized Landau level transitions, we performed transmission measurements in magnetic fields up to 32 T. These transmission spectra are analyzed using the Drude-Lorentz formalism for the magneto-optical conductivity. The results are discussed in the light of the effective single particle model. Finally, we study magneto-optical spectra of low doped multilayer epitaxial graphene. Due to the multilayer character of these samples both semi-classical cyclotron resonance and transitions between Landau levels can be observed simultaneously in the spectra. With the use of the Faraday rotation we can disentangle the contributions of electron- and hole-like charge carriers to the optical response. The spectra are analyzed using a multi-component Drude-Lorentz model. A clear discrepancy is found between our results and the picture of multilayer graphene as a stack of isolated monolayers.

Français

Le graphène, une couche monoatomique d'atomes de carbone ordonné sous forme de maille de nid d'abeille, a été isolé pour la première fois avec succès en 2004. Stimulé par les propriétés électroniques et optiques exotiques, le domaine de recherche sur le graphène a connu un engouement soudain. Beaucoup de ces propriétés découlent directement du caractère relativiste, de sa masse effective nulle et de la chiralité de ses porteurs de charge, communément appelé fermions de Dirac. En conséquence, cette monocouche atomique forme un terrain d'étude dans la physique de solide pour étudier l'électrodynamique quantique (EDQ), où les porteurs de charge obéissent aux lois de l'EDQ mais leur vitesse est 300 fois in-

férieur à celle de la lumière. Sous l'influence d'un champ magnétique externe un effet Hall quantique anormale est observé, dû à la phase de Berry non-triviale. Les bandes électroniques se séparent en niveau de Landau avec une dépendance en racine carré du champs magnétique, typique pour des fermions de Dirac.

En plus de pouvoir étudié la physique relativiste dans un solide, le graphène peut déboucher dans de nouvelles futures applications. C'est le matériaux le plus résistant connu et peut supporter des déformations jusqu'à 20%. Les mobilités des porteurs de charge sont très élevées. Même si elles varient entre diffèrent échantillons des mobilités de 200 000 $cm^2V^{-1}s^{-1}$ ont été observées. Grâce à l'utilisation d'une grille électrostatique les porteurs de charge ambipolaire peuvent être modifiés, ce qui permet des applications électroniques commutable et modifiable. Les propriétés optiques du graphène sont également intéressantes en vue de futures applications. Sa transparence peut aider à la réalisation d'électrode transparente et flexible. Avec la grille il est également possible de modifié les propriétés optiques tel que l'absorption. De plus, à cause de son caractère bi-dimensionnel des fortes interactions lumière/matière et un fort confinement de plasmon sont observés qui en combinaison avec ses propriétés ajustables offre un large potentiel d'application dans le champs de la plasmonique et l'opto-électronique.

Dans cette thèse nous étions expérimentalement les propriétés magnéto-optiques infrarouges de ces couches minces. Les échantillons de graphène mesurés sont des monocouches et des multicouches épitaxiés sur SiC qui est une méthode de croissance prometteuse dû au fait quelle peut être appliqué à des grandes quantités. La structure du graphène sur SiC est néanmoins très complexe à cause des joints de grain, la rugosité de la surface et, dans le cas des multicouches, l'empilement torsadé. Des questions restent ouvertes par rapport à la structure électronique et l'influence de l'empilement et du processus de croissance.

Nous montrons dans nos expériences une rotation Faraday géante, de plusieurs degrés, dans des échantillons fortement dopés. Les spectres démontrent aussi clairement la présence d'excitation plasmonique et magnéto-plasmonique. Avec les spectres de transmission et de rotation Faraday les conductivités optiques et la conductivité Hall CA - en analogie à la conductivité Hall CD - sont extraites. Nous étudions ces modes collectifs en utilisant une approche de milieu effectif et comparons nos résultats à des calculs théoriques existants. À cause du fort dopage la résonance cyclotron jusqu'à 10 T est de nature semi-classique avec une dépendance linéaire en champs. Pour étudier les excitations entre niveau de Landau avec une dépendance en racine carré, des champs beaucoup plus intenses sont nécessaires. Pour observer la transition entre le régime

semi-classique et quantique nous mesurons la transmission en champs magnétique jusqu'à 32 T. Les spectres sont analysés à l'aide du formalisme Drude-Lorentz pour obtenir la conductivité magnéto-optique. Les résultats sont interprétés en terme d'une représentation de particule effective unique. Finalement, nous nous penchons sur les spectres magnéto-optiques de multicouces faiblement dopées. Dans ce cas nous observons les transitions semi-classiques (résonance cyclotron) et les transitions quantiques entre niveaux de Landau. La rotation Faraday permet d'identifier les contributions électrons et trous dans la réponse optique du matériau. Les spectres sont analysés avec une approche Drude-Lorentz à multi-composante. les résultats sont en désaccord avec la représentation de ces échantillons les considérant comme un empilement de monocouches isolés.

Contents

1

Introduction

1.1 Graphene propelled into the limelight

Using tools as simple as scotch tape, tweezers and, most likely, a pair of gloves, back in 2004, Konstantin Novoselov and Andre Geim isolated a much sought after material [1]. This material, graphene, was already well-known due to an early theoretical interest in its exotic properties or simply as a building block of graphite [2]. Simultaneously, other groups were searching for ways of producing these single layers of carbon atoms using more involved methods like the graphitization of SiC [3]. However, it was the incredibly easy to use and inexpensive scotch-tape technique that propelled graphene, together with its discoverers, into the scientific limelight.

Graphene is a one atom thick crystal of carbon atoms arranged in a honeycomb structure and forms the building blocks of graphite. It can be separated from graphite because the Van der Waals force between the layers in graphite is much weaker than the in plane covalent bonds. Novoselov and Geim were the first to exfoliate one single layer and therefore the first to successfully isolate a truly two-dimensional (2D) material [1], gaining them the Nobel Prize in 2010.

The reasons for the enormous scientific interest in graphene are of both practical and fundamental origin. The practical reason is the everlasting search for smaller and faster electronic devices. The first steps towards technological implementation were immediately made by Novoselov and Geim, who reported an electric-field effect in graphene [1], fundamental for future applications. Soon after the first theoretical [4–7] and experimental [8,9] reports of a tunable band gap in Bernal stacked bilayer emerged (layers are rotated by 60° with respect to each other). In addition, it was shown that strips of graphene of a few nanometers, much smaller than typical silicon-based devices, can be used as a transistor [10]. More recently, graphene attracted the attention

as a novel optoelectronic and plasmonic material for applications ranging from the terahertz to the visible spectral range [11–25]. One expects that plasmon waves can be squeezed into a much smaller volume [21, 23] than in noble metals routinely used in plasmonics and can also be manipulated by an external gate voltage.

Apart from the promising future of graphene for technological applications, the first truly 2D crystal proves to be a play garden to probe relativistic physics in a solid. In 1946, P. R. Wallace was the first to study the band structure of graphene and demonstrate the unusual semi metallic behavior [2]. This study was a starting point to study graphite (important for nuclear reactors in the post-World War time). About ten years later, the Slonczewski-Weiss-McClure model was proposed, which provides a description of the electronic properties in this material [26, 27]. Altogether, before 2004 numerous theoretical studies already appeared highlighting the unusual physics found in a monoatomic layer of carbon (e.g. [28–30]). The large interest in graphene was sparked by the prediction that the low energy dispersion is linear and therefore its low-energy excitations are massless, chiral Dirac fermions [31]. In neutral graphene, the chemical potential crosses exactly the Dirac point. The low energy dispersion resembles the physics of quantum electrodynamics (QED) for massless fermions except for the fact that the Dirac fermions in graphene move with a speed v_F, which is 300 times smaller than the speed of light c [32–34]. Therefore many of the unusual properties of QED can be observed in graphene but at v_F instead of c.

Indeed using angle-resolved photoelectron spectroscopy on single layer epitaxial graphene, the energy dispersion was revealed to be linear, and therefore the quasiparticles to be Dirac-like [35, 36]. Due to this linear band dispersion at zero magnetic field, the optical conductivity of neutral graphene at zero temperature is universal over a broad energy range [30,37–40], therefore also the absorption is constant and is simply proportional to the number of layers. Altogether optical studies played a major role in determining the properties of graphene: these studies revealed the effects of an external electric field on the doping [41, 42] and showed the opening of a band gap in Bernal stacked bilayer by an external electric field [41, 43, 44].

1.2 Graphene in a magnetic field

When placed in a magnetic field the Dirac fermions lead to new physical phenomena [45, 46] such as the anomalous integer quantum Hall effect (IQHE) measured experimentally [47, 48], a trademark of Dirac fermion behavior and a direct consequence of the presence of a Landau level at zero energy. Importantly, the IQHE in graphene can be observed at room temperature due to the large cyclotron energies of relativistic electrons [49].

Experiments measuring cyclotron resonance played an important role in determining the fundamental properties of many materials. In 1955 the first measurements were performed to determine the cyclotron masses of Si and Ge [50]. Later on, the line shape of the cyclotron resonance was used to study scattering mechanisms in for ex-

ample 2D electron gasses [51,52]. Magneto-optical studies of the cyclotron resonance transitions were the first to reveal the typical non-equidistant Landau levels with their square-root dependence on field observed in low-doped graphene [53–55]. From these experiments the Fermi velocity of the charge carriers could be extracted. The square-root dependence of the Landau levels on field was confirmed by scanning tunneling microscopy [56,57]. Using magneto-optical spectroscopy, research groups addressed electron-hole asymmetry [55], the possible existence of a band gap [58], scattering mechanisms [59] and the coupling of cyclotron resonance to the K-phonon [60].

1.3 Epitaxial graphene on SiC

The size of the samples produced by the scotch tape technique used by Novoselov and Geim are typically of the order of a few micrometers, rarely samples oof the order of 1 mm were found [61]. Although the technique is inexpensive and offers a relatively easy way to produce graphene, an industrial production of scalable samples is not feasible for this method. Thence other methods to isolate of grow graphene are actively explored. Alternative techniques include chemical vapor deposition (CVD) of graphene on metal films [62–66], the unzipping of carbon nanotubes [67] and the sonication of graphite in a liquid [68].

A different synthesis method is the thermal decomposition of SiC, which results in epitaxial layers of carbon on top of the insulating substrate [3, 69, 70]. The SiC substrate itself is a polar material which can be terminated by a carbon face or by a silicon face. The sample properties of graphene grown on the carbon face differ from the layers grown on the silicon face. The graphitization of the carbon face often leads to multilayer graphene [3], while on the silicon face, the growth of each subsequent layer is controlled by temperature, allowing for a more precise control over the layer thickness [69,70]. Surprisingly, each carbon layer grown on the C-side shows the typical properties of isolated single layer graphene (crossing π bands). Layers grown on the Si-side of SiC however, show a very different behavior. The carbon layer closest to the substrate forms an insulating 'buffer layer', the properties of the second layer correspond to the ones of single layer graphene, while subsequent layers are typically Bernal stacked, which drastically changes the electronic structure [70]. The buffer layer is a result of coupling between dangling bonds in the silicon terminated surface of the SiC and the carbon atoms. However these bonds can be passivated by the intercalation of hydrogen between buffer layer and substrate, effectively transforming the buffer layer into a graphene layer [71,72].

Due to the vicinity of the polar SiC, the Dirac point in the graphene layers close to the substrate is shifted away from the Fermi energy. In graphene grown on the C-face the layers close to SiC are generally electron doped, as is graphene on a buffer layer on the Si-face of SiC [73–75]. In contrast, hydrogen intercalated graphene on the Si-face generally shows a large hole doping [71,76]. In the case of multilayer graphene on the C-face, the outmost layers are close to neutral doping.

Clear advantages of graphene grown on SiC are the scalability of the samples and the direct growth on an insulating substrate, evading extra transfer steps, which compromise the quality of the graphene surface. The doping level of the graphene can be tuned by, for example, the absorption of molecules [8, 77] or by the application of a (top) gate [78, 79].

As was already mentioned, the layers in multilayer epitaxial graphene grown on the C-face of SiC show the Dirac like properties typical for isolated single layer graphene. Landau level spectroscopy performed on this type of graphene revealed a square-root dependence of the Landau levels on magnetic field expected for monolayer graphene [53]. In contrast, the Landau levels in Bernal stacked bilayer graphene show a distinctly different magnetic field dependence [80, 81]. This monolayer behavior was later confirmed by scanning tunneling microscopy measurements [57,82]. In addition, a Berry's phase of π and antilocalization was observed in transport measurements [83, 84]. Finally, angle-resolved photo emission spectroscopy showed that the band structure of the individual layers is indeed Dirac-like [85].

The reason for the apparent single layer behavior in epitaxial multilayer graphene is thought to be a twisted, non-Bernal, stacking of the layers, which effectively decouples the layers [86]. Consequently, multilayer epitaxial graphene on the C-side of SiC is often thought of as a stack of independent graphene layers with a band structure resembling the one of isolated monolayer graphene. The influence of the twisted stacking on the electronic structure received a lot of attention and much theoretical progress was booked [4, 87–94]. It was predicted that in twisted multilayers the effect of the interlayer interaction is to decrease the Fermi velocity with respect to the Fermi velocity in isolated monolayer graphene [88,90,91], which was indeed observed experimentally in rotationally stacked bilayer graphene [95].

1.4 Magneto-optical spectroscopy on epitaxial graphene

In this work we study the magneto-optical properties of graphene, and in particular of single and multilayer epitaxial graphene grown on SiC. The epitaxial graphene samples are provided by the group of Dr. Seyller[1]. Importantly, several elements of the experimental techniques used for this work make our magneto-optical measurements unique in the field of graphene research:

- Spectroscopic measurements of the rotation of polarization of light passing through epitaxial graphene in a magnetic field, known as the Faraday effect, are performed. Faraday rotation reveals the sign of the charge carriers involved in the various optical transitions, so that it can be thought of as an optical analogue to the d.c. Hall effect. From the Faraday rotation spectra we extract the optical Hall conductivity. The Faraday rotation spectra are complemented with transmission

[1]The samples were produced by the group of Prof. Seyller at the Universität Erlangen-Nrnberg, the group recently moved to the Technische Universitt Chemnitz.

spectra, from which we extract the diagonal optical conductivity. The simultaneous measurement of the diagonal and Hall conductivity allows for precise analysis of the optical properties.

- Often in magneto-optical studies only the ratios between transmission spectra at finite magnetic field and zero-field are obtained, providing information about relative changes. With our experimental method, we are able to perform precise measurements of the transmission, from which we extract the absolute diagonal optical conductivity at every field, allowing an in-dept analysis of the optical spectra.

The manuscript is organized as follows: in Chapter 2 we briefly review some theory of optical spectroscopy and specifically discuss magneto-optics on thin films. In the last part of the chapter the experimental methods are presented. Chapter 3 is devoted to a more thorough introduction of the electronic and optical properties of graphene, both for B=0 T and for an externally applied magnetic field. Among other, we discuss cyclotron resonance in highly doped graphene, the quantized Landau levels in weakly doped graphene. Next, we show how the charge carrier concentration of a graphene sample can be determined from the optical spectra and how optics can be used to obtain the layer thickness of a multilayer sample. The synthesis of graphene and more specifically, of the samples used for the optical studies, epitaxial graphene on SiC, is described in the last part of Chapter 3.

In the remaining part of the thesis, starting from Chapter 4, we present the results of the experimental work. In Chapter 4 we concentrate on highly doped single layer graphene grown on the silicon side of SiC and the results of transmission and Faraday rotation measurements in fields up to 7 T. Faraday rotation measurements usually only reveal relevant rotation angles for macroscopically thick samples. Up until our experiments on single layer graphene, the thinnest structures showing measurable Faraday angles were several nanometer thick two-dimensional electron gases [96]. Therefore, we start by presenting the surprising results of these pioneering Faraday rotation measurements carried out on a monoatomic thin graphene layer. Next, we discuss the diagonal and Hall magneto-optical conductivity in the THz range, clearly showing quasi-classical cyclotron resonance. The sign and value of the doping is determined from the Hall conductivity and pronounced optical features caused by the surface morphology are identified as plasmons and magneto-plasmons.

In Chapter 5 we present transmission spectra of highly doped single layer graphene grown on the silicon side of SiC in magnetic fields up to 32 T. The high doping of the sample combined with high magnetic fields allow for the observation of the crossover between classical cyclotron resonance to the quantum regime where optical transitions between the individual low index Landau levels are observed. Precise analysis of the absolute optical spectra is performed and used to study the renormalization of the Drude spectral weight by many body interactions, predicted and observed previously in other studies [97–100].

In the last chapter of this thesis, Chapter 6, we present transmission and Faraday rotation measurements on multilayer epitaxial graphene grown on the carbon face of SiC. A detailed analysis of the optical spectra is performed, from which the doping levels and the sign of the doping is extracted. Due to the importance of the twisted stacking of the layers, magneto-optical spectroscopy has a clear advantage over surface probes, such as angle resolved photo emission and scanning tunneling microscopy, since the optical spectra contain contributions from all graphene layers. Results on two samples with different layer number are discussed. Multiple components are identified in the spectra, including quasi-classical cyclotron resonance, from a highly doped graphene layer closest to SiC and transitions between Landau levels coming from weakly doped layers. The Faraday rotation spectra facilitate the identification of coexisting electron and hole-like Landau level transitions and reveals an electron-hole asymmetry of the Fermi velocity. A detailed analysis of the optical intensity of the Landau level transitions is given.

2

Optical spectroscopy

2.1 Introduction

Optical phenomena in nature, like rainbows, the blue sky, halos near the sun or moon and Fata Morganas have fascinated many throughout the centuries. In the recent century this fascination had been turned into active employment of light: it has become an important experimental probe to extract information about the physical properties of materials in a non-invasive way. Well-known experiments from which the frequency dependent properties of the material can be obtained include reflection, transmission, ellipsometry and Raman scattering measurements. Optical experiments can be performed from the terahertz range to the ultraviolet, covering different properties of – and excitations in – the material, depending on their energy scale. External parameters such as electric and magnetic fields, temperature and pressure can be applied and changed during the optical experiment in order to study their effect on the optical excitations. In particular, a (perpendicularly) applied external magnetic field breaks the time-reversal symmetry of the system, in which case the so-called Faraday rotation of the polarization state of the light can be observed. Measurements off the Faraday effect form an important part of this thesis work.

In this chapter we briefly review the interaction of light with a material and the material properties describing the optical response using Maxwell's equations. The optical conductivity, as well as the dielectric function and its relation to the refractive index are discussed. We proceed with the classical Drude-Lorentz model for the optical response of a solid, both with and without an externally applied magnetic field. Thereafter, we discuss the Kubo-Greenwood formalism, derived from quantum mechanics.

The second part of this chapter, section 2.3, is aimed at connecting the fundamental

optical properties of thin 2 dimensional films, discussed in section 2.2, to experimental parameters, such as transmission. The Fresnel equations will be used to derive several relations to extract the real and imaginary parts of the optical conductivity of a thin film on a substrate from the transmission spectra obtained in an optical experiment. In the same sections we present the experimental techniques to obtain the transmission spectra. In the last section, the Faraday rotation of the polarization state of light and its direct relation to the optical Hall conductivity, as well as the experimental technique to obtain Faraday rotation spectra will be discussed.

Additional information on the subject of optical properties of solids can be found in many books and manuscripts, including Refs. [101–104].

2.2 (Magneto-) Optical properties of solids

In this section we will discuss briefly the interaction of light with solids, starting from the Maxwell equations, which describe how charges and currents act as a source of electric and magnetic fields. The propagation of the field inside the medium is found to depend on the material specific refractive index. The refractive index is directly related to the dielectric function and the conductivity of the material.

In subsection 2.2.2 the classical Drude-Lorentz model to describe the optical conductivity is introduced. The model consists of a sum of Lorentz oscillators, each one at a specific energy, with a specific width and broadening and, in the case that a finite external magnetic field is present, a particular cyclotron resonance energy.

After the introduction of these macroscopic and classical models we will briefly review the Kubo-Greenwood formula, which provides a microscopic, quantum mechanical description for the optical conductivity. Here we will concentrate the discussion on the 2-dimensional case, valid for thin films. The Kubo-Greenwood formula is based on linear response theory and provides a route to qualitatively take excitation and interaction in the solid into account.

In the last subsections the Kramers-Kronig relations and the f-sum rule are reviewed. These relations follow from the analytic properties of the linear response functions. The Kramers-Kronig relations connect the real and imaginary parts of the complex optical conductivity (or dielectric function).

2.2.1 Electromagnetic interaction with matter

The macroscopic Maxwell's equations relate the electric displacement field **D**, current J, and magnetic induction **B** to an external electromagnetic perturbation. The

Maxwell's equations are:

$$\nabla \cdot \mathbf{D} = \rho, \tag{2.1}$$
$$\nabla \times \mathbf{E} = -\frac{\partial \mathbf{B}}{\partial t}, \tag{2.2}$$
$$\nabla \cdot \mathbf{B} = 0, \tag{2.3}$$
$$\nabla \times \mathbf{H} = \mathbf{J} + \frac{\partial \mathbf{D}}{\partial t}, \tag{2.4}$$

where ρ is the charge density. The electric displacement field $\mathbf{D}$ in the medium is related to the external electric field $\mathbf{E}$. The magnetic induction $\mathbf{B}$ is related to the external magnetic field $\mathbf{H}$. The relations defining $\mathbf{D}$ and $\mathbf{B}$ are:

$$\mathbf{D} = \boldsymbol{\epsilon} \cdot \mathbf{E} = \epsilon_0 \mathbf{E} + \mathbf{P}, \tag{2.5}$$
$$\mathbf{B} = \boldsymbol{\mu} \cdot \mathbf{H} = \mu_0 \mathbf{H} + \mathbf{M}. \tag{2.6}$$

Here $\mathbf{P}$ is the electric polarization of the material, caused by the microscopic electric dipoles formed by bound charges. The magnetization density $\mathbf{M}$ is, in analogue to $\mathbf{P}$, caused by bound currents. The right hand side of eqn. (2.5) follows from the linear relation $\mathbf{P} = \epsilon_0 \boldsymbol{\chi}_e \mathbf{E}$, where $\boldsymbol{\chi}_e$ is the electric susceptibility and $\boldsymbol{\epsilon} = \epsilon_0(1 + \boldsymbol{\chi}_e)$, where $\boldsymbol{\epsilon}$ is the complex dielectric function. For eqn. (2.6) the linear relation $\mathbf{M} = \mu_0 \boldsymbol{\chi}_m \mathbf{H}$ was used, where $\boldsymbol{\chi}_m$ is the magnetic susceptibility and $\boldsymbol{\mu} = \mu_0(1 + \boldsymbol{\chi}_m)$.

The optical conductivity, σ, directly related to the dielectric function, ϵ, describes the linear response of the charge carriers in a material to the externally applied electromagnetic (EM) field. Note that both σ and ϵ are frequency dependent. The relationship between the electric field $\mathbf{E}$, the conductivity and the current, $\mathbf{J}_{cond}$, are expressed by Ohm's law:

$$\mathbf{J}_{cond} = \boldsymbol{\sigma} \cdot \mathbf{E}, \tag{2.7}$$

where $\boldsymbol{\sigma}$ is the complex optical conductivity tensor, which we will discuss later in this section.

The Maxwell's equations together with eqns. (2.7), (2.5) and (2.6) fully describe the propagation of the electromagnetic wave in the medium. The wave equation for the transverse electric field propagating in a medium is [101]:

$$\nabla^2 \mathbf{E} - \epsilon_1 \mu_1 \frac{\partial^2 \mathbf{E}}{\partial t^2} - \sigma_1 \mu_1 \frac{\partial \mathbf{E}}{\partial t} = 0. \tag{2.8}$$

Here the subscript 1 denotes the real part of the complex quantity, the subscript 2 indicates the imaginary part.

The wave propagating in the medium is of the form $\mathbf{E}(\mathbf{r}, t) = \mathbf{E_0} e^{i(\mathbf{q}\cdot\mathbf{r} - \omega t)}$, by substituting this into eqn. (2.8), the dispersion relation is obtained:

$$\mathbf{q}^2 = \boldsymbol{\mu}_1(\mathbf{q}, \omega) \left(\boldsymbol{\epsilon}_1(\mathbf{q}, \omega) + i \frac{\boldsymbol{\sigma}_1(\mathbf{q}, \omega)}{\omega} \right) \frac{\omega^2}{c^2}, \tag{2.9}$$

The wave vector $\mathbf{q}$ can also be expressed as:

$$\mathbf{q} \equiv \frac{\omega}{c}\sqrt{\boldsymbol{\mu}\boldsymbol{\epsilon}}, \tag{2.10}$$

where $\boldsymbol{\mu}$ and $\boldsymbol{\epsilon}$ are the complex magnetic and dielectric functions.

Comparing eqn. (2.10) with the dispersion relation, eqn. (2.9), the relationship between the complex dielectric function and the conductivity can be deduced:

$$\boldsymbol{\epsilon}(\omega) = \epsilon_1 + i\epsilon_2 = \epsilon_1 + i\frac{\sigma_1}{\omega}. \tag{2.11}$$

The optical conductivity itself must also be complex ($\boldsymbol{\sigma} \equiv \sigma_1 + i\sigma_2$) and is related to the dielectric function like:

$$\boldsymbol{\sigma}(\omega) = i\omega(1 - \boldsymbol{\epsilon}(\omega)). \tag{2.12}$$

The refractive index $\mathbf{n}$ follows from eqn. (2.10):

$$\mathbf{n}(\mathbf{q}, \omega) = n + ik \equiv \sqrt{\boldsymbol{\mu}\boldsymbol{\epsilon}}. \tag{2.13}$$

Everywhere in this work we assume that $\boldsymbol{\mu} = 1$, and thus $\mathbf{n} = \sqrt{\boldsymbol{\epsilon}}$.

As was already mentioned, the conductivity of an isotropic medium is a tensor. In particular, when an external magnetic field is applied the components of the tensor become magnetic field dependent. In Cartesian coordinates the conductivity tensor is given by:

$$\boldsymbol{\sigma}(\omega, \mathbf{B}) = \begin{pmatrix} \sigma_{xx}(\omega, \mathbf{B}) & \sigma_{xy}(\omega, \mathbf{B}) \\ -\sigma_{xy}(\omega, \mathbf{B}) & \sigma_{xx}(\omega, \mathbf{B}) \end{pmatrix}. \tag{2.14}$$

Where on the diagonal of the tensor, $\sigma_{xx}(\omega, \mathbf{B})$, is the 'optical conductivity' or 'diagonal conductivity'. The off-diagonal elements, $\sigma_{xy}(\omega, \mathbf{B})$, are only non-zero in the case that the time-reversal symmetry is broken, by e.g. an externally applied magnetic field $\mathbf{B}$. σ_{xy} is referred to as the 'off-diagonal' or 'optical Hall conductivity'.

The optical conductivity tensor has general symmetry properties. For the complex diagonal and off-diagonal conductivity [105]:

$$\begin{aligned} \sigma^*_{xx}(\omega, \mathbf{B}) &= \sigma_{xx}(\omega, \mathbf{B}), \\ \sigma^*_{xy}(\omega, \mathbf{B}) &= \sigma_{xy}(-\omega, \mathbf{B}), \end{aligned} \tag{2.15}$$

For the real and imaginary parts, separately, is found that:

$$\begin{aligned} \mathrm{Re}\,\sigma_{xx}(\omega, B) &= \mathrm{Re}\,\sigma_{xx}(-\omega, B), \quad \mathrm{Im}\,\sigma_{xx}(\omega, B) = -\mathrm{Im}\,\sigma_{xx}(-\omega, B), \\ \mathrm{Re}\,\sigma_{xy}(\omega, B) &= \mathrm{Re}\,\sigma_{xy}(-\omega, B), \quad \mathrm{Im}\,\sigma_{xy}(\omega, B) = -\mathrm{Im}\,\sigma_{xy}(-\omega, B). \end{aligned} \tag{2.16}$$

The Onsager relations tell that the complex diagonal elements are symmetric in magnetic field:

$$\sigma_{xx}(\omega, \mathbf{B}) = \sigma_{xx}(\omega, -\mathbf{B}), \tag{2.17}$$

While the complex off-diagonal elements are antisymmetric in field:

$$\begin{aligned} \sigma_{xy}(\omega, \mathbf{B}) &= \sigma_{yx}(\omega, -\mathbf{B}), \\ \sigma_{xy}(\omega, \mathbf{B}) &= -\sigma_{xy}(\omega, -\mathbf{B}). \end{aligned} \tag{2.18}$$

For an isotropic material the magneto-optical conductivity tensor is diagonal in the basis of circular coordinates, which is related to the Cartesian coordinates via the relation:

$$\sigma_{\pm} = \sigma_{xx} \pm i\sigma_{xy}. \tag{2.19}$$

The eigen modes of the electric field in the circular polarization are given by:

$$E_{\pm}(r,t) = \frac{1}{\sqrt{2}} \begin{bmatrix} 1 \\ \pm i \end{bmatrix} E_0 e^{i(\mathbf{q}\cdot\mathbf{r}-\omega t)}. \tag{2.20}$$

Importantly, in this thesis we most often consider the conductivity of ultra thin carbon layers. Therefore we need to distinguish the optical conductivity of bulk materials, the 3-dimensional conductivity, and the optical conductivity of thin films, the 2-dimensional conductivity. In the case of 3D conductivity the current J is a current density per volume, while in the 2D case J is the current density per area. Similarly, in the 3D case the carrier density n is per volume, while in the 2D case the carrier density n is counted per area.

For a more thorough discussion of the Maxwell's equations and the propagation of waves in a medium see for example Refs. [101–104].

2.2.2 Drude-Lorentz model in a magnetic field

The classical Drude-Lorentz model for (optical) conductivity describes the excitations in solids by considering the forces exerted on the charged particles in the solid. An electro-magnetic wave consist of time-varying electric and magnetic fields, giving the charged particles an oscillating motion. The force of the magnetic field is much smaller than the electric force, therefore, we can neglect the Lorentz force in the case that only the forces of the an electro-magnetic wave are considered.

However, when a static magnetic field (**B** field) is applied, the Lorentz force can no longer be neglected. The charged particles rapidly oscillate due to the time-varying electric field, while the static **B** field gives rise to a Lorentz force directed perpendicular to the motion of the particle and direction of the field. The resulting equation of motion for an electron with mass m is:

$$\frac{\mathrm{d}^2\mathbf{r}}{\mathrm{d}t^2} + \gamma\frac{\mathrm{d}\mathbf{r}}{\mathrm{d}t} + \omega_0^2\mathbf{r} = -\frac{e}{m}\mathbf{E}(t) + \frac{e}{m}\mathbf{v}\times\mathbf{B}, \tag{2.21}$$

where $\gamma = 1/\tau$, and τ is the average relaxation time and ω_0 is the eigenfrequency or resonance frequency of bound electrons. The displacement of the particles is considered to be harmonic: $\mathbf{x}(t) = \mathbf{x}e^{-i\omega t}$. Due to the presence of the magnetic field, the

motion of charge carriers in the x and y plane is coupled:

$$\begin{aligned} \ddot{X} + \gamma\dot{X} + \omega_0^2 X &= \frac{-eE_x}{m} + \omega_c\dot{Y}, \\ \ddot{Y} + \gamma\dot{Y} + \omega_0^2 Y &= \frac{-eE_y}{m} - \omega_c\dot{X}, \end{aligned} \tag{2.22}$$

where $\omega_c = eB/m$, is the cyclotron resonance frequency. By moving to frequency space, the time derivative becomes a simple multiplication, so that:

$$\begin{aligned} X(\omega + i\gamma - \frac{\omega_0^2}{\omega}) &= \frac{eE_x}{m\omega} + i\omega_c Y, \\ Y(\omega + i\gamma - \frac{\omega_0^2}{\omega}) &= \frac{eE_y}{m\omega} - i\omega_c X. \end{aligned} \tag{2.23}$$

Equation (2.23) is solved for the displacement in X and Y, from which then the current is found: $j_x = ne\dot{x} = \sigma_{xx}E_x + \sigma_{xy}E_y$, where in the 3-dimensional case n is the density of charge carriers per volume, while in the 2-dimensional case (thin films) n is the density of carriers per unit area. The current, j_x, is found to be:

$$j_x = \frac{ne^2E_x}{m}\frac{\gamma - i\omega + \frac{\omega_0^2}{\omega}}{\omega_c^2 - (\omega + i\gamma + \frac{\omega_0^2}{\omega})^2} - \frac{ne^2E_y}{m}\frac{\omega_c}{\omega_c^2 - (\omega + i\gamma + \frac{\omega_0^2}{\omega})^2}. \tag{2.24}$$

The diagonal ($\sigma_{xx}(\omega)$) and off-diagonal ($\sigma_{xy}(\omega)$) optical conductivities are obtained by identification:

$$\sigma_{xx}(\omega) = \frac{ne^2}{m}\frac{\gamma - i\omega + \frac{\omega_0^2}{\omega}}{\omega_c^2 - (\omega + i\gamma + \frac{\omega_0^2}{\omega})^2}, \tag{2.25}$$

$$\sigma_{xy}(\omega) = \frac{ne^2}{m}\frac{-\omega_c}{\omega_c^2 - (\omega + i\gamma + \frac{\omega_0^2}{\omega})^2}. \tag{2.26}$$

Generally, many different excitations are present in the material, at distinctive energies ω_0, with unique broadenings γ, cyclotron resonance energies ω_c and spectral weights D. In this case, eqns. (2.25) and (2.25), containing one single oscillator, can not provide an accurate description of the optical conductivity. To take into account all excitations a sum off all those contributions should be taken:

$$\sigma_{xx}(\omega) = \sum_{i=1}^{n}\frac{2D_i}{\pi}\frac{\gamma_i - i\omega + \frac{\omega_{0,i}^2}{\omega}}{\omega_{c,i}^2 - (\omega + i\gamma_i + \frac{\omega_{0,i}^2}{\omega})^2}, \tag{2.27}$$

$$\sigma_{xy}(\omega) = \sum_{i=1}^{n}\frac{2D_i}{\pi}\frac{-\omega_{c,i}}{\omega_{c,i}^2 - (\omega + i\gamma_i + \frac{\omega_{0,i}^2}{\omega})^2}. \tag{2.28}$$

Where we replaced $\frac{ne^2}{m}$ with $\frac{2D}{\pi}$.

Using relation (2.19), in the circular coordinates a simpler expression for the magneto-optical conductivity can be found:

$$\sigma_{\pm}(\omega) = \sum_{i=1}^{n} \frac{2D_i}{\pi} \frac{i}{\omega \mp \omega_{c,i} + i\gamma_i - \omega_{0,i}^2/\omega}. \tag{2.29}$$

Equations (2.27), (2.28) and (2.29) are used for the phenomenological data analysis in the analysis of the experimental results in this work.

In the absence of magnetic field, eqn. (2.28) reduces to zero and from eqns. (2.29) and (2.19) can be seen that $\sigma_+(\omega) = \sigma_-(\omega) = \sigma_{xx}(\omega)$, so that the Lorentz model for optical conductivity is reduced to:

$$\sigma(\omega) = \sum_{i=1}^{n} \frac{2D_i}{\pi} \frac{\omega}{i(\omega_{0,i}^2 - \omega^2) + \omega\gamma_i}, \tag{2.30}$$

In the case of metals, an additional important modification can be made; the charge carriers at the Fermi level move freely, such that the restoring force $\omega_0 = 0$. Consequently, in an optical spectrum, the response of free carriers, the so-called Drude peak, or Drude response, can be observed as a peak centered around zero energy. The famous Drude model for free carriers can be found from eqn. (2.30) when putting ω_0 to zero and taking only one term in the sum. Similarly, the complete Drude-Lorentz model directly follows from eqn. (2.30), where one of the terms in the summation has $\omega_0 = 0$, and the remaining terms account for the finite frequency contributions:

$$\sigma(\omega) = \frac{2D_D}{\pi} \frac{1}{\gamma_D - i\omega} + \sum_{i=1}^{n} \frac{2D_i}{\pi} \frac{\omega}{i(\omega_{0,i}^2 - \omega^2) + \omega\gamma_i}, \tag{2.31}$$

where D_D and γ_D are the Drude weight and the broadening of the Drude peak, respectively.

2.2.3 Kubo-Greenwood formula

A microscopic model for the optical conductivity can be derived from the point of view of quantum mechanics, using the linear response formalism to arrive at the Kubo-Greenwood formula. Here we will discuss the Kubo-Greenwood formula, which we will later encounter again when we specifically discuss the optical conductivity of graphene [106].

The conductivity is the linear response to a time-dependent perturbation:

$$H = H_0 + H_1(t), \tag{2.32}$$

where H_0 is the unperturbed, time-independent part of the Hamiltonian and $H_1(t)$ is the perturbation of the system due to the time-dependent electric field. The electric field induces a current density $j(,t)$, dependent on the conductivity of the material.

Ohm's law gives the relationship between electric field, conductivity and current density:

$$j_\alpha(t) = \int_{-\infty}^{t} \mathrm{d}t' \sigma_{\alpha\beta}(t-t') E_\beta(t'), \tag{2.33}$$

Using linear response theory the total current can be obtained, then by identification the Kubo's formula for the conductivity is found, which is in frequency space [106]:

$$\sigma_{\alpha\beta}(\omega) = \frac{ie^2 N \delta_{\alpha\beta}}{Vm\omega^+} + \frac{1}{V\hbar\omega^+} \int_{-\infty}^{\infty} \mathrm{d}\tau \theta(\tau) \langle [J_\alpha(\tau), J_\beta(0)] \rangle e^{i\omega^+\tau}, \tag{2.34}$$

where V is the volume, N is the total particle density, $\tau = t - t'$, $\theta(\tau)$ is the Heaviside function, $J = -e\sum_i v_i$ is the total current and v_i is the particle velocity. $\omega^+ \equiv \omega + i\delta$, where δ is a infinitely small term added to assure convergence. $-\theta(\tau)\langle [J_\alpha(\tau), J_\beta(0)] \rangle$ is the many-body current-current correlation function.

Equation (2.34) can be simplified significantly by using single-particle states instead of the many-body current-current correlation function:

$$\sigma_{\alpha\beta}(\omega) = \frac{e^2}{V} \sum_{nn'} \frac{f(E_n) - f(E_{n'})}{E_n - E_{n'}} V^\alpha_{n'n} V^\beta_{nn'} \frac{i}{\omega - \omega_{nn'} + i/\tau}, \tag{2.35}$$

where $f(E_n)$ is the fermi distribution, E_n is the energy of the single particle state. We introduced the velocity operator $v = p/m$, where p is momentum and m is the particle mass and used $V^\alpha_{n'n} = \langle n|v_\alpha|n'\rangle$ and $\omega_{nn'} = \omega_n - \omega_{n'}$. Finally, $i\delta$ was replaced by i/τ, which is the finite lifetime interpretation.

In the case that we consider the conductivity of a thin film, $\sigma_{\alpha\beta,2D}(\omega)$, we have to replace the volume V in eqn. (2.35) by the 2 dimensional volume V_{2D} (area). We also introduce the dimensionless universal optical conductivity: $\sigma_0 = e^2/4\hbar$, and rewrite the velocity operator as $v_\alpha = \frac{1}{\hbar}\frac{\partial H_0}{\partial q_\alpha}$ to arrive at a simple version of the Kubo-Greenwood formula for the 2-dimensional conductivity:

$$\sigma_{\alpha\beta,2D}(\omega) = \frac{8\sigma_0}{V_{2D}} \sum_{nn'} \frac{f(E_n) - f(E_{n'})}{E_n - E_{n'}} \langle n|\frac{\partial H_0}{\partial q_\alpha}|n'\rangle\langle n'|\frac{\partial H_0}{\partial q_\beta}|n\rangle \frac{i}{\hbar\omega - \hbar\omega_{nn'} + i\gamma}. \tag{2.36}$$

Where we also introduced an additional factor of two to take into account the spin degeneracy, $\gamma = \hbar/\tau$ is a phenomenological broadening and H_0 is the single-particle Hamiltonian which describes the energy levels of the system. Equation (2.36) forms the starting point for deriving the magneto-optical properties of thin films, discussed in section 3.3.3.

2.2.4 Kramers-Kronig relations

We have seen that the functions describing the response of a material to an external field, the optical conductivity and the dielectric function, are complex tensors. In order to obtain a full picture of the magneto-optical response of a material, one needs

to determine every component of that tensor. However, as we will see later, optical experiments often only provide the real part of one or more of those components of the tensor, such as $\mathrm{Re}\,\sigma_{xx}(\omega)$ and $\mathrm{Re}\,\sigma_{xy}(\omega)$. Fortunately, the real and imaginary parts of the linear response function turn out to be related by the Kramers-Kronig relations.

Although they are general relations revealing the direct relationship between the real and imaginary parts of any causal response function, here we give the Kramers-Kronig relations for the optical conductivity [101, 102]:

$$\sigma^{(1)}_{\alpha\beta}(\omega) = \frac{1}{\pi}\mathcal{P}\int_{-\infty}^{+\infty}\frac{\sigma^{(2)}_{\alpha\beta}(\omega')}{\omega'-\omega}\mathrm{d}\omega', \tag{2.37}$$

$$\sigma^{(2)}_{\alpha\beta}(\omega) = -\frac{1}{\pi}\mathcal{P}\int_{-\infty}^{+\infty}\frac{\sigma^{(1)}_{\alpha\beta}(\omega')}{\omega'-\omega}\mathrm{d}\omega'. \tag{2.38}$$

Here the superscript 1 (2) indicates the real (imaginary) part of the conductivity. The subscripts α and β denote the cartesian coordinates x and/or y: for example, the term $\sigma^{(1)}_{\alpha\beta}(\omega)$ can be $\sigma^{(1)}_{xx}(\omega)$ or $\sigma^{(1)}_{xy}(\omega)$. Thus, the Kramers-Kronig relations apply to the real and imaginary parts of both σ_{xx} and σ_{xy} separately.

2.2.5 f-sum rule for optical conductivity

The Thomas-Reiche-Kuhn sum rule, or f-sum rule, tells us that the sum of the strengths of all oscillators is proportional to the ratio of the electronic density to the mass of the carriers [101]:

$$W = \int_0^\infty \mathrm{Re}[\sigma(\omega)]\mathrm{d}\omega = \frac{\pi n e^2}{2m}, \tag{2.39}$$

where W is the total spectral weight, or the area under $\mathrm{Re}[\sigma(\omega)]$ up to infinite frequency. A consequence of the f sum rule is that the optical conductivity is conserved, even though spectral weight can be transferred between several oscillators at different energies. The principle of conservation of spectral weight can be used to, for example, analyze the strength of emerging optical transitions and the transfer of weight between them. However, in general the optical conductivity is not determined up to infinite frequency, therefore in practice, a frequency range must be chosen for the analysis of spectral weight.

The f-sum rule is derived from the Kubo-Greenwood relations, discussed in the previous section. However, in magnetic field, time-reversal symmetry is broken and the eigenstates of the system are the circular polarized states. The real and imaginary parts of the conductivity in the basis of left and right circular polarization do not satisfy the Kramers-Kronig relations individually [107, 108]. The reason for this violations is that the conductivities are not even in frequency and therefore causality does not hold. Still an f-sum rule in the circular basis can be formulated, strictly valid for non-magnetic materials: the average strength of the left and right circular polarizations is

conserved and yields the total number of charge carries [109]:

$$D = \int_0^\infty \frac{(\mathrm{Re}[\sigma(\omega)_+] + \mathrm{Re}[\sigma(\omega)_-])}{2} \mathrm{d}\omega = \int_0^\infty \mathrm{Re}[\sigma_{xx}(\omega)] \mathrm{d}\omega = \frac{\pi n e^2}{2m}. \quad (2.40)$$

2.3 Experimental quantities

In the previous section we have introduced models for the (magneto-) optical conductivity. These models can be employed to analyze the conductivity of solids, so that we can distinguish the different contributions of distinct excitations and learn about their energy, broadening and weight. However, to be able to do this analysis, we first need to experimentally determine the optical properties of a solid. In this section we will discuss the experimental quantities – transmission, Fabry-Perot interference and Faraday rotation – and how to obtain from them the optical conductivity. In the second part of each section we will describe the experimental techniques and set-ups used to measure the infrared transmission and Faraday rotation spectra in magnetic field.

The experimental work presented in this thesis is almost exclusively performed on samples of thin graphene films grown on a thick SiC substrate. Both graphene and the SiC substrate are transparent in the far infrared region; our region of interest. Therefore, the experimental quantity most reliably obtained experimentally is the transmission of the film on the substrate and the bare transmission of the substrate. In an externally applied magnetic field, the transmission spectra are obtained as a function of field. Apart from transmission, an additional experimental parameter, only finite at non-zero magnetic field, is the Faraday rotation, which proves to be an important optical quantity, not only for technical applications, but because it provides access to the AC Hall conductivity.

In section 2.3.1 we first discuss the thin film approximation with which the real part of the diagonal optical conductivity can be extracted from the experimental transmission spectra. The second part of the section is dedicated to a description of the experimental technique used to obtain the transmission as a function of magnetic field. Section 2.3.2 demonstrates the extraction of the change in the imaginary part of the diagonal conductivity relative to the magnetic field. The change in conductivity can be found from Fabry-Perot oscillations in the high resolution transmission spectra of the thin film on the substrate. Again, the second part of the section is dedicated to a description of the experimental technique used to study the field dependence of the Fabry-Perot interference. In the last section the principle of Faraday rotation in a solid is introduced. Subsequently, we discuss the use of experimental Faraday rotation spectra for extracting the real part of the AC Hall conductivity. The experimental method is detailed in the end of section 2.3.3.

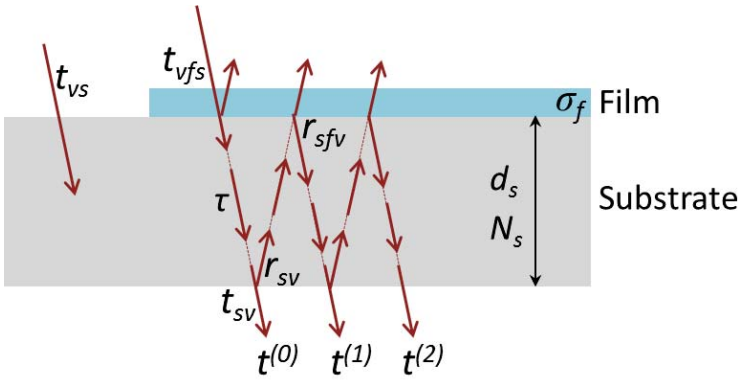

Figure 2.1: Schematic representation of the path of light transmitted through a thin film on a substrate. The complex transmission and reflection coefficients are indicated. The path of the first two internally reflected rays are also shown. For clarity the rays are tilted, in the experiments however, near normal incidence was used.

2.3.1 Transmission of a thin film on a substrate

Theoretical background

The type of sample used in the experimental part of this work consists of a thin conducting film on a thick insulating substrate, schematically shown in Fig. 2.1. The substrate is characterized by its complex refractive index, $N_s = n_s + ik_s$, where n_s is the real part of the refractive index and k_s is the extinction coefficient, and its thickness d_s. N_s can be obtained from an optical experiment, while d_s is measured with a micrometer. The film has a two dimensional optical conductivity σ_f, which is the optical property of interest and thus the subject of our study. The experimental quantities we access are the transmission of the substrate, T_s, and the transmission of the film on the substrate, T_f. The transmission ratio between sample and substrate,$T = T_f/T_s$, will prove to be the key experimental quantity from which the conductivity of the film, σ_f, can be extracted. In this section we will derive expressions for T in terms of N_s, d_s and σ_f with the use of complex transmission and reflection coefficients.

Figure 2.1 shows the optical path of light impinging on the thin film + substrate and shows the complex transmission and reflection coefficients, which are:

$$t_{vs} = \frac{2}{N_s + 1},\ t_{sv} = \frac{2N_s}{N_s + 1},\ t_{vfs} = \frac{2}{N_s + 1 + Z_0\sigma_f}, \tag{2.41}$$

$$r_{sv} = \frac{N_s - 1}{N_s + 1},\ r_{sfv} = \frac{N_s - 1 - Z_0\sigma_f}{N_s + 1 + Z_0\sigma_f},\ \tau_s = \exp\left(\frac{i\omega}{c}N_s d_s\right), \tag{2.42}$$

where $Z_0 = 4\pi/c \approx 377\ \Omega$ is the impedance of vacuum.

The light transmitted by the film is partially reflected internally at the substrate-vacuum (v) interface and at the substrate-film interface. Several of these internal reflections in the substrate are shown in Fig. 2.1, their transmission is indicated as $t^{(j)}$,

where j is the ray number. The complex transmission of the first ray ($j = 0$) is $t_f^{(0)} = \tau_s t_{vfs} t_{sv}$. The general expression of the complex transmission of every j^{th} ray has the form:

$$t_f^{(j)} = \tau_s t_{vfs} t_{sv} (r_{sv}\, r_{sfv}\, \tau_s^2)^j. \tag{2.43}$$

The complex transmission of the substrate, $t_s^{(j)}$, can be found by replacing $t_{vfs} \to t_{vs}$ and $r_{sfv} \to r_{sv}$ in eqn. (2.43).

If the substrate is flat-parallel and homogeneous, the internally reflected rays are fully phase coherent, resulting in Fabry-Perot oscillations in the spectrum. In order to compute the total transmission we simply add the transmission of every ray: $t_f = \sum_j t_f^{(j)}$. On the contrary, when phase coherence is destroyed by a wedged substrate or a rough sample surface, the total transmission should be obtained by adding intensities. In most of the experiments discussed in this work the spectral resolution was reduced either at the time of the data acquisition, or by locally fitting the Fabry-Perot fringes when analyzing the spectra, so that the internally reflected rays add up incoherently. In the incoherent case the multiple rays add by power and not by electric field. The total transmission coefficients of the sample, T_f, and the substrate, T_s, are given by:

$$T_f = \frac{|\tau_s t_{vfs} t_{sv}|^2}{1 - |r_{sv}\, r_{sfv}\, \tau_s^2|^2}, \qquad T_s = \frac{|\tau_s t_{vs} t_{sv}|^2}{1 - |r_{sv}^2\, \tau_s^2|^2}, \tag{2.44}$$

from which the substrate normalized transmission can be found, using eqns. (2.41) and (2.42):

$$\begin{aligned} T = \frac{T_f}{T_s} &= \left|\frac{t_{vfs}}{t_{vs}}\right|^2 \frac{1 - |r_{sv}^2 \tau_s^2|^2}{1 - |r_{sfv} r_{sv} \tau_s^2|^2} \\ &= \frac{|N_s + 1|^4 - |N_s - 1|^4 |\tau_s|^4}{|(N_s + 1)(N_s + 1 + Z_0\sigma_f)|^2 - |(N_s - 1)(N_s - 1 - Z_0\sigma_f)|^2 |\tau_s|^4}. \end{aligned} \tag{2.45}$$

For a transmission experiment, the substrate must be at least partially transparent, therefore the penetration depth ($\sim 1/k_s$) must be large compared to the thickness of the substrate and $k_s \ll n_s$ in this case. With this in mind we neglect the imaginary part of the refractive index, k_s; N_s is substituted with n_s, except in τ_s, which is used to we define $\alpha = |\tau_s|^2 = exp(-2\omega k_s d_s/c)$, note that here α is not to be confused with the fine structure constant. Now, by decomposing the last relation in terms of the conductivity, eqn. (2.45) can be written as:

$$T = \left[1 + \frac{2}{n_s + 1} \frac{1 + \alpha^2 r^3}{1 - \alpha^2 r^4} \,\mathrm{Re}\,(Z_0\sigma_f) + \frac{1}{(n_s + 1)^2} \frac{1 - \alpha^2 r^2}{1 - \alpha^2 r^4} \,|Z_0\sigma_f|^2\right]^{-1}, \tag{2.46}$$

where the substrate-vacuum reflectivity coefficient is re-entered, using the short notation $r_{sv} = r = (n_s - 1)\,/\,(n_s + 1)$. The resulting relation is a function of both the real and imaginary part of σ_f. However, from the experimentally obtained substrate normalized transmission, only, the complex conductivity cannot be determined. The

imaginary part of σ_f appears in the third term of eqn. (2.46), which has a significantly smaller prefactor than the second term, in which only the real part of σ enters. Therefore, we make an approximation and neglect the influence of $\mathrm{Im}[\sigma_f]$.

As already mentioned in section (2.2.2), in a perpendicular magnetic field, the conductivity and the transmission both become a tensor. In the basis of circularly polarized light, these tensors are diagonal and eqn. (2.46) thus describes the transmission of left- and right handed circularly polarized light separately, if σ_f is substituted with $\sigma_\pm^f$ and T with $T_\pm$. For unpolarized light $T = 1/2(T_+ + T_-)$. However, without experimental scheme to obtain $T_\pm$, at finite magnetic fields, we make an additional approximation by neglecting the small influence of $\mathrm{Re}[\sigma_{xy}^f]$ on the transmission. Thus we obtain the expression:

$$T \cong \left[1 + \frac{2}{n_s+1}\frac{1+\alpha^2 r^3}{1-\alpha^2 r^4}\,\mathrm{Re}\left(Z_0\sigma_{xx}\right) + \frac{1}{(n_s+1)^2}\frac{1-\alpha^2 r^2}{1-\alpha^2 r^4}\mathrm{Re}\left(Z_0\sigma_{xx}\right)^2\right]^{-1}. \tag{2.47}$$

With this relation, the optical conductivity of the thin film can be extracted by entering the experimental substrate normalized transmission, the refractive index and the extinction coefficient of the substrate. When neglecting the quadratic part of eqn. (2.47) the linear expression is found:

$$T \cong \left[1 + 2Z_0\mathrm{Re}\left(\sigma_{xx}\right)\left(\frac{1}{n_s+1} + \frac{2n_s}{(n_s-1)^2}\frac{|q|^2}{1-|q|^2}\right)\right]^{-1}. \tag{2.48}$$

where $|q| \equiv (n_s-1)/(n_s+1)^2\,\tau_s^2$. The last equation can be even more simplified using the linear approximation $(1-x)^{-1} \approx 1+x$, we arrive at the simple relation (provided that $Z_0\mathrm{Re}[\sigma_{xx}^f] \ll 1$):

$$1 - T \cong 2Z_0\mathrm{Re}(\sigma_{xx})\left(\frac{1}{n_s+1} + \frac{2n_s}{(n_s-1)^2}\frac{|q|^2}{1-|q|^2}\right). \tag{2.49}$$

In the derivation of eqn. (2.47) we rely on the thin film approximation and, at zero magnetic field, neglect the imaginary part of σ_{xx}. At finite magnetic fields, the approximation becomes more severe by ignoring the influence of σ_{xy} on the transmission ratio. In order to estimate the difference between the exact optical conductivity and the one obtained from eqn. (2.47), we performed a numerical check. The details of the procedure and the results are discussed in appendix B.1. The results of the numerical check show that eqn. (2.47) proves reasonably accurate, especially in reproducing the peak positions in the optical spectra. At zero or low magnetic fields the spectral weight is slightly overestimated depending on the amount of absorption in the film. On the contrary, at higher magnetic fields, neglecting σ_{xy} result in an underestimation of the spectral weight, where the level of deviation strongly depends on the amount of absorption in the film and the cyclotron resonance energy.

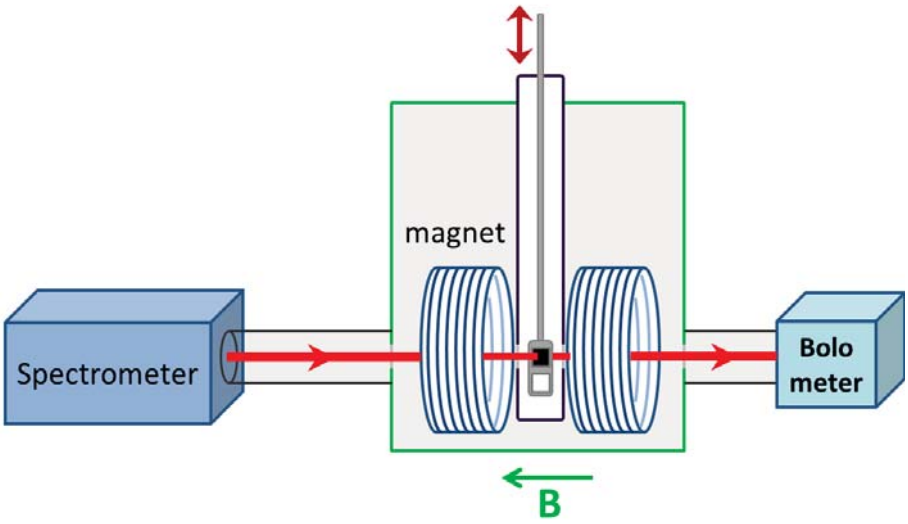

Figure 2.2: Experimental setup: a spectrometer is attached to a split coil superconducting magnet and bolometer. A polarizer can be placed between spectrometer and magnet so that the light of the spectrometer is linearly polarized before impinging on the sample. With the use of a sliding cold finger the sample position can be changed.

Experimental method

All transmission spectra were measured using a commercial infrared Fourier transform spectrometer from Bruker [110] equipped with a Hg-source for the terahertz regime and a SiC Globar source for the infrared regime. Inside the spectrometer the light from the source is directed to an interferometer. Firstly, the light is impinging on a beamsplitter, which reflects a part of the light to a fixed mirror and the other part of the light is transmitted and falls on a scanning mirror. When scanning the mirror, the optical path of that light ray is varied, so that upon recombination of the two beams, the one from the fixed mirror and the one of the scanning mirror, the beams interfere, creating a time-dependent pulse. The resulting time-dependent signal is called the interferogram. Below 12 meV (100 cm^{-1}), a silicon beamsplitter was used, while for higher frequencies a germanium coated 6 μm mylar beamsplitter is more suited. The light beam leaving the interferometer is guided to a superconducting magnet with the use of several mirrors, where it is focussed on the sample. The transmitted beam is then focussed on a helium cooled silicon bolometer. The impinging light raises the temperature of the silicon detector. The temperature change induces a change in the resistance, which is registered as a function of time. The higher the intensity of the light which hits the detector, the larger the change in resistance. The registered time dependent amplitude is Fourier transformed to obtain the amplitude of the transmitted light as a function of frequency. With the above mentioned sources (Globar and Hg-source) and beamsplitters (silicon and Ge coated 6 μm mylar), used in combination

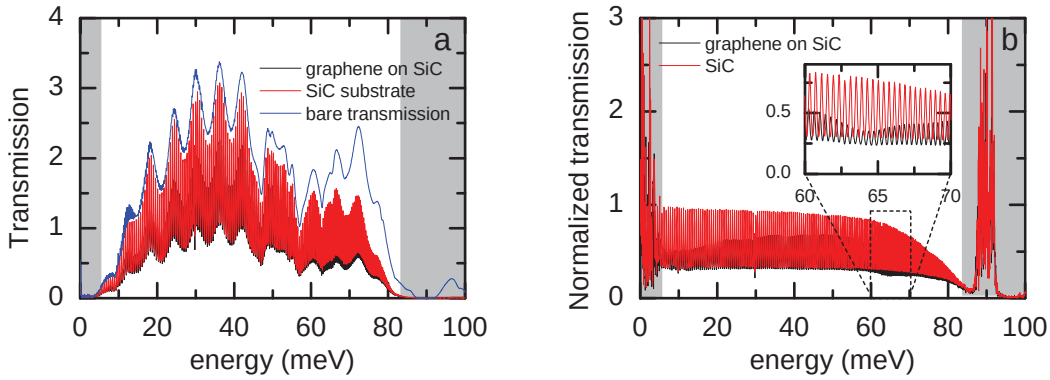

Figure 2.3: Typical transmission spectra of graphene on SiC and a bare SiC substrate measured with a resolution of 0.05 meV, T = 5 K and B = 3 T. a) Raw transmission spectra of graphene on SiC (black line), the bare SiC substrate (red line) and transmission without sample (blue line). b) Absolute transmission spectra of graphene on SiC and of the bare SiC substrate. The inset in panel b shows a close-up of an absorption dip in the graphene spectrum. The grey shaded areas at low and high energies in panels a and b indicate the energy ranges where the combination of source, beamsplitter and bolometer, does not supply enough intensity to provide useful optical spectra.

with the bolometer, the accessible range of optical energies ranges from about 1.0 meV to about 85 meV, where the upper limit of 85 meV is, on one hand, determined by the filter in the bolometer and on the other hand by the phonons in the substrate used in our experiments.

The superconducting magnet is a commercial split-coil magnet from Cryogenic Limited [111]. The magnet can deliver fields up to ± 7 T. A sample and reference substrate can be mounted simultaneously on a sliding cold finger and are inserted at the top of the magnet into the sample chamber. The sample chamber can be filled with helium gas of liquid providing a variable temperature between 2.2 and 300 K. This type of sample insert is referred to as a 'VTI'; Variable Temperature Insert. By sliding the cold finger in the vertical direction, either the sample or the reference can be placed in the path of the beam or both can be moved out of the optical path, while the temperature inside the magnet stays unchanged. This system allows us to normalize the transmission spectra of the sample to the bare transmission of the substrate or transmission without reference and to avoid drift or other variations in the experimental set-up as much as possible. Figure 2.2 gives a schematic impression of the ensemble of the spectrometer, magnet, sliding cold finger and bolometer.

Typically we determine the transmission ratio T between sample and reference at a fixed temperature and magnetic field. The absolute transmission of sample or reference is obtained by normalizing their spectra to the spectrum of the light that passes the magnet when no sample or reference is placed in the optical path. The best energy resolution with which the spectra can be obtained is about 0.05 meV. Figure 2.3a shows examples of transmission spectra taken with this high resolution on a (almost)

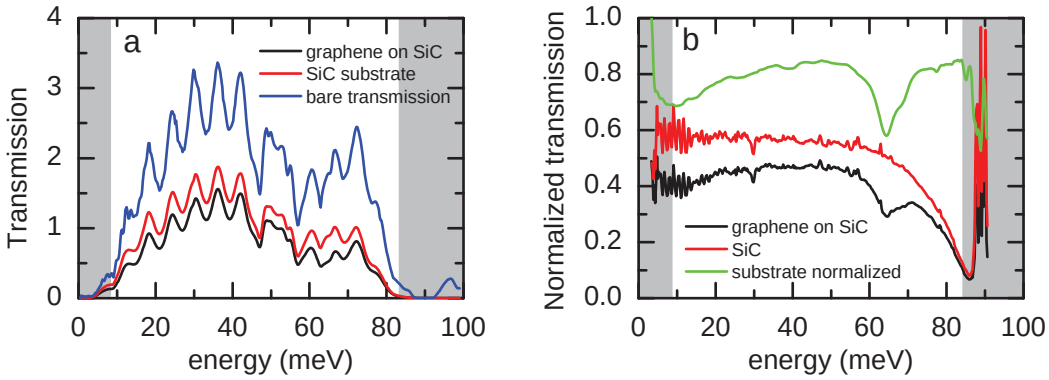

Figure 2.4: Typical transmission spectra of graphene on SiC and a bare SiC substrate measured with a resolution of 0.65 meV, at T = 5 K and B = 3 T. a) Raw transmission spectra of graphene on SiC, SiC and without sample. b) Absolute transmission spectra of graphene on SiC (black line), SiC (red line) and the transmission ration T between graphene on SiC and the SiC substrate (green line). The intensity of the transmission light in the grey areas is too low for a accurate extraction of the transmission spectra.

flat parallel sample, using a Hg-source and a 6 μm mylar beamsplitter. The grey shaded areas below 6 meV and above 85 meV indicate photon energies where the intensity of the signal is too low for an accurate extraction of the transmission. The amplitude of the transmission spectra of the sample and reference oscillate strongly, which is due to internal reflections (Fabry-Perot interference) in the SiC substrate. The origin of the internal reflections is illustrated in Fig. 2.1, in section (2.3.1), and more extensively discussed in section 2.3.2. Absolute spectra are obtained by normalizing the raw transmission to the raw transmission of the set-up, so that the absolute transmission reflects only the transmission of the sample or substrate, shown in Fig. 2.3b. Although the absolute transmission of graphene on SiC is clearly different from the one of the bare SiC reference, the analysis and interpretation of the spectra in Fig. 2.3b is complicated by the presence of the pronounced Fabry-Perot oscillations.

The Fabry-Perot oscillations (or fringes) form a nuisance for the extraction of $\mathrm{Re}[\sigma_{xx}]$ from the transmission spectra. Therefore, the oscillations must be removed from the spectra. The removal of the fringes can be done in different ways. Either every fringe in the high resolution spectra is locally fitted, which is the subject of the next subsection, alternatively the spectra are measured with a lower spectral resolution effectively canceling out the oscillations. Another way to get around the Fabry-Perot oscillations is to destroy the phase coherence between the internal reflections by using a wedged sample or a sample with large surface roughness.

Importantly, one can make use of the Fabry-Perot oscillations and extract relative changes in $\mathrm{Im}[\sigma_{xx}]$ by analyzing the shift in the fringes for different magnetic fields, as is discussed in sections (2.3.2).

Figure 2.4 shows the same transmission data as Fig. 2.3, measured with an approximately ten times lower resolution (the resolution is 0.65 meV). Crucially, the

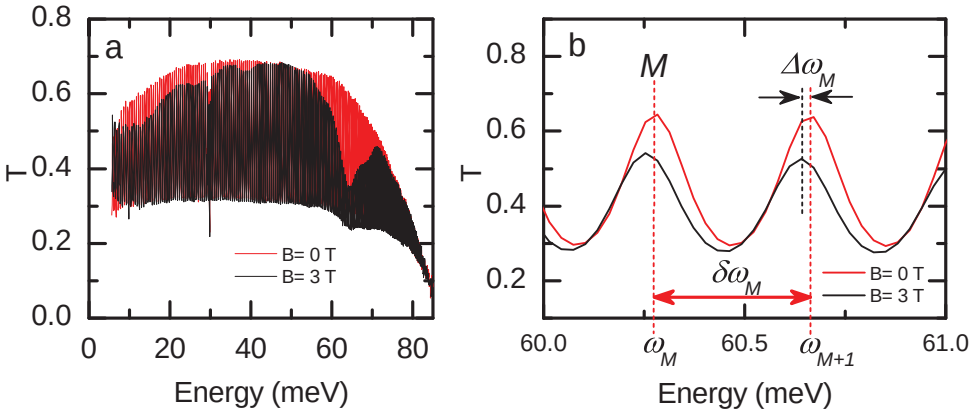

Figure 2.5: High resolution transmission spectra showing Fabry-Perot oscillations. (a) Transmission of graphene on SiC for zero field and 3 T. (b) Close up of the spectra in (a), the fringes at 3 T are shifted with respect to 0 T. The fringes number is indicated as M, the period of the fringes is $\delta\omega_M$, and the shift is $\Delta\omega_M$, the frequency at which constructive interference is maximum is indicated as ω_M.

Fabry-Perot oscillations in the substrate are averaged. The raw transmission spectra in Fig. 2.4a now only show broad oscillations which stem from, among other, the windows between source, the sample and the detector, but these are canceled when the ratio between sample and reference is taken. The absolute transmission spectra, Fig. 2.4b, reveal the effect of the graphene layer on the transmission, most clearly seen in the ratio between the transmission of graphene on SiC and the bare SiC substrate (green line in panel b). This sample-substrate ratio T, forms the input of eqn. (2.47), with which $\mathrm{Re}[\sigma_{xx}]$ is obtained.

2.3.2 Fabry-Perot oscillations in the substrate

Theoretical background

A significant advantage of the thick substrate + thin film system, is that from the Fabry-Perot oscillations in the substrate valuable information about the optical properties of the film can be extracted. In order to observe Fabry-Perot oscillations, the internal reflections of the light must be coherent; so that at selected frequencies constructive and destructive interference occurs. High resolution transmission spectra of graphene on SiC are shown in Fig. 2.5a for 0 and 3 T. The shape of the oscillations is described by an inverse sine function [112]. Internally reflected waves interfere constructively when their phase difference, φ, is equal to an integer times 2π. The phase difference between the waves follows from the Fresnel relations (eqns. (2.42)). The phase is given by the argument of the additionally obtained transmission coefficient:

$$\varphi = \frac{2\omega_M d_s N_s}{c} + \arg(r_{sfv}) = 2\pi M, \tag{2.50}$$

where ω_M is the frequency at which constructive interference occurs, M is the integer number of that maximum and r_{sfv} is defined in Fig. 2.1. An externally applied magnetic field changes the conductivity of the film, $\sigma^f(\omega)$, thus $\arg(r_{sfv})$. Consequently the phase of internally reflected light is shifted, which introduces a change in the Fabry-Perot interference. In Fig. 2.5b a close up of the transmission data from Fig. 2.5a is plotted, showing a few individual oscillations. The fringes at 3 T are clearly shifted in frequency with respect to the fringes at 0 T. Providing that the optical properties of the substrate stay unaltered by the field, the change φ with magnetic field is directly related to the field derivative of $\mathrm{Im}[\sigma^f_{xx}(\omega)]$. This relation can be shown by taking the field derivative of eqn. (2.50) and developing $\arg(r_{sfv})$, which is done in appendix B.2. More precise, from the shift in maximum frequency normalized to the oscillation period, $\frac{\Delta\omega_M}{\delta\omega_M} = \xi$, one can find $\Delta\mathrm{Im}[\sigma^f_{xx}(\omega)]$, according to:

$$\Delta\mathrm{Im}[\frac{\sigma_{xx}}{\sigma_0}] = \frac{\xi}{\alpha}\frac{n_s^2 - 1}{n_s}, \tag{2.51}$$

where α is the fine structure constant and n_s is the real part of the refractive index of the substrate.

In deriving eqn. (2.51) several approximations were used, the impact of these simplifications is determined by a numerical check, of which the details are discussed in appendix B.3. Exactly extracted $\Delta\mathrm{Im}[\sigma^f_{xx}(\omega)]$ are compared with $\Delta\mathrm{Im}[\sigma^f_{xx}(\omega)]$ obtained from eqn. (2.51) using the Fabry-perot oscillations from transmission spectra.

Experimental method

As mentioned above, the Fabry-Perot oscillations contain important information about the relative changes in $\mathrm{Im}[\sigma_{xx}]$ of the film on top of the substrate. To extract $\Delta\mathrm{Im}[\sigma_{xx}]$, the shift in the energy at which coherence occurs should be determined.

The Fabry-Perot fringes are best resolved when the spectra on the sample are normalized to spectra of the 'empty' set-up. The sample must be as flat parallel as possible, since a wedge can reduce or completely cancel out the oscillations. Naturally, the spectra must be obtained with a resolution several times higher than the period of the oscillations. Figure 2.5a shows an example transmission spectra taken on graphene on SiC which are normalized to the 'empty' set-up. The red curve corresponds to the normalized transmission at a magnetic field of 0 T, while the black curve corresponds to B = 3 T. In Fig. 2.5b a close-up of the absorption is shown. The Fabry-perot oscillations measured at 3 T are clearly shifted with respect to the fringes at 0 T.

To analyze the change in the period the inverse of the normalized transmission is fitted locally with a sine function. From these fits the period of the oscillation, the average transmission, and the position of the oscillation as a function of the energy is obtained. The average transmission is now free of fringes, and therefore can be used as an input for eqn. (2.47), with which $\mathrm{Re}[\sigma_{xx}]$ is obtained. The positions of the oscillations can be used to calculate the shift in the oscillations induced by an externally applied field, which is the input for eqn. (2.51), with which $\mathrm{Im}[\sigma_{xx}]$ is obtained.

A related analysis of the interference fringes was performed in the thesis work of J. Feenstra [112].

2.3.3 Faraday rotation of a thin film on a substrate

Theoretical background

Faraday rotation is the rotation of the polarization state of light by a medium placed in a perpendicular magnetic field. The magnetic field breaks the time reversal symmetry and the absorption and extinction coefficients for left and right handed circularly polarized light become different. Therefore, if linearly polarized light (which is a superposition of left and right handed polarized light) propagates through such an optically active material, the transmitted light gains an elliptical character with a rotated main axis with respect to the polarization of the incident light. The effect was discovered by Michael Faraday in 1846 and is known since as the Faraday effect [113]. Through the years many materials showing the Faraday effect have been identified, and several of them have found their way to applications in the fields like optical detectors, sensing (measuring magnetic fields) and optical communication.

The material properties responsible for the rotation of the polarization plane of the light is the difference in propagation speeds for left and right handed circularly polarized light, therefore, the thickness of the material plays a crucial role in the magnitude of the rotation. In many cases, the Faraday rotation is simply linearly proportional to the sample thickness. In magnetic materials, the Faraday effect is closely related to the Zeeman effect. When an external magnetic field is applied, the energy levels split due to a coupling between field and the total angular momentum. Light can excite charge carriers between the levels and interact with the spin of those carriers through the magnetic field component of the radiation. Whether photons are absorbed by the magnetically polarized material depends on their angular momentum, which can be parallel or antiparallel to the magnetic polarization. Therefore the selection rules for left and right handed circular polarized light are different and the Faraday effect is observed. This type of interaction lies at the origin of the Faraday rotation observed in for example $EuTiO_3$ [114].

In graphene however, the origin of the Faraday rotation lies in the interaction between the electric field component of the electromagnetic radiation and the orbital motion of the charge carriers. When an external magnetic field is applied, the electron and hole bands of graphene split up into Landau levels (see section 3.3.1). Due to strict selection rules for the dipole excitations between the Landau levels, the absorption of left and right handed circular polarized light is different as soon as the Fermi energy is shifted away from the Dirac point (see section 3.3.3), effectively causing Faraday rotation of the polarization state of the light transmitted through the graphene.

In thin films, the Faraday rotation spectra are directly related to the optical Hall conductivity, σ_{xy}, which is the 'off-diagonal' element of the magneto-optical conductivity tensor. The extraction of the optical Hall conductivity from the experimentally

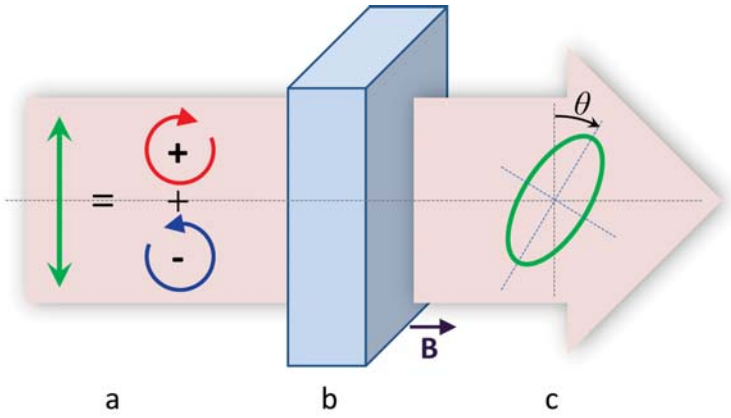

Figure 2.6: Scheme of light, indicated by the pink large arrow, transmitted by a sample in a perpendicular magnetic field. (a) The green arrow on the left shows the initial linear polarization, which in the circular basis, consists of left and right handed circularly polarized light, schematically represented by the red and blue circles. (b) In the sample the left and right handed polarized light experiences different propagation and absorption, which is shown by the unequal red and blue circles. (c) The net result after transmitting the sample is elliptically polarized light with the main axis rotated over an angle θ with respect to the original orientation of the linear light.

obtained Faraday rotation offers a route to study the magneto-optical properties of the charge carriers in the sample. When combined with transmission measurements from which the diagonal elements of the conductivity tensor can be extracted a full picture of the real part of the optical properties of a material can be obtained.

Importantly, in parallel to the DC Hall effect, the optical Hall effect is sensitive to the sign of the charge carriers, offering a valuable extra piece of information about the sample under study. Additionally, with both the real diagonal conductivity and the real Hall conductivity known, the magneto-optical conductivity in the basis of circular polarization can be obtained by using the Kramers-Kronig relations.

Figure 2.6 shows schematically the evolution of the polarization state of light impinging a material in a perpendicular magnetic field. Initially the light is linearly polarized (stage a), however, due to a different propagation velocity and difference in absorption of left and right handed circularly polarized light (stage b, inside the sample) the polarization becomes elliptical and the plane is rotated over an angle θ (stage c).

At zero magnetic field, when the time-reversal symmetry is not broken (t_{xy} of the sample 0), the Faraday effect in the sample is zero. Therefore, when a polarizer and an analyzer placed before and after the sample respectively, are crossed the intensity of the light reaching the detector will be at minimum. When the polarizer and the analyzer are parallel, the intensity detected will be maximum.

Figure 2.7 shows a model of the transmitted intensity for ϕ between 0 and π radian. Maximum intensities are observed at both 0 and π radian, when the angle of the

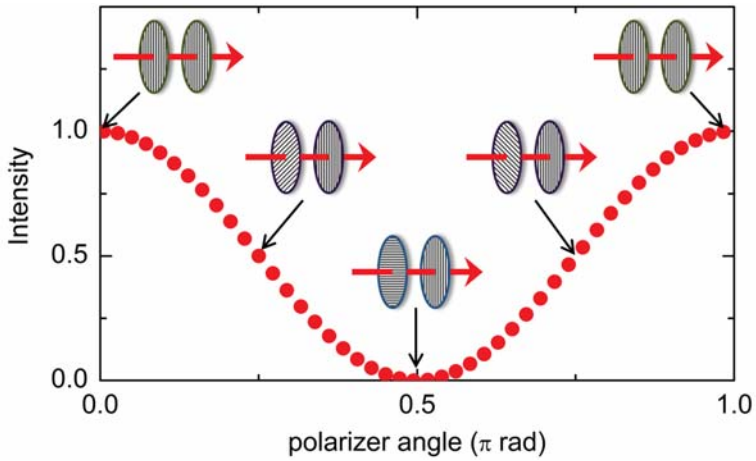

Figure 2.7: Model of the intensity of the light arriving at the detector when the polarizer is rotated 180° (π radian). The polarizer and analyzer are drawn schematically to indicated the configurations.

incident light is parallel to the analyzer angle. The minimum intensity is observed at $(1/2)\pi$ rad, exactly when polarizer and analyzer are crossed.

With a finite magnetic field switched on, the polarization state of the light that arrives at the detector is now influenced by the magneto-optical properties of the sample (Fig. 2.8b). For an arbitrary angle, ϕ, between polarizer and analyzer the intensity can be described using Jones vectors:

$$\begin{bmatrix} E_x \\ E_y \end{bmatrix}_{out} = \begin{bmatrix} 1 & 0 \\ 0 & 0 \end{bmatrix} \begin{bmatrix} t_{xx} & t_{xy} \\ -t_{xy} & t_{xx} \end{bmatrix} \begin{bmatrix} E_0 \cos\phi \\ E_0 \sin\phi \end{bmatrix}. \tag{2.52}$$

After adding all internal reflections and taking the square the intensity is found:

$$I(\phi) \propto \sum_j |t^j_{xx}|^2 \cos^2\phi + \sum_j (t^j_{xx} t^{j*}_{xy} + t^{j*}_{xx} t^j_{xy}) \cos\phi \sin\phi + \sum_j |t^j_{xy}|^2 \sin^2\phi, \tag{2.53}$$

Equation (2.53) can be rewritten by moving to double angles the following relations are found:

$$\begin{aligned} I(\phi) &\propto \frac{\sum_j |t^j_{xx}|^2 + \sum_j |t^j_{xy}|^2}{2} + \cos 2\phi \frac{\sum_j |t^j_{xx}|^2 - \sum_j |t^j_{xy}|^2}{2} + \sin 2\phi \frac{\sum_j (t^j_{xx} t^{j*}_{xy} + t^{j*}_{xx} t^j_{xy})}{2} \\ &= I_0 + I_1 \cos 2\phi + I_2 \sin 2\phi. \end{aligned} \tag{2.54}$$

where

$$\begin{aligned} I_0 &= \frac{\sum_j |t^j_{xx}|^2 + \sum_j |t^j_{xy}|^2}{2} \\ I_1 &= \frac{\sum_j |t^j_{xx}|^2 - \sum_j |t^j_{xy}|^2}{2} \\ I_2 &= \frac{\sum_j (t^j_{xx} t^{j*}_{xy} + t^{j*}_{xx} t^j_{xy})}{2}. \end{aligned} \tag{2.55}$$

This can be used to obtain the relation:

$$\tan 2\theta = \frac{\sum_j (t^j_{xx} t^{j*}_{xy} + t^{j*}_{xx} t^j_{xy})}{\sum_j |t^j_{xx}|^2 - \sum_j |t^j_{xy}|^2}. \tag{2.56}$$

With the use of $t_\pm = t_{xx} \pm i t_{xy}$, we arrive at:

$$\theta = \frac{1}{2} \arg \left(\sum_j t^j_- t^{j*}_+ \right). \tag{2.57}$$

To derive the relation between the conductivity of the thin film and θ, we develop the last expression. The transmission coefficients t^j_- and t^{j*}_+ (eqn. (2.43), see Fig. 2.1), expressed in the diagonal basis of circularly polarized light, are substituted in the expression for θ, after which the sum over all j rays is performed in the incoherent way. The real prefactor can be neglected, thus, the exact solution for the rotation is:

$$\theta = \frac{1}{2} \arg \left(\frac{t_{-,vfs} t^*_{+,vfs}}{1 - r_{-,sfv} r^*_{+,sfv} |r_{sv} \tau^2_s|^2} \right). \tag{2.58}$$

Again this expression is a function of the complex conductivity tensor, therefore we assume that the real part of the optical Hall conductivity is the dominating term and use the linear approximation, we obtain:

$$\theta \approx \frac{1}{n_s + 1} \frac{1 + \alpha^2 r^3}{1 - \alpha^2 r^4} \operatorname{Re} \left(Z_0 \sigma^f_{xy} \right). \tag{2.59}$$

This relation provides us with a direct relation between experimentally observed rotation and the real part of the optical Hall conductivity.

Note that in principle every internal reflected ray (see Fig. 2.1) has its individual Faraday rotation θ. Here we treated the substrate as incoherent, therefore the total observed rotation is in fact an average of the rotations for constructive interference and destructive interference. However, in the coherent case Fabry-Perot oscillations can be observed also in the Faraday rotation spectra [115].

Experimental method

The Faraday rotation spectra are measured using a set-up similar to the one described in the previous section. The important extra ingredients to enable the determination of the Faraday rotation are two gold grid-wire polarizers. The first one is placed right after the interferometer, but in front of the magnet, to linearly polarize the incident infrared light. The second polarizer is placed directly in between the magnet and the bolometer and functions as an analyzer of the polarization state of the transmitted light. Figure 2.8a shows the set-up used for the Faraday rotation measurements, including the rotating polarizer and the analyzer used to manipulate and analyze the polarization

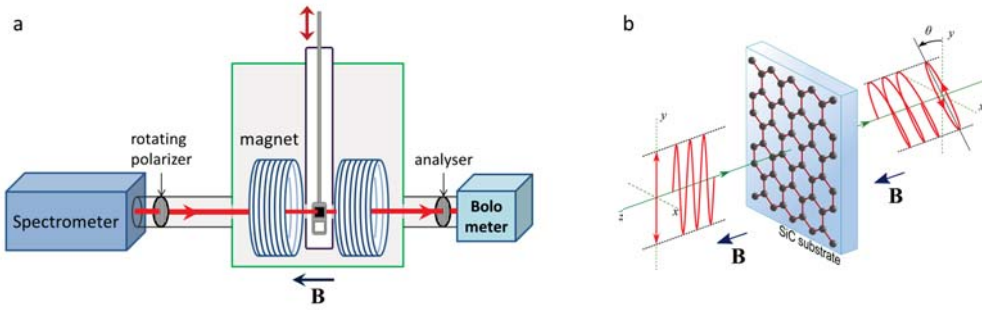

Figure 2.8: Schematics of the Faraday rotation set-up. a) The set-up of spectrometer, magnet and detector used for the transmission measurements is upgraded with two polarizers. b) The light impinging on the graphene sample is linearly polarized. While passing through the graphene in a perpendicular magnetic field, the polarization plane of the beam is rotated over an angle θ. Simultaneously, the light becomes elliptically polarized due to a difference in absorption of left and right handed circularly polarized light. The positive direction of the magnetic field is along the z-axis.

state of the light. With the addition of the two polarizers, effectively the set-up is most closely resembling a spectroscopic ellipsometry configuration. The influence of the sample in magnetic on the polarization state of the light is schematically represented in Fig. 2.8b.

The way to obtain the Faraday rotation angle for a fixed magnetic field is to measure optical spectra at a set of different polarizer angles, ϕ, and analyze the intensity dependence on ϕ. The polarizer angles are chosen such that a minimum in the intensity can be observed when the intensity is plotted as a function of polarizer angle. This 'intensity versus polarizer angle plot' is made for each frequency separately. An example of such a graph is shown in Fig. 2.9. The red arrows in the graph indicate the measurement order: the first spectrum is measured with a polarizer angle of 5° with respect to the vertical, the second measurement is taken at 115°, the third spectrum is measured at 10° and so on. This 'zig-zag' measuring order was introduced to compensate for possible drifts in the signal over time, which would introduce a systematic error in the 'intensity versus polarizer angle plot'. After measurements have been taken at all polarizer angles, the 'zig-zag' procedure is repeated in reverse order, starting with the last measured angle, the blue arrows in Fig. 2.9 indicate this reverse measurement. In total every polarizer angle is measured twice and when analyzing the data, the average of the intensities measured at each polarizer angle is used.

Apart from drift in the signal, also the presence of (depolarizing) windows and the non-ideal random polarization of the source must be taken into account. Therefore, for the used set of polarizer angles, an additional calibration measurement is made: the sample and the analyzer are removed from the set-up and transmission spectra are taken at each polarizer angle, using the same 'zig-zag' method as described above.

Figure 2.10a shows the light intensity as a function of polarizer angle for an energy of 15 meV, measured on single layer graphene grown on the silicon side of SiC

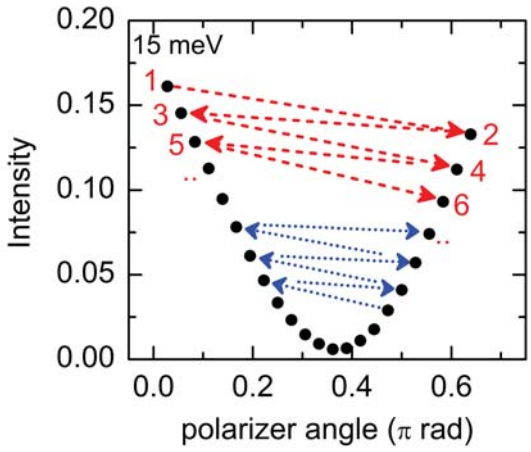

Figure 2.9: An example of a measurement of the intensities of the signal, plotted as a function of polarizer angle. The red and blue arrows indicate the order of measurements done.

(see Chapter 6.5.1): the red triangles and black circles are measured with the sample in place and correspond to fields of 7 and -7 T respectively. The blue triangles correspond to the (scaled) intensity measured without analyzer and sample and reveals the polarization dependence of the experimental set-up, unique at every energy, shown here for 15 meV. In a next step, the intensities measured (at finite field) on the sample are normalized to the set-up calibration curve. In Fig. 2.10b the normalized intensities for 7 and -7 T are plotted, the solid lines correspond to a fit with a sine wave, used to determine polarizer angle at which the intensity is minimum.

The inset in Fig. 2.10b shows a close up of the data and the fits near the minimal intensities. The Faraday angle θ can be found from the fits by determining the angle at which the intensity is smallest for both positive and negative magnetic field. The difference between the 'minimum intensity angles' at positive and negative field corresponds to 2 $\times\theta$ (here for 15 meV) and a field of 7 T).

Once the Faraday angle is found for a particular frequency, the normalization of the intensity plots by the calibration curve and the fitting of the normalized intensity plots is repeated for every energy for both positive and negative field, in this way complete Faraday rotation angle spectra can be obtained.

Figure 2.10c shows the 'minimum intensity angles' for both +7 (red) and -7 T (black) for the full energy range. The curves show strong oscillations caused by the windows in the set-up. However, the influences of the windows are independent of the sign of the magnetic field, while the rotation due to the sample is antisymmetric with magnetic field. Therefore we take the difference in 'minimum intensity angles' at positive and negative field effectively canceling all symmetric effects. The difference between the curves shown in Fig. 2.10c, divided by two, is shown in Fig. 2.10d and corresponds to the Faraday angle measured on single layer epitaxial graphene at 7 T.

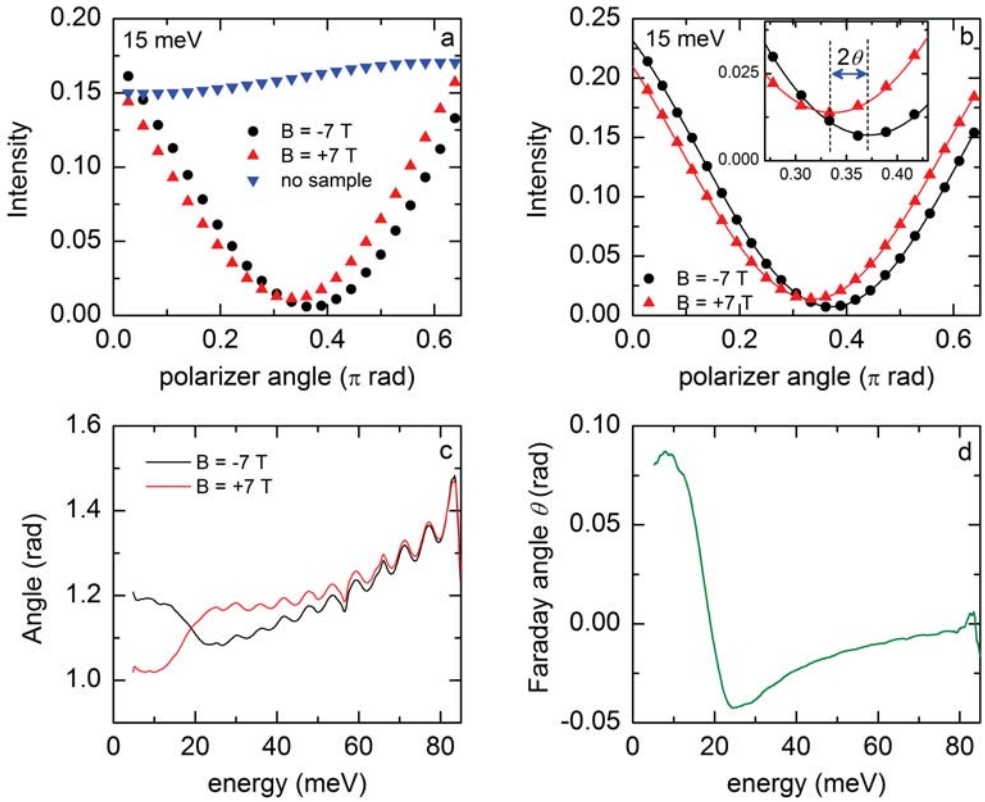

Figure 2.10: Model of the intensity of the light arriving at the detector when the polarizer is rotated a full turn. The polarizer and analyzer are drawn schematically to indicated their orientation.

3

Graphene, a truly two-dimensional material

3.1 Introduction

Graphene is an one atom thick sheet of carbon atoms arranged in the famous honeycomb crystal lattice. Each carbon atom has six electrons, two of which are forming a closed $1s^2$ shell, the remaining four fill 2s and 2p states. Three of the valence electrons are involved in sp^2 hybridized orbitals, which form in-plane σ bonds to the three nearest neighbors. The carbon-carbon distance is 1.42 Å and the bond angle is 120°. The σ bonds are responsible for the structure of graphene and for its unusual mechanical and thermal properties [116]. The fourth valence electron remains in the half-filled $2p_z$ orbital orthogonal to the graphene plane and forms a π bond by overlapping with other $2p_z$ orbitals. These delocalized π electrons determine the famous electronic properties of graphene [31].

In this chapter we will discuss the electronic and optical properties of single layer graphene. The discussion is divided into three main sections, the first, section 3.2, introducing graphene without any kind of external field. The second part, section 3.3, is focussed on the properties of graphene in an externally applied magnetic field. Both sections end with a discussion of the optical and magneto-optical properties.

The last section of this chapter focuses on the different synthesis methods of graphene. The type of graphene sample used for the experiments in this work is epitaxial graphene grown on SiC. In section 3.4.1 the synthesis and the properties of single layer graphene grown on silicon faced SiC are discussed, while the subject of section 3.4.2 is the synthesis and the properties of rotationally stacked multilayer graphene grown on carbon faced SiC.

3.2 Graphene, without external fields applied

3.2.1 Tight-binding approach

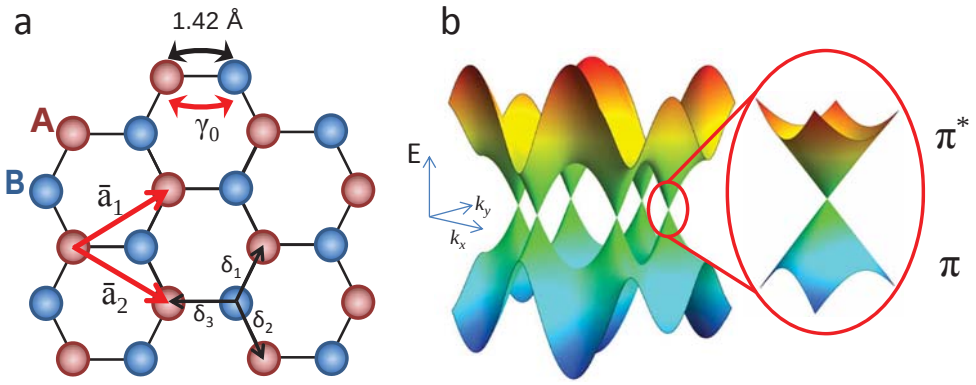

Figure 3.1: (a) Schematic representation of the honeycomb structure of the carbon atoms in single layer graphene. (b) The tight-binding electronic band structure, the inset shows the two linear π bands which cross at the Dirac point.

The hexagonal lattice of carbon atoms can be regarded as two offset triangular sublattices A and B, as is schematically shown in Fig. 3.1a. The lattice vectors $\mathbf{a_1}$ and $\mathbf{a_2}$, in real space, are:

$$\mathbf{a_1} = \frac{a}{2}(3, \sqrt{3}), \qquad \mathbf{a_2} = \frac{a}{2}(3, -\sqrt{3}). \tag{3.1}$$

where a is the nearest neighbor distance (1.42 Å). The nearest neighbor vectors, indicated in Fig. 3.1a as δ_1, δ_2 and δ_3, are given by:

$$\delta_1 = \frac{a}{2}(1, \sqrt{3}), \quad \delta_2 = \frac{a}{2}(1, -\sqrt{3}), \quad \delta_3 = \frac{a}{2}(-1, 0). \tag{3.2}$$

Wallace was the first to use the standard tight binding approach to calculate the electronic states of graphene [2], considering only the nearest-neighbor hopping parameter γ_0. The tight-binding Hamiltonian is a 2×2 matrix [2, 27, 117]:

$$H(\mathbf{k}) = \begin{pmatrix} 0 & \gamma_0 S(\mathbf{k}) \\ \gamma_0 S^*(\mathbf{k}) & 0 \end{pmatrix} \tag{3.3}$$

where $\mathbf{k}$ is the wave vector and $S(\mathbf{k})$ is the overlap integral:

$$S(\mathbf{k}) = \sum_{\delta} \exp i\mathbf{k}\delta = 2\exp\frac{ik_x a}{2} \cos\frac{k_y\sqrt{3}a}{2} + \exp(-ik_x a). \tag{3.4}$$

The energies of the two π bands are found to be:

$$\begin{aligned} E_{\pi^*}(\mathbf{k}) &= -E_{\pi}(\mathbf{k}) \\ &= \gamma_0 \sqrt{3 + 2\cos\left(k_y\sqrt{3}a\right) + 4\cos\left(\tfrac{k_y\sqrt{3}a}{2}\right)\cos\left(\tfrac{k_x 3a}{2}\right)}. \end{aligned} \tag{3.5}$$

The electronic band structure described by eqn. (3.5) is shown in Fig. 3.1b. Importantly, the two π bands cross at the inequivalent K and K' points of the Brillouin zone, exactly at zero energy. In momentum space, positions of the K and K' points are $\left(\frac{2\pi}{3a}, \frac{2\pi}{3\sqrt{3}a}\right)$ and $\left(\frac{2\pi}{3a}, -\frac{2\pi}{3\sqrt{3}a}\right)$, respectively. The Hamiltonian can be expanded near the K and K' points:

$$H_{K,K'}(\mathbf{q}) = \hbar v_F \begin{pmatrix} 0 & q_x \mp i q_y \\ q_x \pm i q_y & 0 \end{pmatrix} \tag{3.6}$$

where $v_F = 3a\gamma_0/2$ is the energy independent Fermi velocity and $\mathbf{q}$ is the momentum measured with respect to the K and K' points. Hamiltonian (3.6) is equivalent to the Dirac-Weyl equation in 2D, which is used to describe particles with zero rest mass (relativistic) of spin 1/2 and with a Fermi velocity v_F. For this reason, the low energy quasiparticles in graphene are often referred to as "massless Dirac fermions". The K and K' points are the so-called Dirac points, close to which the band structure is effectively described by Hamiltonian (3.6). The band energies following from the eigen values of Hamiltonian (3.6):

$$E_{\pi^*}(\mathbf{k}) = -E_{\pi}(\mathbf{k}) \approx v_F \hbar |\mathbf{q}|, \tag{3.7}$$

Since pristine graphene has one electron per carbon in the π band, at charge neutrality, this results in half filled bands. In this case, the Fermi energy lies at the Dirac point (or charge-neutrality point). Although the density of states at the Dirac point is zero, electrons from the hole bands (below the Dirac point) can be excited to the electron bands (just above the Dirac point) with zero excitation energy, therefore pristine graphene is a zero-gap semiconductor.

The wave functions describing the bands near the K point are [31]:

$$\Psi_K^{\pm}(\theta_{\mathbf{q}}) = \frac{1}{\sqrt{2}} \begin{pmatrix} e^{i\theta_q/2} \\ \pm e^{-i\theta_q/2} \end{pmatrix}, \tag{3.8}$$

where $\pm$ corresponds to the positive and negative solution for the two π bands and $\theta_q = \arctan(\theta_x/\theta_y)$ is the angle in momentum space. Importantly, the wave function changes sign under a 2π rotation in k-space: $\Psi_K^{\pm}(\theta_{\mathbf{q}}) = -\Psi_K^{\pm}(\theta_{\mathbf{q}} + 2\pi)$. The phase difference for this cyclic loop is π and is often referred to as a Berry's phase [118]. A direct consequence of the Berry's phase in graphene is the existence of a zero energy Landau level and the Anomalous Quantum Hall effect, where the steps in the conductivity are shifted by 1/2 with respect to the usual Quantum Hall effect [47, 48].

3.2.2 Ambipolar doping

In 2D electron gases the quadratic energy dispersion gives rise to a constant density of states (DOS) [119]. The linear dispersion of the electronic bands in graphene gives

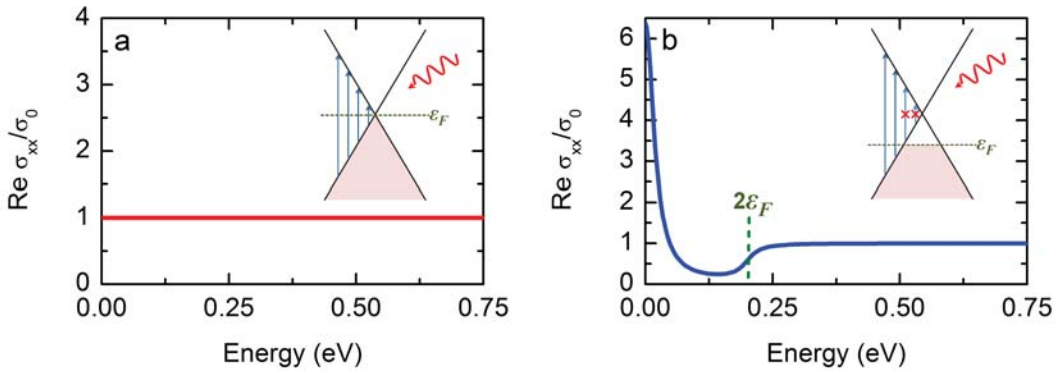

Figure 3.2: Model of the real part of the optical conductivity of (a) undoped and (b) doped single layer graphene, with the Fermi level 100 meV below the Dirac point, a broadening of 10 meV and at T = 10 K. The insets show the permitted optical transitions between hole and electron bands.

rise to a strikingly different picture: the DOS is linearly dependent on the energy ϵ (measured with respect to the Dirac point), and vanishes at the Dirac point [2]:

$$\rho(\epsilon) = \frac{g_s g_v |\epsilon|}{2\pi v_F^2 \hbar^2}, \tag{3.9}$$

where $g_s = g_v = 2$, are the spin and valley degeneracies, respectively. The carrier density, n, is found by integrating the DOS up to the Fermi energy, ϵ_F:

$$n = \frac{\epsilon_F^2}{\pi v_F^2 \hbar^2}. \tag{3.10}$$

Due to the fact that graphene is only one, or just a few, atomic layers thick, it can be doped easily using an external gate, ionic liquids or by other external influences like surface contamination or simply by being in the vicinity of polar material. Importantly, due to the electron-hole symmetry of the bands and DOS, the Fermi energy can be shifted through the Dirac point to select hole or electron doping, which is referred to as ambipolar doping [1, 120]. An external gate and ionic liquid gating offer active control over the carrier concentration in graphene, so that the Fermi energy can be tuned continuously through zero energy. In contrast, surface contamination or the presence of a substrate often shifts the Fermi level (far) away from charge neutrality. As we shall see, it is vital to take the doping level and the sign of the charge carriers into account when discussing the (magneto)-optical properties of graphene.

3.2.3 Optical properties

The relativistic low energy band dispersion of monolayer graphene gives rise to an optical conductivity with a universal value, $\sigma_0 = e^2/4\hbar$, which is, at zero temperature,

independent of frequency: [30, 38, 39, 42, 46, 121, 122]

$$\mathrm{Re}\,\sigma(\omega) = \sigma_0 \equiv \frac{e^2}{4\hbar}. \tag{3.11}$$

Figure 3.2a shows the universal conductivity of a single graphene layer for infrared photon energies up to 0.75 eV. The inset shows schematically the π bands near the Dirac point, the hole bands are occupied, while the electron bands are empty. The arrows indicate the allowed optical transitions.

The transmission of the graphene film can be found using the Fresnel equations in the thin film limit, where $d_{film} \ll \lambda$ (third relation of eqn. (2.41)). For free standing graphene, $N_s = 1$ and the transmission coefficient is:

$$t = \frac{2}{2 + \frac{4\pi}{c}\sigma} = \frac{2}{2 + \pi\alpha}, \tag{3.12}$$

where α is the fine structure constant: $\alpha = e^2/\hbar c$. The transmission, $T = |t|^2$, of free standing single graphene therefore is also frequency independent and can be expressed as:

$$T = \left(1 + \frac{\pi\alpha}{2}\right)^{-2} \approx 1 - \pi\alpha \approx 0.977. \tag{3.13}$$

The absorption of the free standing film is $1-T$ = 2.3%, and is strikingly large for a single atomic layer [38, 39]. Therefore it is possible to see graphene with the bare eye and identify the number of layers of a sample by just an easy, straightforward, optical measurement under a microscope. However, this is strictly valid in the case that the Fermi level lies exactly at the Dirac point.

Due to the presence of a substrate, the application of an external gate or surface contamination, the Fermi level is often shifted away from the Dirac point. Figure 3.2**b** shows the optical response for (hole) doped single layer graphene with ϵ_F = -100 meV, a broadening, γ, of 10 meV and at T = 10 K. The inset shows a schematic representation of the π bands, the shifted Fermi energy and the allowed optical transitions. In the spectrum the optical response of free carriers, or intraband transitions, can be observed in the form of a Drude peak centered around zero energy. At higher energies, but below a threshold of twice the Fermi level ϵ_F, the optical response is small, because optical transitions between the electron and hole bands, interband transitions, are blocked [30, 42, 46, 121, 122]. Interband transitions are allowed above $\hbar\omega = 2|\epsilon_F|$, therefore the optical conductivity shows an onset at this value, while at energies above $2|\epsilon_F|$ the conductivity converges to the universal conductivity σ_0. At even higher photon energies the conductivity strongly deviates from the universal conductivity due to the presence of a van Hove singularity in the DOS. The resulting peak in the optical conductivity however, is modified by excitonic effects, therefore the peak has a Fano-like line shape [97, 123, 124].

3.3 Graphene in magnetic field

By turning on a perpendicular magnetic field, electronic bands split up in quantized energy levels, called Landau levels (LLs). For a quadratic dispersion, the Landau levels are equally spaced, are linearly dependent on magnetic field B and inversely proportional to the cyclotron resonance mass, $m_c = eB/\omega_c$ [50, 119, 125, 126]. The relativistic dispersion of graphene gives rise to a very different Landau level spectrum; the energies of Landau levels show a square root dependence on both Landau level number n and B [30, 117]. As a result of this non-equidistant spacing of the Landau levels, a spectacular series of absorption peaks, corresponding to transitions between various levels can be observed in optical experiments [53, 54, 58, 127]. Another typical property of graphene in a magnetic field is the existence of a Landau level (n = 0) at zero energy, which is degenerate in electrons and holes. As a consequence, graphene shows the half-integer quantum Hall effect [45, 46], first observed in exfoliated graphene flakes [47, 48] and later in graphene epitaxially grown on SiC [78, 79, 128].

3.3.1 Landau levels: quantum regime

The energies of the discrete Landau levels can be found by considering Hamiltonian (3.6) with an additional electromagnetic (EM) perturbation [129]:

$$\mathbf{p} \Longrightarrow \mathbf{\Pi} = \mathbf{p} + e\mathbf{A}(\mathbf{r}), \tag{3.14}$$

where $\mathbf{A}(\mathbf{r})$ is a vector potential generating the magnetic field B. Replacing the momentum $\mathbf{p}$ with eqn. (3.14) is called a Peierls substitution and is valid as long as the magnetic length, l_B

$$l_B = \sqrt{\frac{\hbar}{eB}}, \tag{3.15}$$

is much larger than the lattice spacing $= \sqrt{3}a = 0.24$ nm.

With the help of commutation relations the momentum operators Π_x and Π_y can be related to the ladder operators:

$$\mathbf{\Pi}_- = \mathbf{\Pi_x} - i\mathbf{\Pi_y} = \frac{\sqrt{2}\hbar}{l_b}\mathbf{b}, \tag{3.16}$$

$$\mathbf{\Pi}_+ = \mathbf{\Pi_x} + i\mathbf{\Pi_y} = \frac{\sqrt{2}\hbar}{l_b}\mathbf{b}^\dagger. \tag{3.17}$$

These expressions are than substituted in the Hamiltonian in the absence of field. Considering only the π electrons, eqns. (3.16) and (3.17) replace $\mathbf{p} = \hbar\mathbf{q}$ in Hamiltonian (3.6):

$$H_B = \frac{\sqrt{2}\hbar v_F}{l_b}\begin{pmatrix} 0 & \mathbf{b} \\ \mathbf{b}^\dagger & 0 \end{pmatrix}. \tag{3.18}$$

The eigen values and states can be found by solving the systems of equations:

$$\frac{\sqrt{2}\hbar v_F}{l_b}\mathbf{b}\psi_1 = E\psi_2, \tag{3.19}$$

$$\frac{\sqrt{2}\hbar v_F}{l_b}\mathbf{b}^\dagger\psi_2 = E\psi_1. \tag{3.20}$$

If $\mathbf{b}^\dagger$ acts on eqn. (3.19), we find:

$$\mathbf{b}^\dagger\mathbf{b}\psi_1 = \left(\frac{El_B}{\sqrt{2}\hbar v_F}\right)^2\psi_1, \tag{3.21}$$

where $\mathbf{b}^\dagger\mathbf{b}$ is the number operator: $\mathbf{b}^\dagger\mathbf{b}|n\rangle = n|n\rangle$. The square of the energy E is a function of n, therefore discreet energy levels, so-called Landau levels, are found [30, 117]:

$$E_n = \mathrm{sgn}(n)\sqrt{2|n|}\frac{\hbar v_F}{l_b} = \mathrm{sgn}(n)\sqrt{2\hbar v_F^2|enB|}, \tag{3.22}$$

where n is the LL number, which is a positive integer for electron-like LLs and a negative integer for hole-like LLs and e is the electron charge. Note that the symbol n is also used for carrier density. From eqn. (3.22) follows that for the level with $n = 0$ the LL energy $E_0 = 0$, moreover, due to electron-hole symmetry, the $n = 0$ LL is degenerate for both electrons and holes. In addition, the LLs spectrum is non-equidistant. The LL energies following from eqn. (3.22) are shown in Fig. 3.4 as a function of magnetic field, for $n = \pm1, \pm2, ...\pm7$.

3.3.2 Cyclotron resonance: classical regime

Charge carriers can be excited from a filled Landau level, below the Fermi energy, to an empty LL, above the Fermi energy, on the condition that the absolute difference in LL number n is equal to one. Since the LLs are non-equidistant, a different doping level results in a change in the transition energy, or cyclotron resonance energy. If the LLs close to the Fermi energy have high quantum number, the so-called quasi-classical cyclotron is observed, which is typically for highly doped graphene. On the contrary, in low doped graphene the LLs close to the Fermi energy have small quantum number, therefore the transitions are in the quantum regime. In this case, the typical square-root dependence of the LL transition energy on the applied magnetic field can be observed.

In Fig. 3.3 examples of cyclotron resonance transitions are shown. The Fermi energy, indicated by the green dashed line, is shifted away from charge neutrality, as is the case in highly (electron) doped graphene. The blue arrows show the allowed transitions between the LLs for various magnetic fields. For clarity, only LLs with n up to 20 are shown. The observed transitions take place between LLs with high index, therefore these excitations give rise to semi-classical cyclotron resonance. In practice, in many graphene samples the doping level is shifted far away from the Dirac point,

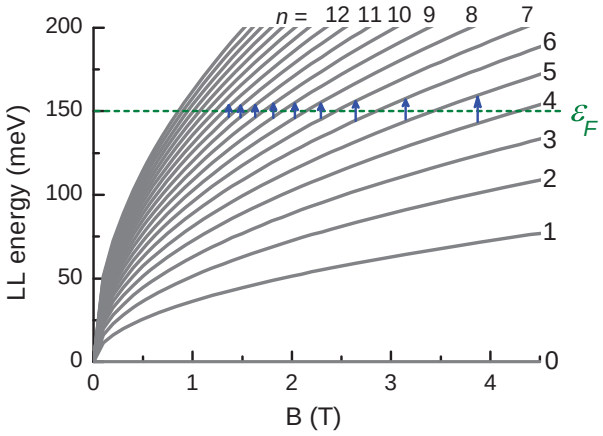

Figure 3.3: Schematic representation of the electron-like Landau levels (up to n = 20) for single layer graphene, with v_F = 10^6 m/s. The Fermi energy, indicated by the green dashed line, is shifted far away from the Dirac point. The blue arrows correspond to cyclotron resonance transitions between Landau levels, shown here starting from the 12→13 transition, for clarity the transitions for lower magnetic fields are not shown, but are allowed.

therefore quasi-classical cyclotron resonance is often observed even at very high fields (B ∼10 T).

Quasi-classical cyclotron resonance can be described using the cyclotron mass m_c, which is given by [130]:

$$m_c = \frac{\hbar^2}{2\pi}\left[\frac{\partial A(E)}{\partial E}\right]_{\epsilon_F}, \tag{3.23}$$

where $A(E) = \pi q(E)^2$, is the momentum space area enclosed by the orbit of energy E. With the linear band dispersion, eqn. (3.7), the area can be expressed as $A(E) = \pi(E/(v_F\hbar))^2$, and the cyclotron mass becomes:

$$m_c = \frac{\epsilon_F}{v_F^2}. \tag{3.24}$$

The cyclotron resonance energy is described by the expression for classical cyclotron resonance, $\omega_c = eB/m_c$. Thus, the cyclotron resonance energy in highly doped graphene is dependent on the Fermi velocity and inversely dependent on the Fermi energy [30, 127]:

$$\omega_c = \frac{eBv_F^2}{\epsilon_F}. \tag{3.25}$$

Importantly, eqn. (3.25) shows that, in the semi-classical regime, ω_c is linearly dependent on the magnetic field.

3.3.3 Magneto-optical properties

Experimentally, the Landau levels in graphene have been observed in the form of optical transitions between full and empty Landau levels in infrared spectroscopy exper-

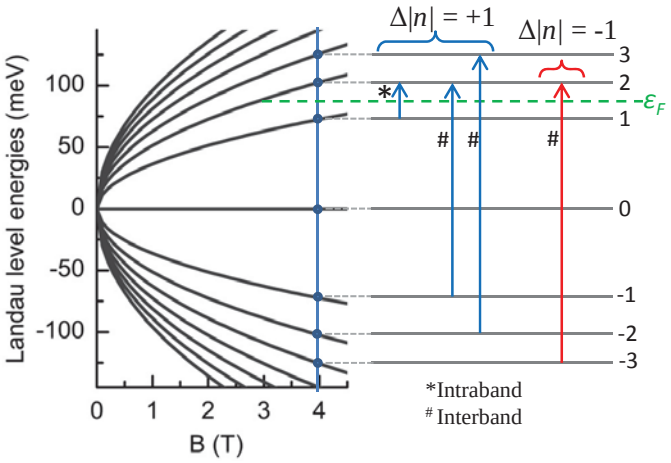

Figure 3.4: Model of the Landau level energies showing the typical square-root like dependence on magnetic field, levels $n = 0, \pm1, \pm2, ...\pm7$ are shown. The green dashed line indicates the Fermi level. Allowed optical transitions between the LLs are shown as arrows. The blue arrows correspond to the selection rule $\Delta|n| = +1$, while the red arrow corresponds to $\Delta|n| = -1$. The transition corresponding to the blue arrow labeled with $*$ is an intraband transition, while the arrows labeled with the $\sharp$ symbol are interband transitions.

iments [53, 54] and directly by scanning tunneling spectroscopy experiments [56, 57]. Since the Landau levels in graphene are not equidistant, a spectacular series of peaks at different frequencies can be observed in the infrared absorption spectra. The optical transitions between the LLs in graphene can be of two types: interband transitions, where carriers from the hole-like LLs are excited to the electron-like LLs and intraband transitions, where carriers from the filled hole(electron)-like LLs are excited to empty hole(electron)-like LLs. Since in graphene the hole and electron bands have the same symmetry, the selection rule for the optical transitions between the initial LL (n_i) and the final LL (n_f) is the same for both the intra- and interband transition, which is [131, 132]:

$$\Delta|n| = |n_f| - |n_i| = \pm 1, \tag{3.26}$$

In Fig. 3.4 an example of the allowed optical transitions between LLs is shown in the case of electron doping, with: $\epsilon_1 < \epsilon_F < \epsilon_2$. The blue arrows in Fig. 3.4 all correspond to transitions with $\Delta|n| = +1$, while the red arrow is an example of a transitions with $\Delta|n| = -1$. The excitation from the filled $n = 1$ LL to the empty $n = 2$ LL corresponds to an intraband transition, indicated by the $*$. For the intraband transitions the sign of $\Delta|n|$ signals the type of doping: interband transitions with $\Delta|n| = -1$ are only allowed when $\epsilon_F < 0$: p-doping. All other transitions, labeled with $\sharp$, are interband transitions.

The optical conductivity of graphene in a magnetic field can be obtained using the Kubo formalism, detailed in section 2.2.3. Relatively simple analytical expressions for $\sigma_{xx}(\omega, B)$ and $\sigma_{xy}(\omega, B)$ can be obtained when the scattering width, γ, is

assumed to be independent of Landau level number and assumed to be independent on frequency [127, 131]:

$$\begin{aligned}\sigma_{xx}(\omega, B) =& \frac{e^2 v_F^2 |eB|(\hbar\omega + i\gamma)}{\pi c i} \times \\ & \sum_{n=0}^{\infty} \left\{ \frac{[f(E_n) - f(E_{n+1})] + [f(-E_{n+1}) - f(-E_n)]}{(E_{n+1} - E_n)^2 - (\hbar\omega + i\gamma)^2} \frac{1}{E_{n+1} - E_n} \right. \\ & \left. + \frac{[f(-E_n) - f(E_{n+1})] + [f(-E_{n+1}) - f(E_n)]}{(E_{n+1} + E_n)^2 - (\hbar\omega + i\gamma)^2} \frac{1}{E_{n+1} + E_n} \right\},\end{aligned} \tag{3.27}$$

And for $\sigma_{xy}(\omega, B)$ the Kubo formalism results in:

$$\begin{aligned}\sigma_{xy}(\omega, B) =& \frac{e^2 v_F^2 eB}{\pi} \sum_{n=0}^{\infty} ([f(E_n) - f(E_{n+1})] - [f(-E_{n+1}) - f(-E_n)]) \times \\ & \left\{ \frac{1}{(E_{n+1} - E_n)^2 - (\hbar\omega + i\gamma)^2} + \frac{1}{(E_{n+1} + E_n)^2 - (\hbar\omega + i\gamma)^2} \right\}.\end{aligned} \tag{3.28}$$

where $f(E_n) = 1/[\exp((E_n - \epsilon_F)/T) + 1]$, is the Fermi distribution and E_n is the energy of the n^{th} LL, given by eqn. (3.22). The expression for $\sigma_{xx}(\omega, B)$ is an even function of ϵ_F, magnetic field B and frequency ω. $\sigma_{xy}(\omega, B)$ is an odd function of ϵ_F, B and ω. A direct consequence of the odd symmetry is that for half filling of the zero LL: $\epsilon_F = 0$, the optical Hall conductivity $\sigma_{xy}(\omega, B) = 0$.

Figure 3.5b shows $\sigma_{xx}(\omega, B)$ obtained from eqn. (3.27) with $\epsilon_1 < \epsilon_f < \epsilon_2$, v_f = 10^6 m/s, a field of 4 T and a scattering width of 10 meV. The corresponding LLs and the optical excitations are shown in Fig. 3.5a. In the spectrum, peaks centered around the transition energies are observed. At high energies, the transitions become closer in energy, so that the peaks merge and the conductivity converges to the universal conductivity.

Figure 3.5d shows the optical Hall conductivity obtained using eqn. (3.28), corresponding to the LL system shown in panel **a**. Spectral features can be observed at the transition energies of the $1 \to 2$ and the $-1 \to 2$; the inflection points at the center of the spectral features coincide with the transition energies. However, at higher energies the transitions cancel out and therefore, $\sigma_{xy}(\omega, B)$ goes to zero. This cancelation is due to the fact that the spectral feature resulting from a transition with $\Delta n = +1$ is precisely opposite in sign to the feature stemming from the transition with $\Delta n = -1$. Since, at high energies both the $-n \to n + 1$ and the $-n - 1 \to n$ transitions are allowed, their combined contribution to $\sigma_{xy}(\omega, B)$ is zero. Importantly, the sign of the slope at the resonance energy reveals the type of charge carrier. For electron doping (as in this example) the slope is positive, while for p-doped graphene the spectral feature has a negative slope at the resonance energy.

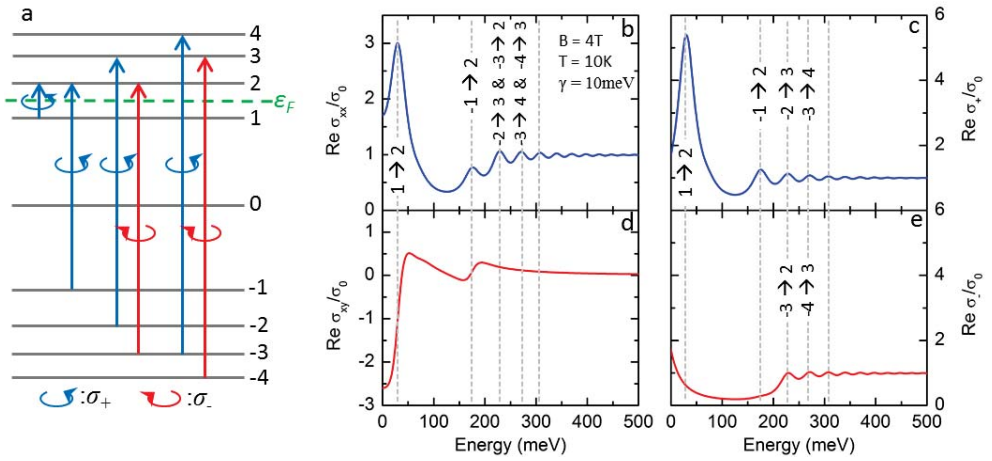

Figure 3.5: (a) Schematic representation of the Landau level energies, levels $n = 0$, ± 1, ...± 4 are shown. The green dashed line indicates the Fermi level. Allowed optical transitions between LLs are shown as arrows. The blue arrows correspond to absorption of RCPL (left handed circularly polarized light), while the red arrow corresponds to absorption of LCPL (left handed circularly polarized light). (b) The real part of the optical conductivity, resulting from the system shown schematically in (a). (c) The real part of the conductivity in the basis of RCPL. (d) The real part of the optical Hall conductivity. (e) The real part of the conductivity in the basis of LCPL.

The optical conductivity in the basis of circularly polarization can be obtained from $\sigma_{xx}(\omega, B)$ and $\sigma_{xy}(\omega, B)$ using the relation $\sigma_{\pm} = \sigma_{xx} \pm i\sigma_{xy}$. In Fig. (3.5)c and e, the real part of $\sigma_+(\omega, B)$ and $\sigma_-(\omega, B)$ are shown for the LL system shown schematically in panel a. The peaks observed in $\sigma_+(\omega, B)$ originate from the transitions with $\Delta n = +1$ and correspond to the absorption of right-handed circularly polarized light (RCPL). On the contrary, peaks observed in $\sigma_-(\omega, B)$ originate from the transitions with $\Delta n = -1$ and correspond to the absorption of left-handed circularly polarized light (LCPL).

In the classical regime where the cyclotron resonance is linearly dependent on the external magnetic field (see section 3.3.2), expressions for the optical conductivity can be obtained from the Kubo formula by studying the weak field limit [122]. Similar relations for the optical conductivity in the classical regime can be obtained using Boltzmann's theory of transport [133]. It was shown that the spectral shape of the optical excitations in the diagonal and off-diagonal components of the optical conductivity tensor are described by the Drude-lorentz model [122, 133], discussed in section 2.2.2 (eqns. (2.27) and (2.28)).

3.4 Graphene synthesis

Graphene was first isolated using the famous 'scotch-tape technique' in 2004 [1]. In this method thin layers of carbon are removed from graphite crystals with scotch tape.

Then the layers on the scotch tape are thinned down further by e.g. folding the tape several times, effectively cleaving the flakes. Finally the scotch is pressed onto a substrate and removed again, leaving behind a few or just one layer of carbon.

A typical substrate used is doped silicon with an insulating layer of SiO_2, which enhances the visibility of the flakes on the substrate and functions as a gate dielectric for electric field effect measurements. However, other substrates can be used like quartz, diamond, chlorinated silicon, TEM grids etc. A promising substrate, only recently applied successfully, are thin flakes of boron nitrite (BN) [134], which is insulating and has a honeycomb structure with a lattice constant close to the one of graphene. Although the deposition of exfoliated graphene on (also) exfoliated BN results in even smaller samples, the quality, and in particular the mobility, of the graphene is convincingly higher.

After the deposition of the exfoliated flakes on the substrate, the samples are searched for under a microscope, which can be quite a lengthy work due to the small sample size. The number of layers of the selected flakes can be determined by optical contrast [38, 39], by Raman spectroscopy [135] or by atomic force microscopy (AFM). The size of the flakes forms the main challenge when working with this technique: most flakes are just a few micrometer, larger flakes of about 100 micron width can be found, but these are rare. However, exfoliation provides the highest quality samples with single crystal domains, specifically now with the successful employment of BN as a substrate. In addition, the 'scotch-tape technique' proves to be a method feasible in any lab equipped with an optical microscope and scotch tape, and therefore is one of the most used synthesis technique to produce graphene.

The successful implementation of graphene in future commercial applications in (nano) technology, strongly depends on the feasibility and costs of large-scale fabrication. With this in mind, many groups (and companies) focussed their work on finding a recipe to grow graphene on an unlimited scale. Many different approached have been demonstrated, from which commonly used methods are now: Chemical Vapor Deposition (CVD) on metal foils [62–66] and the graphitization of SiC [3, 70]. Other synthesis methods, not discussed here, include molecular beam epitaxy (MBE), the un-zipping of carbon nanotubes and cleaving graphite in liquids.

CVD of carbon on metal foils of copper or nickel can produce large scale graphene sheets of relatively high quality. To grow the graphene, a metal, used as a catalyst, is placed in a furnace in which a carbon gas flow is directed to the metal surface. At high temperature the carbon is absorbed by the metal surface, however, when cooling down, the carbon is released by the metal forming a graphene layer on top of the metal. The source of carbon can be almost anything, but typically used sources include methane, ethylene and solids like poly methyl methacrylate (PMMA). After growth, the metal is etched away and the film can be transferred to an arbitrary (insulating) substrate using a polymer like PMMA or PDMS, applied on the graphene film in advance. Typically, the mobility of CVD grown graphene ranges between 1000 and 7000 cm^2/Vs and due to the transfer between the metal foil and insulating substrate the films tend to be doped.

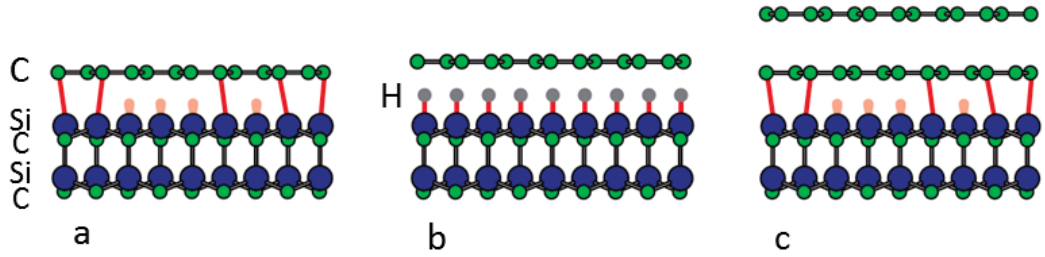

Figure 3.6: (a) Bufferlayer (b) Hydrogen passivation transforms the bufferlayer into a graphene layer. (c) Graphene on top of a bufferlayer. These figures are reproduced from Ref [71].

Epitaxial growth of graphene on silicon carbide (SiC) provides a second route to obtain large scale graphene. One of the advantages of this synthesis technique is that samples are directly grown on insulating, transparent SiC. The SiC is annealed at around 1500°C, either in vacuum or an argon atmosphere. At this temperature the silicon is desorbed from the SiC, leaving behind an excess of carbon which forms layers of graphene on the SiC surface. However, a nuance should be made: SiC is a polar material consisting of layers of silicon and carbon, therefore, the surface can be terminated at either the silicon (SiC(0001)) or the carbon (SiC(000$\bar{1}$)) side, which strongly influences the sublimation process and ultimately, the growth of the graphene layers. For this reason, in the next sections and chapters a distinction is made between epitaxial graphene on the C-side and on the Si-face.

After the CVD growth or exfoliation of graphene flakes additional steps can be taken for the specific needs of the experiment. The graphene layer can be transferred to a suitable substrate, electrical contacts can be applied by lithography and freely suspended graphene can be obtained by etching away the substrate. In addition, the sample can be annealed to reduce surface contamination, or the reverse: ad-atoms can be applied to actively influence the doping level of the graphene.

The experimental work presented in this thesis is performed on graphene epitaxially grown on SiC. Therefore, the next sections are focussed specifically on the properties and preparation of epitaxial graphene grown on the Si-side (section 3.4.1) and the C-side ((section 3.4.2)) of SiC.

3.4.1 Single layer graphene on SiC(0001)

As mentioned above, the surface termination of SiC strongly influences the epitaxial growth of graphene on SiC. The graphitization of the silicon terminated side of SiC is a slow and self-limited process, for which high temperatures, between 1150 and 1450°C, are required [69]. The self limiting nature of the growth makes it easy to obtain one single carbon layer, the so-called buffer layer, shown in Fig. 3.6a. The buffer layer

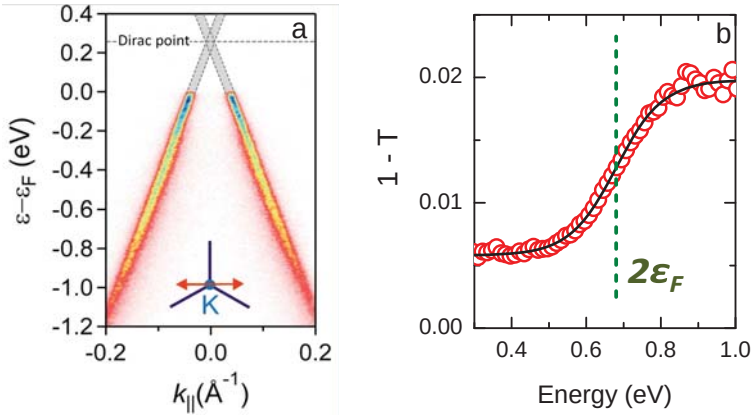

Figure 3.7: (a) ARPES data on a hydrogen intercalated monolayer epitaxial graphene sample. (b) Optical absorption, $1 - T$, in the mid infrared range showing the onset of optical transitions at twice the Fermi level. The green dashed line indicates twice the Fermi level, the black line is a fit using a phenomenological function to find the center frequency of the onset structure.

is a honeycomb carbon ($6\sqrt{3}\times6\sqrt{3}$) surface reconstruction, where about 30% of the carbon atoms are covalently bonded to the silicon in the SiC, so that the formation of the π-bands, characteristic for graphene, is precluded [69, 70]. When heated up to higher temperatures, more silicon is desorbed so that a second carbon layer forms, shown in Fig. 3.6c. The carbon atoms in the second layer are decoupled electronically from the buffer layer and SiC and therefore, form the first layer of graphene [70].

A different route to obtain electronically decoupled graphene on the Si-face of SiC is to grow the buffer layer and subsequently intercalate hydrogen in between the carbon layer and the SiC surface [71, 72]. The hydrogen breaks the covalent bonds between the silicon and buffer layer and therefore the buffer layer is transformed in a single decoupled graphene layer, shown in Fig. 3.6b. Hereafter we will refer to this type of epitaxial monolayer graphene as 'hydrogen intercalated' graphene.

Due to the difference in synthesis the graphene on a buffer layer and the hydrogen intercalated graphene display slightly different properties. Importantly, the doping found for graphene on a buffer layer is typically electron like [73–75], while the hydrogen intercalated graphene is generally hole doped [71, 76]. Whereas the doping level of the graphene on a buffer layer strongly varies from sample to sample and can be close to the Dirac point, the Fermi energy of the hydrogen intercalated graphene is often shifted as far as 300 to 350 meV away from the neutrality point. The Fermi level can be extracted from angle resolved photo emission spectroscopy (ARPES) experiments, which visualizes the occupied bands. Figure 3.7a shows results of ARPES measurements on a hydrogen intercalated monolayer. The ARPES results reveal that ϵ_F is located below the Dirac point in the hole bands. The difference in energy between Fermi level and Dirac point can be found by extrapolating the bands; for this sample $\epsilon_F \approx$ -0.27$\pm$0.1 eV. The large errorbar stems from the uncertainty in the extrapolation.

The doping of the sample can also be estimated using an optical technique: mid infrared spectroscopy reveals the onset of interband transitions at $\hbar\omega = 2|\epsilon_F|$, as is explained in section 3.2.3. Figure 3.7b shows the experimentally obtain absorption (1-T) of one of the samples used in our experiments. A clear edge, resulting from the finite doping level can be observed. From a phenomenological fit, the black curve in Fig. 3.7b, the value of the Fermi level is found: $|\epsilon_F|$ = 0.34 eV, which corresponds to a carrier concentration $n \approx 8 \times 10^{12}$ cm^{-2} (eqn. (3.10)). Where we used an estimated Fermi velocity of 10^6 m/s. For the work reported in this thesis hydrogen intercalated graphene was used. The samples were provided by the group of T. Seyller from he university of Erlangen, Germany.

For the synthesis of graphene layers on the silicon side of SiC, commercial 6H-SiC wafers are hydrogen etched, so that the SiC surface consists of smooth terraces, only showing atomic steps. For the etching, the wafers are heated to 1150°C in an atmosphere argon at a pressure of 1 bar and a flow of 0.5 litre/min. Then, the atmosphere is changed to hydrogen and the wafer is heated further to 1450°C for 15 minutes using the same pressure and flow, after which the wafers are cooled down in an argon atmosphere. At this stage the wafers are ready for graphitization, or ready to be used as a reference substrate.

The next step to synthesize hydrogen intercalated single layer graphene, is the graphitization of the silicon side of the SiC at 1450°C in an argon atmosphere at a pressure of 1 bar, with a gas flow of 0.1 litre/min, for 15 minutes. At this temperature the buffer layer is formed on top of the SiC. Then, the silicon dangling bonds are passivated by hydrogen intercalation, which is done at 600°C for 75 minutes in an atmosphere of 900 mbar and a flow of 0.9 litre/min purified hydrogen. The layer thickness of the graphene is estimated by X-ray photoemission spectroscopy (XPS). Also the carbon side of the samples is checked by XPS to be graphene free.

To produce graphene on buffer layer grown on SiC the hydrogen etched wafers are annealed for 15 minutes at 1650°C in an argon atmosphere at 1 bar using a flow of 0.1 litre/min. The higher temperature, with respect to the growth temperature of the buffer layer, is needed for the growth of the second carbon layer.

3.4.2 Multilayer graphene on SiC(000$\bar{1}$)

When started from the carbon terminated surface, the desorption of silicon from the SiC is fast and happens at moderate temperatures. During this process many graphene layers, easily up to 100 layers, can be obtained [3,136]. Although this type of graphene has many layers, magneto-optical spectroscopy revealed a Landau Level spectrum typical for single layer graphene [53], which was later confirmed by scanning tunneling microscopy (STM) measurements [57, 82]. In addition, a Berry's phase of π and weak antilocalization was observed in transport measurements [83, 84]. Finally, ARPES showed that the bandstructure of the individual layers is indeed cone-like and therefore resembles the electronic structure of a stack of uncoupled single layers [85].

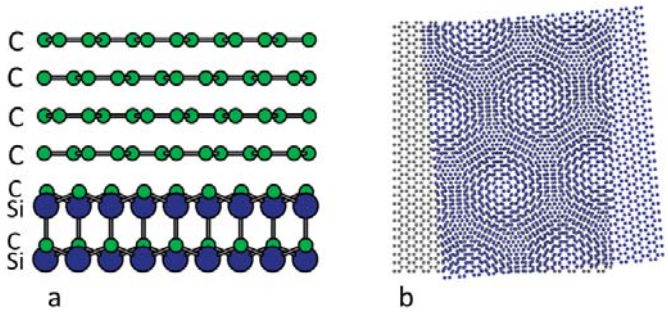

Figure 3.8: (a) A schematic picture of multilayer graphene on the carbon side of SiC (b) Moire pattern of two rotated honeycomb lattices. Courtesy, website NIST.

The electronic decoupling of the layers is generally assigned to the rotational stacking of the layers [86]. Many theoretical studies contribute to the understanding of the influence of stacking on the electronic structure and Landau levels [4, 87–93]. Importantly, it was predicted that layer twisting affects the interlayer interaction, and effectively reduces the Fermi velocity with respect to its 'bare' value in monolayer graphene [88, 90, 91]. Since the rotation between the layers varies randomly from layer to layer, the Fermi velocity is expected to be different for carriers in different graphene layers. Nevertheless, no complete theory able to quantitatively describe the effects of twisted stacking on the band structure at arbitrary rotation angles exists even for bilayer graphene.

An additional complication typical for multilayer graphene is that the substrate induces a strong shift in the Dirac-point energy E_D with respect to the chemical potential in the layers close to the SiC. The shift is strongest in the layer closest to the SiC and decreases for every subsequent layer. Therefore, different charge densities and carrier mobilities are found in the layers depending on their distance from the substrate.

The growth conditions of epitaxial graphene were constantly improving in the last years, which resulted in an enhanced mobility of charge carriers [3, 71, 72, 75, 83, 137]. Generally, the synthesis process of multilayer graphene starts with hydrogen etching the carbon terminated side of 6H-SiC, similar to the etching treatment for the synthesis of single layer graphene on the Si-face. However, the carbon terminated surface of the commercial SiC wafers is less flat than the silicon terminated surface, therefore the hydrogen etching is performed at a temperature of 1600°C, for 20 minutes. Next, the now clean and flat carbon terminated side is graphitized in an argon atmosphere, at a pressure of 100 mbar and a gas flow of 0.1 litre/min. The graphitization of the SiC takes place at around 1650°C; when kept at this temperature for 90 minutes, roughly 17 - 20 rotationally stacked layers will cover the surface.

The back side of the substrate is checked for graphene using X-ray photoemission spectroscopy (XPS), which is also used to estimate the number of graphene layers. Alternatively the number of layers can be estimated by measuring the optical absorption of the stacked layers with optical microscopy over a large area using a spot size of only

10×10 μm^2. We assume that each graphene layer absorbs 1.5% of light at 1 eV, which is the value expected for monolayer graphene on SiC, provided that the chemical potential does not exceed 0.5 eV. This absorption value is lower than the absorption of 2.3% of free-standing graphene, because the refractive index of SiC is larger than 1 (see eqn. (2.41)).

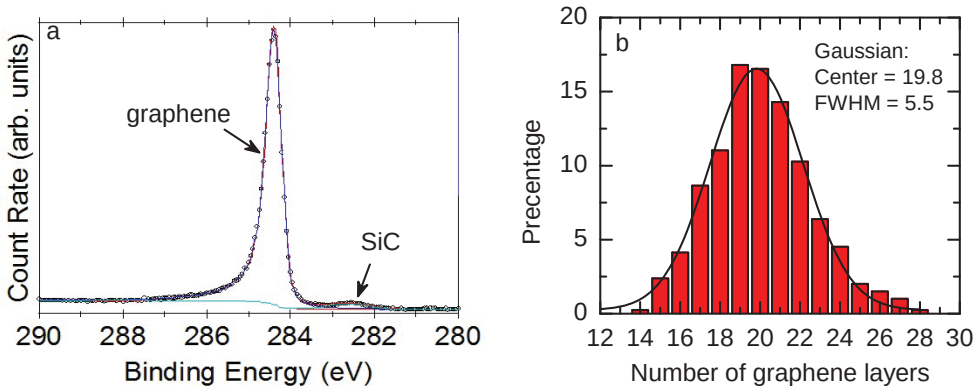

Figure 3.9: (a) XPS data on multilayer graphene on the C-side of SiC, (Felix Fromm, University of Erlangen). (b) Distribution of the MIR absorption obtained on 800 random spots on the same multilayer graphene sample. The black curve is a Gaussian fit.

Figure 3.9a shows an example of XPS data taken on a thick multilayer graphene sample. The strong peak at a binding energy of about 284.4 eV is attributed to graphene, while the weak peak at a binding energy of about 282.6 eV corresponds to SiC. From the ratio of the areas under the two peaks the number of graphene layers can be extracted. In this particular case the deduced number of graphene layers is 19 [1].

In Fig. 3.9b the distribution of layer thicknesses obtained using MIR absorption is plotted for the same sample. The distribution was obtained by measuring the absorption on 800 random spots on the sample. The line in Fig. 3.9b is a Gaussian distribution fitted to the histogram, which indicates an average coverage of 19.8 layers of graphene. The slightly larger number of layers revealed by infrared microscopy can be related to an underestimation of the absorption of one layer. In addition to the number of layers, optical absorption provides information about the width of the distribution, which is quite large of these samples.

[1] Private communications; Felix Fromm

4

Single-layer epitaxial graphene on SiC

4.1 Introduction

Up to now the thinnest structures showing the Faraday rotation were several nanometer thick two-dimensional electron gases [96]. As the rotation angle is proportional to the distance traveled by the light, an intriguing issue is the scale of this effect in single layer graphene - the ultimately thin object in condensed matter physics. In the first part of this chapter, section 4.3.1, we demonstrate that a single atomic layer of carbon turns the polarization by several degrees in modest magnetic fields. From the optical spectra, both Faraday rotation and transmission, clear signs of (magneto-) plasmonic excitations are observed, the origin of the plasmon-radiation coupling is studied by atomic force microscopy and polarized transmission measurements, presented in section 4.3.3. In the subsequent sections, the analysis of the magneto-optical properties is developed by extracting the magneto-optical conductivities from the Faraday rotation spectra and transmission spectra. The plasmon spectral weight, carrier scattering, the plasmon energy, the cyclotron resonance energy, the cyclotron mass as well as the Fermi velocity are extracted.

Apart from the giant Faraday rotation, one of the central result of this chapter is that intrinsic defects couple light to terahertz plasmons in graphene. Importantly, in section 4.4.5 we show using simulations that the Faraday rotation is strongly influenced by the plasmonic resonance. Thus, once one can actively 'program' the plasmon energy, for instance by controlling the defects, one can control the energy region of the Faraday rotation. Therefore, in the conclusions we argue that our experimental results show that epitaxial graphene is a promising candidate for future optoelectronic

The results in this chapter are published in I. Crassee *et al.* Nature Physics **7**, 48 (2011) and I. Crassee *et al.* Nano Letters **12**, 2470 (2012).

technologies.

All the experimental results present in this chapter are obtained on hydrogen intercalated single layer graphene epitaxially grown on the silicon side of SiC. The magneto-optical experiments are performed in moderate magnetic fields: up to 7 T. Measurements done at higher fields, up to 32 T, will be the topic of the next chapter.

4.2 Sample and experimental details

The graphene samples are prepared by graphitization of a SiC substrate with a thickness of about 370 μm and a surface area of 10×10 mm^2. The synthesis method of the single layer graphene is discussed in section 3.4.1. The back sides of the samples are always checked to be free of graphene using x-ray photoemission spectroscopy. The reference substrate is prepared from the same SiC wafer. ARPES measurements on similar samples, see Fig. 3.7a, show that the Fermi level in this type of graphene is shifted below the Dirac point. Using optical spectroscopy in the mid infrared range, it was found that the sample used in our study has a Fermi energy, ϵ_F = -0.34 $\pm$ 0.01 eV (see Fig. 3.7b in sec. 3.4.1), which corresponds to a hole concentration $n = \epsilon_F^2/(\pi\hbar^2 v_F^2) \approx 8\times10^{12}$ cm^{-2} [138], where $v_F \approx 10^6$ m/s is the Fermi velocity.

All magneto-optical measurements are done in the Faraday geometry (magnetic field and propagation of light normal to the sample) using a Fourier transform infrared spectrometer connected to a split-coil superconducting magnet, as described in sections 2.3.1 and 2.3.3. The infrared Fourier transform spectrometer is equipped with a mercury source and silicon beamsplitter to access the low terahertz (THz) frequencies, while for the far infrared range a globar source and 6μ mylar beamsplitter was used. With this combination of sources and beamsplitters the accessible frequency range is 1.5 meV to 85 meV. The superconducting split-coil magnet delivers fields up to 7 T. The measurements presented in this chapter are done at temperatures between 5 and 10 K.

4.3 Results

4.3.1 Giant Faraday rotation

Figure 4.1a shows the Faraday angle θ measured on single layer graphene at 5 K in magnetic fields up to 7 T in the far-infrared range. The spectra show a strong dependence on the magnetic field: the observed spectral structure becomes larger and shifts to higher energies with increasing field. Measurements on the bare substrate did not reveal any Faraday effect, hence the rotation comes exclusively from the carbon monolayer. At 7 T, the maximum Faraday rotation exceeds 0.1 radians ($\sim$ 6 degrees), which is an unexpectedly large effect for just a single atomic layer [138]. It is much larger than the fine-structure constant ($\sim 10^{-2}$), which is the predicted scale for the Faraday

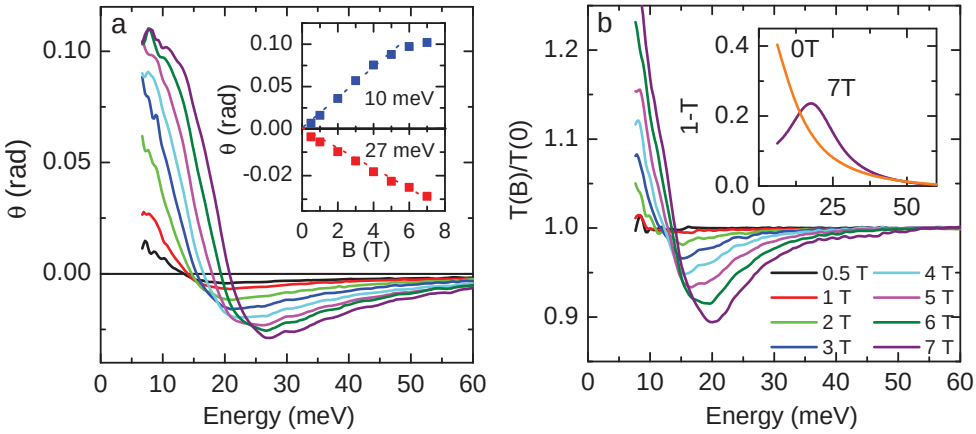

Figure 4.1: (a) The Faraday angle θ for fields up to 7 T at 5 K. The inset presents the magnetic field dependence of $\theta(B)$ at $\hbar\omega$ =10 and 27 meV. The dashed lines are linear fits of the data points between 0 and 5 T. (b) the transmission ratio $T(B)/T(0)$ at the same fields. In the inset the absorption spectra $1 - T(B)$ for B = 0 T and 7 T are shown.

angle, associated with the quantized Hall conductance [139–142]. The inset shows the field dependence of θ at 10 and 27 meV. At low fields, the rotation is linearly dependent on field; at an energy of 10 meV the angle increases with a slope of +18.5 mrad/T, while at 27 meV the angle decreases with -4.5 mrad/T.

The transmission spectra at corresponding fields also reveal a strong magnetic field dependence, most easily seen in the zero-field normalized transmission $T(B)/T(0)$, shown in Fig. 4.1b. The spectra show a dip moving to higher energies with increasing field. The inset shows the absorption (1-T) at 0 and 7 T. A strong peak is observed, shifting from energies below 10 meV, to about 22 meV at 7 T. As we will see later, this peak is associated with quasi-classical cyclotron resonance.

The doping, ϵ_F = -0.34 eV, found from mid-infrared absorption measurements, in combination with the relatively low magnetic fields used in these experiments put the cyclotron resonance in the classical regime: the Fermi energy is far from the Dirac point, so that the allowed optical transition are between LLs with large quantum numbers [58, 122]. In Fig. 4.2a the hole-like Landau levels (up to n = -30 for clarity) are plotted as a function of field, using $v_F = 10^6$ m/s. The Fermi energy, determined for the single layer graphene sample, is indicated by the red dashed line. The allowed optical transitions are shown in the close-up in Fig. 4.2b with blue arrows. Clearly for the Landau levels involved in the excitations $|n| \gg 1$. Therefore, the Dirac quasiparticles are expected to exhibit the classical cyclotron resonance effect, as discussed in section 3.3.2, with a linear dependence on the magnetic field. The strength of the oscillator is determined by the total density of carriers: the higher the doping level, the larger the cyclotron peak in the transmission spectra and the larger the Faraday rotation.

Importantly, the Faraday rotation spectra not only depend on the total density of

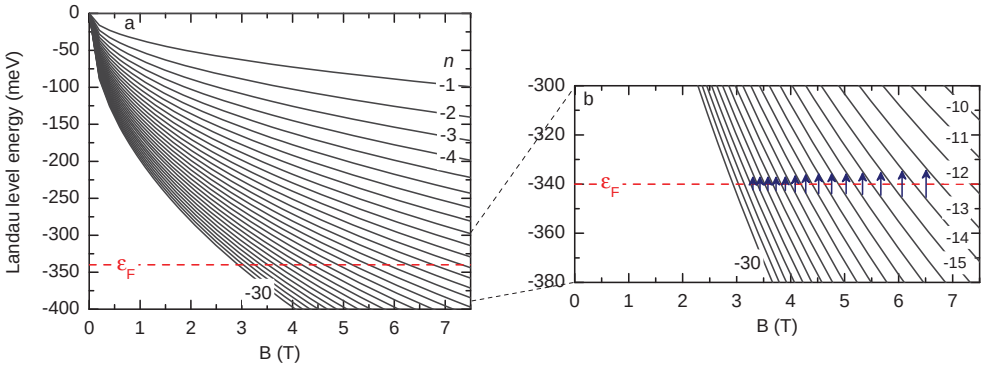

Figure 4.2: (a) Magnetic field dependence of the hole like Landau levels, with n = -1 to -30 and $v_F = 10^6$ m/s. The red dashed line corresponds to the Fermi energy in the single layer graphene sample. (b) Close-up of the Landau levels around ϵ_F, the blue arrows indicate the allowed optical transitions between the Landau levels.

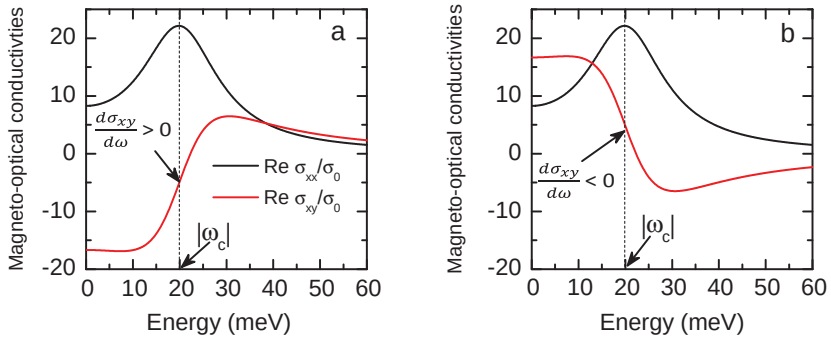

Figure 4.3: (a) The Drude Lorentz model for the diagonal (black line) and Hall conductivity (red line), with ω_c = +20 meV (electron doping). (b) The same Drude-Lorentz model for the diagonal (black line) and Hall conductivity (red line), with ω_c = -20 meV (hole doping). The curves were obtained from eqns. (2.25) and (2.26)

charge carriers but also reveal the sign of those charge carriers in the graphene layer. The spectral feature corresponds to an antisymmetric structure, where the absolute cyclotron resonance energy, $|\omega_c|$, coincides with the position of the maximum absolute slope $|d\theta(\omega)/d\omega|$, or the inflection point. The sign of the slope at the inflection point matches the sign of ω_c. Figure 4.3a shows the real parts of $\sigma_{xy}(\omega)$ (red line) and $\sigma_{xx}(\omega)$ (black line) for ω_c = +20 meV obtained using the Drude-Lorentz model for the magneto-optical conductivity (eqn. (2.25) and eqn. (2.26)). The peak in $\sigma_{xx}(\omega)$ is centered around $|\omega_c|$, which coincides with the inflection point in $\sigma_{xy}(\omega)$. At the inflection point $d\sigma_{xy}(\omega)/d\omega > 0$, signaling n-type doping. Since Re $\sigma_{xy}(\omega) \propto \theta(\omega)$, the sign of $d\sigma_{xy}(\omega)/d\omega$ matches the sign of $d\theta(\omega)/d\omega$. In Fig. 4.3b the same model is plotted, however now ω_c = -20 meV: hole-type doping. $\sigma_{xx}(\omega)$, the black line in both (a) and (b), is entirely unchanged. However, the sign of the slope at the inflection point in $\sigma_{xy}(\omega)$ (red line) is opposite: $d\sigma_{xy}(\omega)/d\omega < 0$. Clearly, $\sigma_{xy}(\omega)$ and thus $\theta(\omega)$,

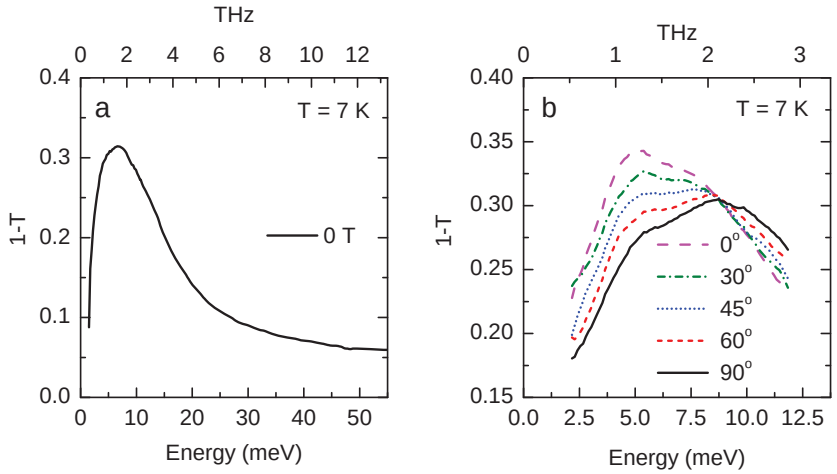

Figure 4.4: (a) Terahertz absorption spectrum of graphene on SiC at T = 7 K measured using unpolarized light. (b) terahertz absorption spectra at T = 7 K measured using linearly polarized light. The polarization state of the impinging light was rotated with respect to the sample.

unmistakeably reveal the sign of the carriers. Coming back at Fig. 4.1a: the negative slope at the inflection point in the Faraday rotation spectra is an unmistakable signature of hole doping in hydrogen intercalated single layer graphene.

The unexpectedly large rotation observed is directly related to the high doping typical for single layer epitaxial graphene and opens up new pathways for future graphene-based technologies. In addition to the practical side of this newly identified property, the Faraday rotation spectra offer optical, thus no need for electrical contacts, access to fundamental properties of graphene, such as the sign of the charge carriers.

4.3.2 Optical response in the terahertz: plasmons in graphene

After the observation of the giant Faraday rotation in single layer graphene [138], we extended the spectral range of our measurements of the Faraday angle and transmission spectra down to terahertz (THz) frequencies in order to do more quantitative analysis on the data. The goal of these measurements was to better determine the shape of the Drude peak, however, by doing these measurements we were in for a large surprise.

The low frequency absorption at zero magnetic field, shown as the orange curve in the inset of Fig. 4.1b resembles strongly a Drude response, a peak centered around zero energy, which is the optical signature of free carriers. However, the complementary experiments in the THz regime show that the Drude absorption is absent. Instead a strong peak at around 1.6 THz (6.5 meV) is observed. Figure 4.4a shows the substrate normalized absorption (1-T) measured at 7 K at zero field with unpolarized light [143]. The deviation from the Drude behavior is associated with the presence of a confinement potential acting on the free carriers and the corresponding plasmonic absorption.

A similar resonance was observed in graphene micro-ribbons in the polarization perpendicular to the ribbons [20] and in graphene dots [144]. The micro-ribbons and dot-like structures break the translational symmetry in the graphene, which results in a shift of the Drude peak to higher frequencies.

Figure 4.4b shows the absorption measured at 7 K at zero field using linearly polarized light [143]. The polarization state of the light was rotated with respect to the graphene sample. The peak position in the spectra appears at different energies for different rotation of the polarization state. Therefore the polarized optical absorption shows that the THz resonance peak is related to the sample morphology. Importantly, the peak position remains at finite energy for every polarization.

4.3.3 Origin of the plasmonic resonance

To couple electromagnetic radiation to a plasmon mode, the translational invariance of the system needs to be violated. In two-dimensional systems, typical ways to break the symmetry are placing an external grid in the vicinity of the sample [145] and making stripe or dot-like periodic structures inside the system [24, 146–148]. In graphene, this coupling has recently been achieved by pattering it in the shape of ribbons [20], in a periodic array of dots [144] and by using a metallic atomic force microscopy (AFM) tip in scattering-type scanning near field optical microscopy [22].

Importantly, the samples used in this study were not patterned or otherwise shaped to break translation symmetry. In order to clarify the origin of the confinement that causes the plasmonic resonance, we performed vibrating cantilever atomic force microscopy (AFM) imaging to extract topographic and phase information of the graphene on SiC. Figure 4.5a shows a topographical height image of a 10×10 μm^2 area of the sample. The dominating structures are the terraces due to the miscut angle of SiC substrate [75, 149, 150]. Due to these terraces the translation symmetry in the graphene is broken and therefore plasmons can be excited. Their irregular shape as compared to morphologies observed earlier [75] is related to the specific graphitization temperature. Measurements on different spots of the sample show that the terraces are oriented in the same direction across the entire sample.

Closer inspection of the AFM images also reveals numerous wrinkles in graphene, such as the ones indicated by the arrows in Fig. 4.5b. The wrinkles are formed due to the relaxation of strain in graphene during the cooling down after graphitization [151, 152], and are most probably an additional cause of the broken translational symmetry in the graphene. Figure 4.5c presents the map of the oscillation phase of the cantilever on the same area as in Fig. 4.5b. The phase delivers information about specific material properties which affect the interaction between tip and sample. Sharp changes in the height profile, due to the steps and the wrinkles are clearly observed. The dark spots in the phase correspond to regions without graphene, as was determined by Raman spectroscopy.

Figure 4.6 shows height profiles for the lines marked in Fig. 4.5a. Profiles 1 to 3 correspond to the steps in the SiC substrate, while traces 4 to 7 are taken across

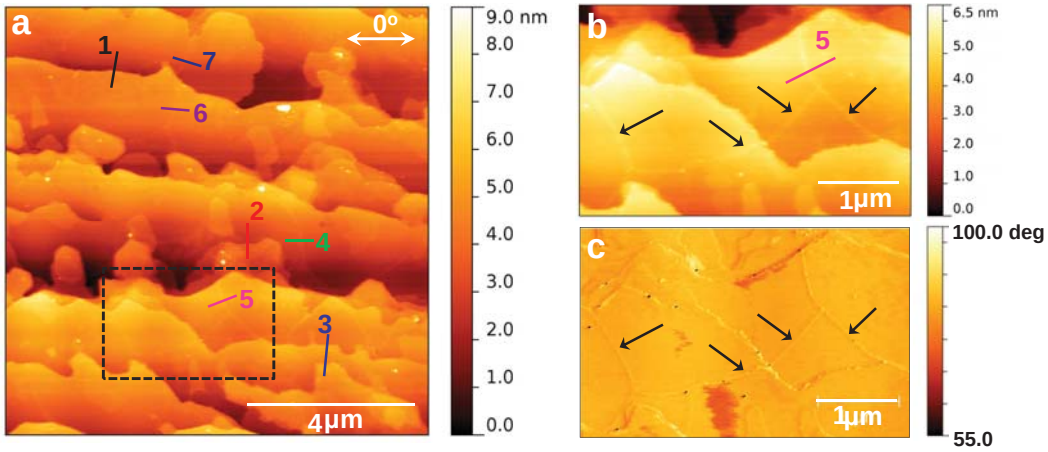

Figure 4.5: Topographic height (a) of a 10×10 μm^2 region of epitaxial graphene on SiC used for optical experiments. (b) and (c): Close-ups of the region in (a) marked by dashed rectangles, where (b) is the height map, while (c) is the corresponding phase. Arrows point to graphene wrinkles.

the wrinkles on the terraces and show that these wrinkles have a height of less than 1 nm, which is in agreement with previous work [151]. The regions of homogeneous graphene have a typical size of about one micrometer throughout the whole sample.

The results of the polarized optical transmission experiment already revealed a strong anisotropy in the plasmon resonance energy, which correlates with the angle of the linear polarization state with respect to the sample. The spectrum corresponding to 0° in Fig. 4.4b is the transmission obtained with the polarization axis parallel to the substrate terraces, as indicated in Fig. 4.5a, while the 90° spectrum in Fig. 4.4b corresponds to transmission obtained with the polarization axis perpendicular to the substrate terraces. Thus, the absorption maximum is at about 1.7 times higher energy for the electric field perpendicular to the terraces than for the parallel orientation. The excitation of the plasmon parallel to the terraces is likely due to the rough shape of the SiC step edges. But it cannot be excluded that the wrinkles, which are randomly oriented, are an additional cause of translational symmetry breaking in the graphene. Indeed, near-field optical measurements show that wrinkles scatter plasmons as effectively as the steps in the substrate [3].

From the AFM imaging we conclude that the broken translational invariance in graphene epitaxially grown on SiC is a result of intrinsic defects uniformly distributed over the layer, caused by substrate terraces and thermal relaxation after the graphitization process [75, 76, 151, 152]. The correlation between the polarized optical absorption curves and the orientation of the terraces in the substrate shows that the terahertz plasmon resonance peak is related to those morphological structures.

[3] Private communications: J. Chen *et al.* unpublished.

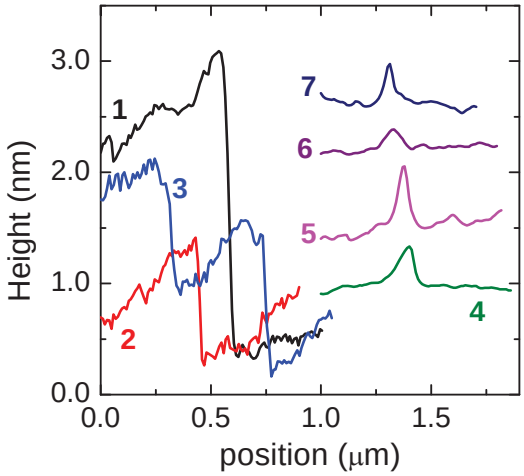

Figure 4.6: Height profiles along selected lines marked in Fig. 4.5, corresponding to terraces (1-3) and wrinkles (4-7).

4.3.4 Terahertz magneto-optical response: magnetoplasmons in graphene

Figures 4.7a and b show the Faraday rotation and transmission spectra measured at 5 K in fields up to 7 T [143] using unpolarized light. Because of the anisotropy of the sample, the curves and the plasmon energy in Fig. 4.7 are effective averages over all polarizations. The absolute Faraday rotation observed in these measurements is somewhat lower compared to the Faraday rotation observed in Fig. 4.1a, which is probably due to an increased surface contamination. The Faraday rotation spectra in Fig. 4.7a show a decrease in rotation angle at energies towards zero, which was not observed previously in Fig. 4.1a. The THz transmission spectra in Fig. 4.7b show that the dip observed at zero field splits in to two modes, one of which moves towards lower energy and the other moves towards higher energy with increasing field. This strong dependence on the magnetic field stands in drastic contrast to conventional plasmonic materials like gold, where the carrier mass exceeds the free-electron mass, leading to at best a weak dependence on magnetic field [153].

With the use of the thin film relations for the diagonal conductivity (section 2.3.1) and the optical Hall conductivity (section 2.3.3), the real parts of the magneto-optical conductivity spectra are extracted from the transmission and the Faraday rotation spectra, respectively. The optical Hall conductivity $\sigma_{xy}(\omega)$, normalized to the universal conductivity $\sigma_0 = e^2/4\hbar$ is shown in Fig. 4.7c. The normalized diagonal conductivity $\sigma_{xx}(\omega)$, is plotted in Fig. 4.7d. Clearly, the plasmon resonance centered at about 6.5 meV at 0 T splits into two modes, with one increasing and the other decreasing with B. The black dashed lines in Fig. 4.7c and Fig. 4.7d are fits to the conductivity curves using an effective medium model, as discussed in section 4.3.5.

In order to get further insight into the character of the two modes we extracted

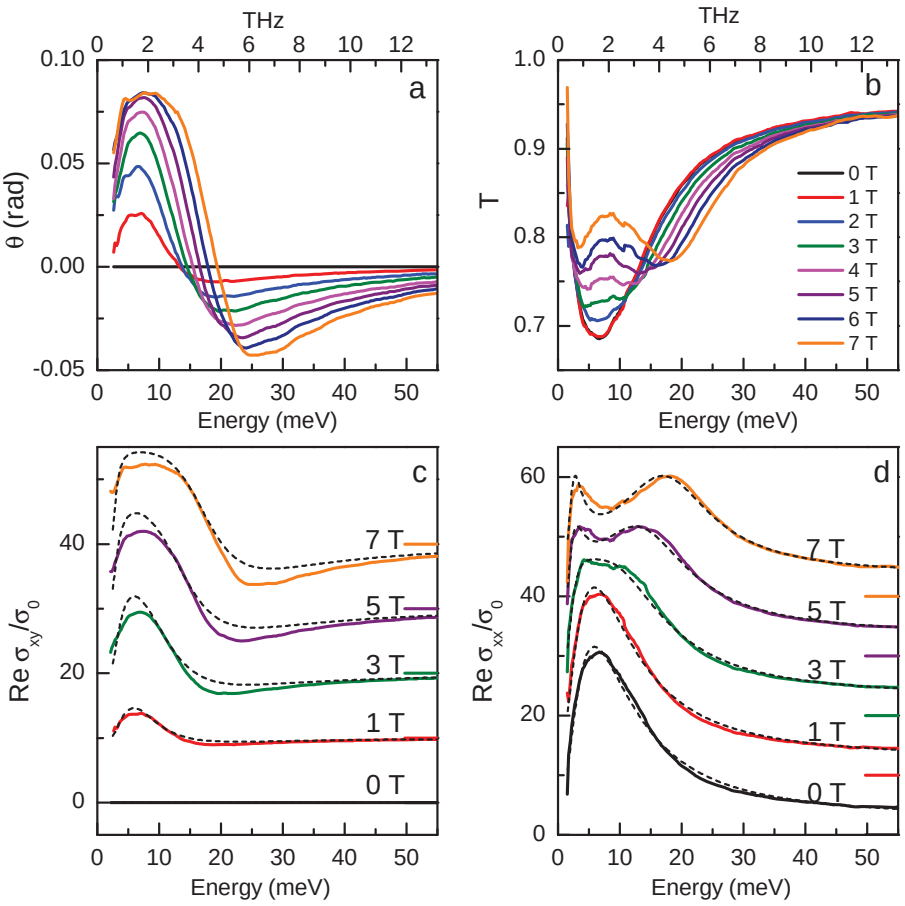

Figure 4.7: (a) The Faraday rotation spectra, extended to THz energies, for fields up to 7 T and (b) substrate normalized terahertz transmission spectra of graphene on SiC. The diagonal (c) and Hall (d) conductivities normalized to $\sigma_0 = e^2/4\hbar$. The offset of the curves in (c) and (d) are indicated by lines of the same color. The dashed lines in (c) and (d) are fits to the data.

the imaginary part of the Hall conductivity $\mathrm{Im}\,\sigma_{xy}(\omega)$ from the real part of the Hall conductivity $\mathrm{Re}\,\sigma_{xy}(\omega)$ with the use of the Kramers-Kronig relations (section 2.2.4). Next, the real parts of the optical conductivity for left and right handed circularly polarized light, $\sigma_\pm(\omega) = \sigma_{xx} \pm i\sigma_{xy}$ are obtained directly from $\mathrm{Re}\,\sigma_{xx}(\omega)$ and $\mathrm{Im}\,\sigma_{xy}(\omega)$. $\sigma_-(\omega)$ and $\sigma_+(\omega)$ are plotted in Fig. 4.8a and b respectively. One can clearly see that in each of the two circular polarizations only one mode is present. The peak positions in $\sigma_-(\omega)$ and $\sigma_+(\omega)$ are denoted ω_+ and ω_- respectively, since the first increases and the latter decreases with B. Figure 4.8c shows the field dependence of ω_+ and ω_-.

The field-induced splitting of the plasmon peak resembles strikingly the appearance of collective resonances observed previously in disk-shaped quantum dots of two-dimensional electron gases based on GaAs heterostructures [146, 148]. To illustrate the comparison; Fig. 4.8d shows the energies of the two modes reported in

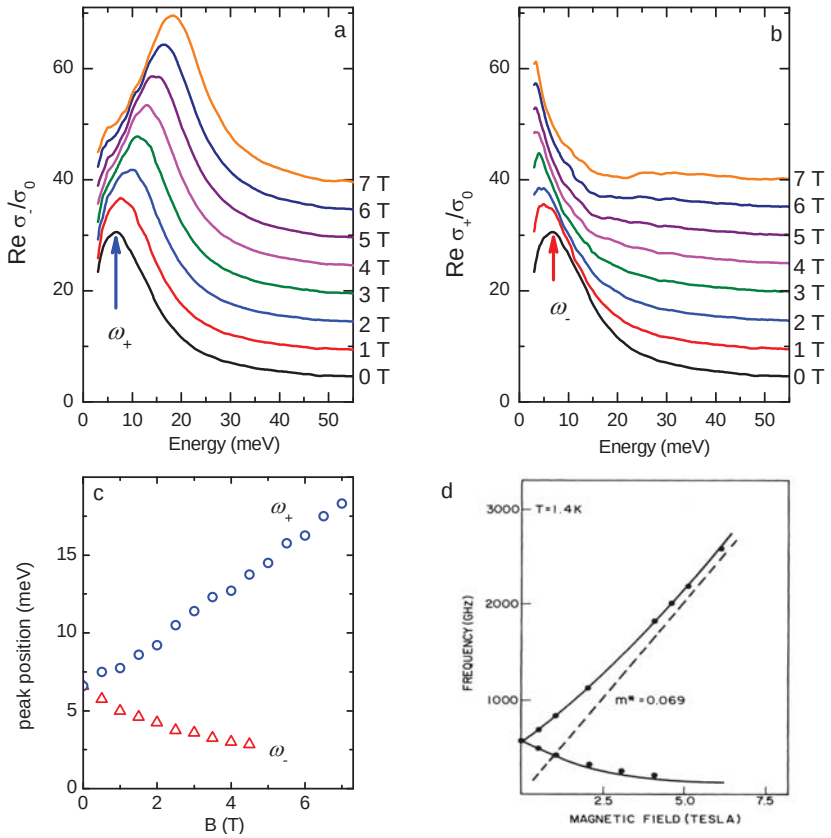

Figure 4.8: (a) $\mathrm{Re}\,\sigma_-(\omega)$ and (b) $\mathrm{Re}\,\sigma_+(\omega)$ obtained using a Kramer-Kronig transformation to extract $\mathrm{Im}\,\sigma_{xy}(\omega)$. (c) peak positions in $\mathrm{Re}\,\sigma_-(\omega)$ and $\mathrm{Re}\,\sigma_+(\omega)$ as a function of field. (d) magnetoplasmon energies observed in a heterostructure of a 2DEG by Allen [146]

Ref. [146], even the energy scale of the plasmon resonance is comparable to the excitation observed in Figs. 4.8a, b and c. The surface of liquid helium is another example of a system on which bound 2D electrons show plasmon and magneto-plasmonic resonances [154, 155]. For both the electron gas in the GaAs heterostructures and the surface of liquid helium, the upper and lower branches were attributed to the so-called bulk and edge magnetoplasmons, respectively, with resonance frequencies [146]:

$$\omega_\pm = \sqrt{\frac{\omega_c^2}{4} + \omega_0^2} \pm \frac{|\omega_c|}{2}, \tag{4.1}$$

where ω_0 is the plasmon frequency at zero field, $\omega_c = \pm eB/m$ is the cyclotron frequency (positive for electrons and negative for holes) and m is the cyclotron mass. At high fields, where $|\omega_c| \gg \omega_0$, the upper branch becomes essentially the usual cyclotron resonance with a linear dependence on magnetic field, while the lower branch represents a collective mode confined to the edges [156] with the energy inversely proportional to the field.

4.3.5 Effective medium approach

In the specific case of an array of disk shaped quantum dots, the effective medium Maxwell-Garnett approach [146] can be used to derive the magneto-optical response of such a system. Details of the Maxwell-Garnett approach can be found in appendix B.4. For a filling factor f of one, the effective medium model describing (magneto)plasmonic resonance simply reduces to the phenomenological Drude-Lorentz model for magneto-optical conductivity, where the plasmon resonance energy at zero field is ω_0.

The spectra of $\sigma_{xx}(\omega)$ and $\sigma_{xy}(\omega)$ at each magnetic field were simultaneously fitted using eqns. (2.27) and (2.28) (see section 2.2.2). The dashed black lines in Fig. 4.7c and d show the fitted Drude-Lorentz model containing one resonance peak ($n = 1$ in eqn. (2.27) and eqn. (2.28)):

$$\sigma_{xx}(\omega) = \frac{2D}{\pi} \frac{\gamma - i\omega + \frac{\omega_0^2}{\omega}}{\omega_c^2 - (\omega + i\gamma + \frac{\omega_0^2}{\omega})^2}, \tag{4.2}$$

$$\sigma_{xy}(\omega) = \frac{2D}{\pi} \frac{-\omega_c}{\omega_c^2 - (\omega + i\gamma + \frac{\omega_0^2}{\omega})^2}. \tag{4.3}$$

The parameters ω_0, ω_c, γ and D were treated as adjustable during fitting. We also added a small frequency independent background term $\sigma_b \approx 3.5\ \sigma_0$ to the real part of the diagonal optical conductivity. The background is discussed in section 4.4.3.

The experimental data including all important spectral features are well reproduced, which shows that the plasmon structure and the splitting of the mode in magnetic field can be quantitatively described by the phenomenological Drude-Lorentz formula [146, 157]. The good comparison between model and data might come as a surprise, for several good reasons. First of all, the effective medium approach leading to the Drude Lorentz formula is strictly valid for electronically isolated disk like quantum dots. In addition, the epitaxial graphene is anisotropic and the size of the homogeneous regions of graphene is certainly distributed. Moreover, the plasmon confining edges originating from the defects in epitaxial graphene seem rough and complex. Despite its seemingly inapplicability, the phenomenological Drude-Lorentz model can quantitatively reproduce the optical spectra. Note, quantitatively: noticeable deviations, especially in the fits to $\sigma_{xy}(\omega)$, demonstrate the inevitable limitations of this simple model.

In order to scrutinize the applicability of the Drude-Lorentz model to describe the magnetoplasmon resonance in systems other than regular arrays of disk-shaped dots with finite thickness, we fitted the phenomenological model to numerical spectra reproduced from Ref. [158] for magnetoplasmonic resonance in a lattice of square graphene patches. The numerical results for the optical Hall conductivity for two different patterns with length L are shown in Fig. 4.9a with open symbols, for both results T=5 K, B = 7 T, $v_F = 10^6$ m/s, γ = 10 meV and ϵ_F = 0.34 eV. The black lines in Fig. 4.9a are fits to the spectra using the Drude-Lorentz relation for $\sigma_{xy}(\omega)$ (eqn. (2.28)), where n = 1

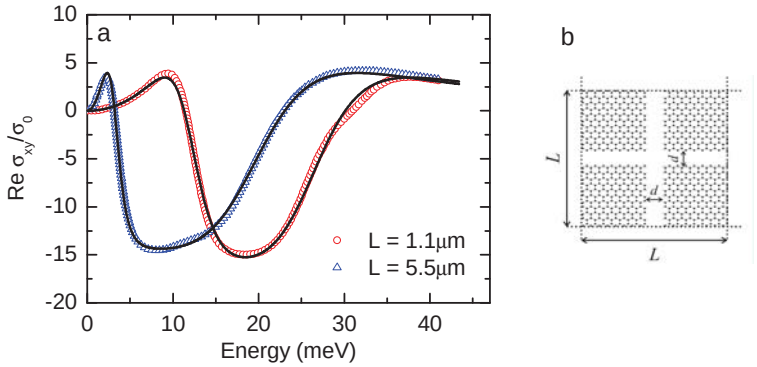

Figure 4.9: (a) Numerical spectra of Re $\sigma_{xy}(\omega)$ showing magnetoplasmonic resonance in a array of square graphene patches, reproduced from Ref. [158] (open symbols), fitted with the Drude-Lorentz model in magnetic field (black lines). (b) schematic representation of the modeled graphene sample.

(one oscillator) and ω_0, ω_c, γ and D were treated as adjustable parameters. Apart from the weak second order resonance seen in the curve for L = 1.1 μm at around 30 meV, the numerical spectra are well reproduced. This demonstrates that the applicability of eqn. (2.27) and eqn. (2.28) is not restricted to the case of an array of disk-shaped dots with finite thickness.

Supported by the ability of the Drude-Lorentz model to quantitatively describe magnetoplasmonic resonance in graphene, we use the fit results to extract the plasmon spectral weight D, the plasmon energy ω_0, the cyclotron resonance energy ω_c and the scattering rate γ at every magnetic field.

4.4 Discussion

4.4.1 Cyclotron resonance energy

Figure 4.10 shows the field dependence of ω_0 and ω_c extracted from the fitting procedure. The bare plasmon frequency is essentially constant, with an average value of about 6.5 meV. The cyclotron frequency is almost perfectly linearly dependent on the field, with a slope $\hbar|\omega_c|/B$ = 2.1 meV/T. According to the relation, $|\omega_c| = |eB|/m$, the cyclotron mass is about 5.5 % of the free electron mass m_e. Also shown in Fig. 4.10, are the energies of the two magnetoplasmon modes, $\omega_\pm$, which are calculate with the results for ω_0 and ω_c and the relation for the magnetoplasmon energies, eqn. 4.1. They are very close to the peak positions in $\sigma_\pm$ (Fig. 4.8a,b,c).

The linear dependence of the cyclotron resonance energy perfectly agrees with the classical cyclotron resonance expected from Dirac-like charge carriers in graphene at high doping [30]. The cyclotron mass depends on doping according to the relation $m = |\epsilon_F|/v_F^2$. Using $|\epsilon_F| = 0.34$ eV, and $m = 0.055m_e$, the Fermi velocity of the charge carriers can be obtained: $v_F = 1.04 \times 10^6$ m/s. This number matches remarkably well

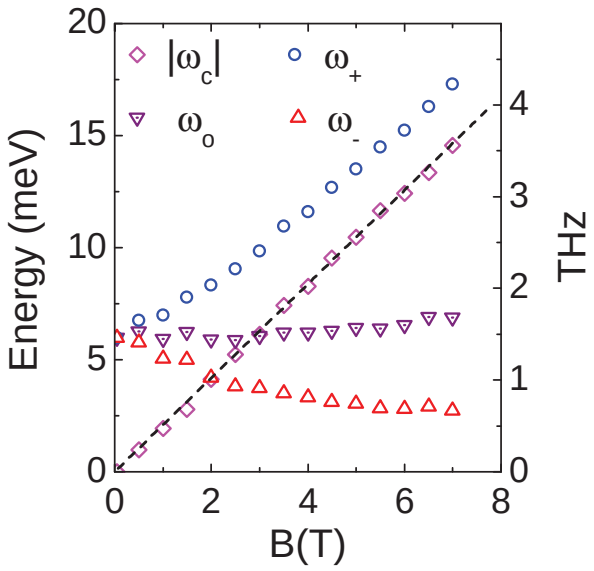

Figure 4.10: The magnetic field dependence of the plasmon energy $\hbar\omega_0$, cyclotron resonance energy $\hbar|\omega_c|$ and magnetoplasmon energies $\hbar\omega_\pm$. The dotted line is a linear fit to the cyclotron energy.

the Fermi velocity obtained by other methods [159].

4.4.2 Plasmon and magnetoplasmon resonance energies

The plasmon energy, $\hbar\omega_0 = 6.5$ meV, contains important information about the confinement causing the plasmon excitation. In the particular case of isolated quantum dots, the plasmon resonance energy is predicted by the effective medium approach [146, 157, 160]:

$$\omega_0^2 = \frac{3\pi^2 n e^2}{2md\kappa}, \tag{4.4}$$

where $\kappa = (1 + \epsilon_{SiC})/2 \approx 5$ is the average dielectric constant of the surrounding media and d is the dot diameter. For graphene, where the effective mass $m = |\epsilon_F|/v_F^2$ and the charge density $n = \epsilon_F^2/\pi v_F^2$, eqn. (14) can be rewritten:

$$\omega_0^2 = \frac{3\pi e^2 |\epsilon_F|}{2d\kappa}, \tag{4.5}$$

From which can be seen that the plasmon energy is square-root dependent on the Fermi energy of the graphene layer.

From the topographic height maps measured by AFM, we found that the mean size of the homogeneous graphene regions is about 1 μm. If we naively use eqn. (4.5) and use $|\epsilon_F| = 0.34$ eV, the predicted plasmon energy is 15.2 meV. This is more than twice the experimentally observed value. The discrepancy between the experimentally observed plasmon energy and the predicted energy is certainly not surprising.

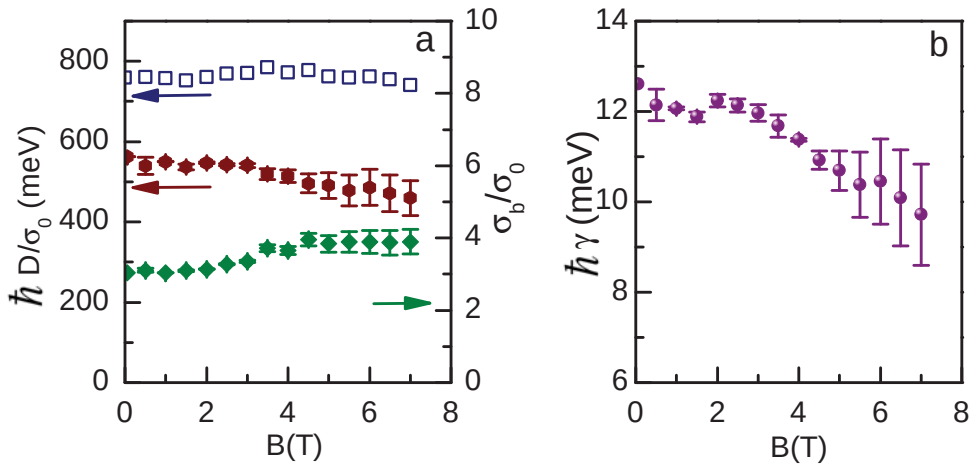

Figure 4.11: (a) Magnetic field dependence of the plasmon spectral weight D (hexagons), and the background term σ_b (diamonds). The open squares correspond to the experimental optical conductivity D_{int}, obtained from integration of the spectra. (b) Field dependence of the broadening γ (circles) of the plasmon resonance.

Clearly, the graphene regions are not shaped in dots, but have a complex and rough shape. Moreover, the defect lines separating the homogeneous regions are very narrow, which means that the regions cannot be seen as 'isolated'. Due to the narrow separation, electromagnetic coupling between neighboring graphene regions is likely to play an important role in the confinement of the carriers. Such a coupling causes a redshift [157, 161–163] of the plasmon energy as compared to the case of uncoupled particles, this redshift of the plasmon energy is commonly observed in plasmonic nanostructures.

The two magnetoplasmon branches ($\omega_\pm$), found from ω_0 and ω_c correspond to the collective behavior of the charge carriers in the graphene [156]. The upper branch, of which the energy increases with magnetic field is approaching the cyclotron resonance energy and corresponds to carriers performing cyclotron motion confined to the homogeneous graphene regions. As was seen in Fig. 4.8a, the ω_+ mode is visible as a peak in Re $\sigma_-(\omega)$. The resonances showing up in Re $\sigma_-(\omega)$ are due to hole-like charge carriers, which is in agreement with the fact that the graphene is p-doped.

However, although the graphene is hole doped, the lower magnetoplasmon mode, ω_-, of which the resonance energy depends on $1/B$, is only present in Re $\sigma_+(\omega)$, signaling electron-like behavior, as can be seen in Fig. 4.8b. The seemingly electron-like behavior of the mode originates from the collective resonance of hole-like carriers which are effectively confined to the edges of the regions [164].

4.4.3 Spectral weight

Figure 4.11a shows the spectral weight D of the plasmon resonance peak and the amplitude of the background conductivity as a function of magnetic field, obtained by fitting the effective medium model to $\mathrm{Re}\,\sigma_{xx}$ and $\mathrm{Re}\,\sigma_{xy}$. The spectral weight of the plasmon peak shows a small decrease with magnetic field. Likely, the slight field dependence D is not associated with a true decrease of the intraband spectral weight. A second method to extract the plasmon spectral weight is to do straight forward integration of the plasmon peak in the optical spectra. The open squares in Fig. 4.11a correspond to the integrated optical conductivity, from 2 to 85 meV, $D_{int} = \int \mathrm{Re}\sigma_{xx}(\omega)d\omega$. Indeed D_{int} is roughly constant with field. The decrease in D extracted from the fitting is likely related to the slight increase of the background conductivity with field. The increase in the background effectively compensates the decrease of D. Another reason for the slight decrease in D could be the use of the thin-film relation to extract the optical conductivity from the transmission. As is shown in appendix B.1., for increasing magnetic field the use of relation eqn. (2.47) results in an underestimation of the conductivity and thus of the spectral weight. The effective underestimation of the spectral weight can be as large as 7% for a peak with an original spectral weight of 0.6 eV.

The value of $\hbar D/\sigma_0$ extracted from the fitting is about 0.52 eV. This is somewhat smaller than the expected value of $2|\epsilon_F|$ = 0.68 eV. The difference can only be partially explained by the fact that the thin film relation underestimates the spectral weight. An incomplete coverage of the SiC substrate by graphene could be related as well (see Fig. 4.5b), however the discrepancy can also be due to the presence of the background term σ_b.

The observation of the background is quite unexpected. Although it may partially be due to an experimental uncertainty in the transmission normalization procedure, it cannot be excluded that σ_b is related to the low spectral weight of the plasmon resonance. Possibly, the spectral weight is renormalized by electron-electron [46], electron-phonon interactions [165, 166] or excitations of higher harmonic plasmon resonances [157, 160, 163]. Therefore the spectral weight of the plasmon resonance could be effectively transferred to other energies, forming a background. A second possibility is that the negative charge removed from the graphene monolayer forms a conductive layer in SiC. The electron gas at the substrate-graphene interface could cause a strongly damped Drude peak, manifesting itself as a background in the far infrared range. Notably, a certain optical background below the onset of interband absorption was present in exfoliated monolayer graphene on Si/SiO_2 [42].

4.4.4 Scattering rate

Similar to the dependency of the plasmon spectral weight, the scattering rate, plotted in Fig. 4.11b, is decreasing at high magnetic fields. The broadening, $\hbar\gamma$, is about 10 to 12 meV, surprisingly, this is more than two times smaller than observed by another

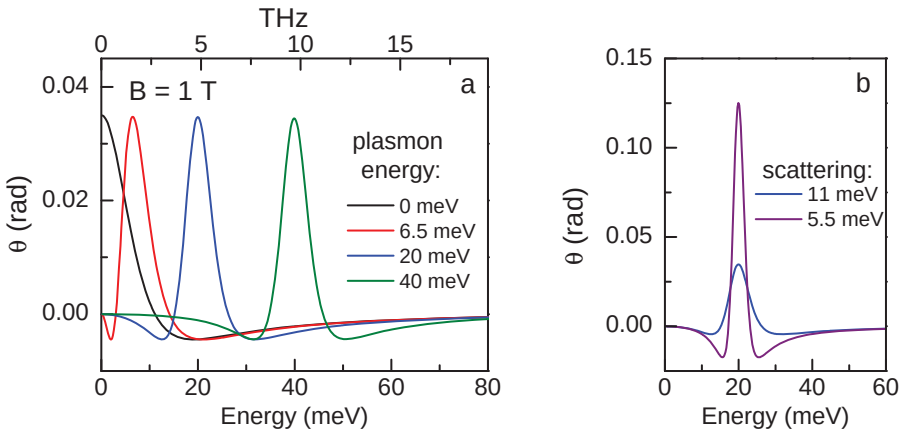

Figure 4.12: A simulation of the effect of the plasmon energy and the scattering on the Faraday rotation. (a) Faraday rotation for $\hbar\gamma$ = 11 meV for different values of $\hbar\omega_0$ = 0, 6.5, 20, and 40 meV. (b) Faraday rotation for $\hbar\omega_0$ = 20 meV and different values of $\hbar\gamma$ = 11 and 5.5 meV. Both in (a) and (b) the magnetic field is 1 T.

group [100] on epitaxial graphene on SiC.

The true intrinsic electron scattering is likely to be even smaller than 10 meV, since the spectral feature is additionally broadened by the distribution of sizes and shapes of the homogeneous regions. However, thanks to the square-root dependence of the plasmon energy on the size of the homogeneous regions, $\omega_0 \propto \sqrt{1/d}$, the effect of the distribution in the size of the homogeneous regions is relatively weak, so that still a reasonably sharp resonance is observed.

The origin of the decrease in scattering rate with increasing magnetic field is also most likely related to the variation in the size of the homogeneous graphene regions. At high magnetic fields the energy of the peak is less influenced by the (broadened) plasmon energy but more and more by the well defined cyclotron resonance energy, therefore the effect of statistical distribution is weaker at high fields.

4.4.5 Influence of magnetoplasmons on the Faraday rotation

The large Faraday effect, relatively low absorption and magnetoplasmons make graphene a promising material for novel applications in optoelectronics. One could think of exploiting the Faraday effect and magnetoplasmonic resonance to construct optical rotations, isolators and waveguides.

Simulations using the Drude Lorentz model for the magneto-optical conductivity, shown in Fig. 4.12, demonstrate that magnetoplasmons control the energy range in which the Faraday rotation is maximum. Figure 4.12a, presents models for the Faraday rotation of homogeneous graphene ($\omega_0 = 0$), the rotation in the presence of plasmons such as the one observed in our sample (6.5 meV) and for higher plasmon energies (20 and 40 meV). Clearly, the Faraday angle is maximum close to the magnetoplasmon resonance and therefore can be controlled not only by magnetic field but also by ω_0.

A way to increase the plasmon energy is to decrease the size of the homogeneous regions, which could be done, for example, by varying the miscut angle of the substrate. Similarly, in more conventional plasmonic materials the Faraday and Kerr angles are enhanced close to the plasma resonance [153, 167]. For example, recently Kerr rotation on the order of 10^{-4} to 10^{-3} radians was observed in an array of Au disks [153]. The rotation observed in graphene is more than 2 orders of magnitude larger, which is a direct consequence of the much smaller cyclotron mass, even though the carrier density per unit cell is also much lower than in noble metals. Here the measurements were performed at low temperature to maximally resolve the magnetoplasmonic spectral structures. However, in the classical limit (graphene with high doping) the Fermi-Dirac thermal filling factors play only a minor role in the optical conductivity, the amount of rotation in this regime is not expected to be significantly reduced at elevated temperatures. Moreover, in the quantum regime, where inter Landau level transitions are observed, the Faraday rotation persists at room temperature [168]. Thus we expect the magnetoplasmonic phenomena to survive at room temperature.

Figure 4.12b demonstrates a method to increase the amplitude of the Faraday rotation for a fixed plasmon energy. By reducing the electronic scattering, the rotation can be significantly increased. Rotations above 0.1 radians by just one atomic layer at a modest field of 1 T, where the energy range can be controlled via plasmons do not seem to be out of experimental reach. Therefore the combination of magnetoplasmons and the Faraday effect is even more promising for applications.

4.5 Conclusion

A giant Faraday rotation was observed in monolayer epitaxial graphene; $\theta > 0.1$ rad, which is much larger than initially predicted [139–142]. The Faraday rotation is strongly enhanced near the resonance energy. Although in two-dimensional electrons gases the cyclotron resonance gives rise to comparable absolute rotations [96, 142], the rotation comes from an effective layer which is about one order of magnitude thicker than mono-atomic graphene. Moreover, while in 2DEGs the cyclotron frequency is doping independent, in graphene it can be tuned with doping as seen from eqn. (3.25). Therefore, for low doped graphene, higher resonance energies can be achieved at the same fields.

The Faraday effect and the associated magneto-optical Kerr effect are widely used in optical communication, data storage and computing. For these applications a large rotation is desirable. The amplitude of the Faraday rotation is strongly determined by the charge scattering rate. Lower scattering results in a sharper resonance peak so that larger rotations are observed. Therefore it is important for future technologies to grow cleaner samples with higher mobilities.

However, the Faraday rotation is not only promising for future technologies but also provides a powerful contact-free tool to obtain experimentally the optical Hall conductivity and which can distinguish the type of the charge carrier. With access to

both the optical conductivity and the optical Hall conductivity the full magneto-optical conductivity tensor is obtained. Furthermore, with the help of the Kramers-Kronig relations, the magneto-optical conductivity in the basis of left and right handed circular polarization can be extracted.

After careful analysis of the optical conductivity and the optical Hall conducitivity, we found that morphological defects on the nanoscale such as atomic steps in SiC and wrinkles in epitaxial graphene produce a remarkably strong plasmon resonance in the terahertz energy range. This resonance has essentially the same origin as the plasmon peak observed in patterned two-dimensional electron gases and in nanostructured graphene. The important difference, however, is that the confinement potential in epitaxial graphene is intrinsic and does not require special lithographic patterning, with the risk to reduce the carrier mobility.

The presence of the plasmon dramatically changes the optical spectra. We used the phenomenological Drude Lorentz model for magneto-optical conductivity to fit the data, allowing us to determine the plasmon spectral weight, the cyclotron resonance energy, the plasmon energy and the carrier scattering. Indeed, the cyclotron resonance energy shows an almost perfect linear dependence on the magnetic field, as predicted for highly doped graphene. The energies of the two magnetoplasmon modes were calculated from the plasmon energy and the cyclotron resonance energy and match the peak positions on the resonances observed in $\sigma_-(\omega)$ and $\sigma_+(\omega)$.

In the view of future applications one needs to be able to actively control both the amplitude of the Faraday rotation and the energy region of maximum rotation, preferably at a moderate constant magnetic field. The amplitude can be maximized by minimizing the carrier scattering rate. Importantly, ambipolar doping of graphene offers a way of reversing the sign of the Faraday rotation, so that fast tunable magneto-optical devices could be envisioned. A promising way of controlling the energy range in which the rotation is maximum is provided by the dependence of the Faraday rotation on the plasmon energy. One can think of controlling the plasmon energy by varying the preparation of the substrate and the graphitization process.

In recent years, the field of terahertz science and technology has made a rapid development, fueled by the huge potential of terahertz radiation in imaging, spectroscopy, biomedical sciences, and integrated circuits. For those applications, THz plasmonic components like waveguides, based on surface plasmons are proposed due to the subwavelength confinement especially suitable for ultra small devices. However, waveguides purely based on plasmonics usually are two-way waveguides; light can propagate in the forward and the backward direction. For functional devices as isolators, rotators, switches and splitters used for example in laser technology, one-way waveguides are of great importance. These one-way waveguides could be realized with the help of Faraday isolators and Faraday mirrors. Therefore, the strong magneto-optical effects found in graphene, combined with its excellent plasmonic properties, makes the mono atomic material a perfect candidate for future terahertz technology.

5

Single-layer epitaxial graphene at high magnetic fields

5.1 Introduction

In this chapter we continue our work on doped single layer epitaxial graphene grown on the silicon side of SiC in which the silicon dangling bonds were passivated by hydrogen. Whereas, in the previous chapter the high doping of the graphene, even at 7 T, firmly kept the optical transitions observed in the classical limit, showing cyclotron resonance linearly dependent on field. Here, we report magneto-transmission experiments at much higher magnetic fields, up to 32 T, directly revealing the classical-to-quantum crossover of the cyclotron resonance in graphene, as will be shown in section 5.3.

The high magnetic field spectra allow us to observe steps in the cyclotron resonance energy at integer filling factors, from which the carrier density (section 5.4.1) is directly extracted. Next, we study the effect of carrier scattering and a distribution of the Fermi energy on the classical to quantum crossover by comparing the experimental data to model data using the Kubo formula (section 5.4.2). The cyclotron mass and the Fermi velocity are extracted, which are vital in obtaining the Fermi energy (section 5.4.3).

In the last part of this chapter we contribute to the ongoing discussion about the renormalization of the Drude spectral weight in graphene [97–100]. The spectral weight of the cyclotron resonance obtained from the fits is compared to the predicted spectral weight based on the effective single-particle picture [31].

In this chapter we will indicate Landau level indices not with the commonly used n, but with the symbol m. This change in notation is restricted to this chapter and made to avoid confusion in the discussion about the carrier density n.

Most of the results presented in this chapter were published in M. Orlita *et al*. New Journal of

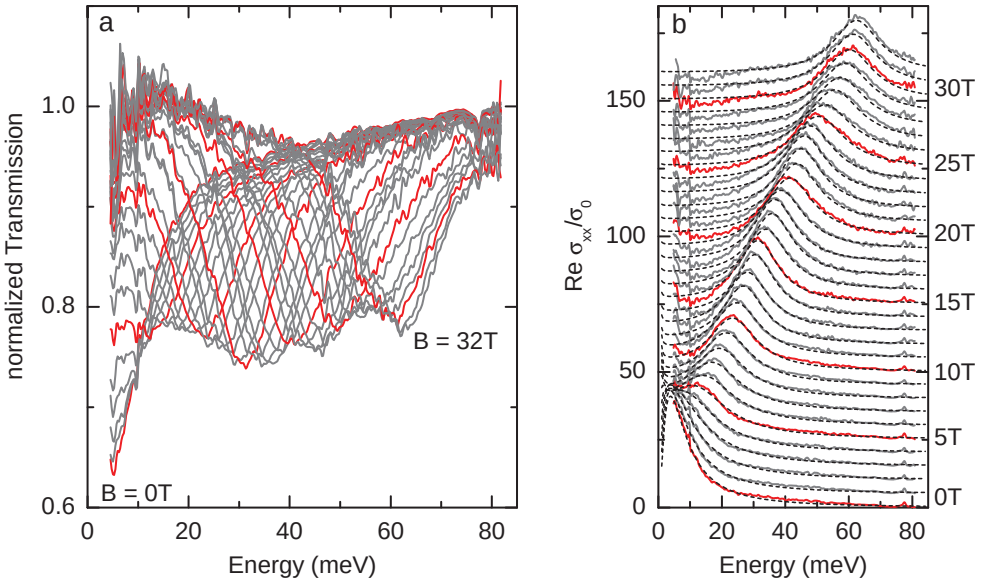

Figure 5.1: (a) Substrate normalized transmission spectra. The red curves correspond to B = 0, 5, 10, 15, 20, 25 and 30 T. (b) Real part of the optical conductivity extracted from the transmission spectra. The curves have an offset of $5\sigma_0$ per Tesla. The red curves corresponds with the red transmission curves in (a). The black dashed lines on top of the spectra are fits using the Drude Lorentz model for the magneto-optical conductivity.

5.2 Experimental details

A single layer of carbon was grown by thermal decomposition of the silicon terminated substrate of 6H-SiC, hydrogen intercalation between buffer layer and substrate was used to passivate the silicon bonds. A more detailed discussion of the growth process this given in section 3.4.1. As was shown in the previous chapter, this type of epitaxial graphene is highly p-doped, with a Fermi energy $|\epsilon_F| \sim 0.3$ eV, which was found from mid infrared transmission measurements visualizing the $2|\epsilon_F|$ onset in the absorption.

The high field transmission measurements were done at the Grenoble High Magnetic Field Lab (LNCMI). Fields up to 32 T were delivered by a resistive coil. The sample and the bolometer were placed in the center of the coil and kept at 1.8 K. The light from a globar, modulated by a Fourier transform spectrometer, was lead to the sample via light-pipe optics. The size of the sample was 5 mm^2, of which about 4 mm^2 was exposed to the light.

From the substrate normalized transmission $T(B)$, the real part of the optical conductivity, Re $\sigma_{xx}(\omega)$, was obtained for each magnetic field, using the thin film relation (eqn. (2.47)). The details concerning eqn. (2.47) are discussed in section 2.3.1, while its limitations are shown in appendix B.1.

Physics **14**, 095008 (2012).

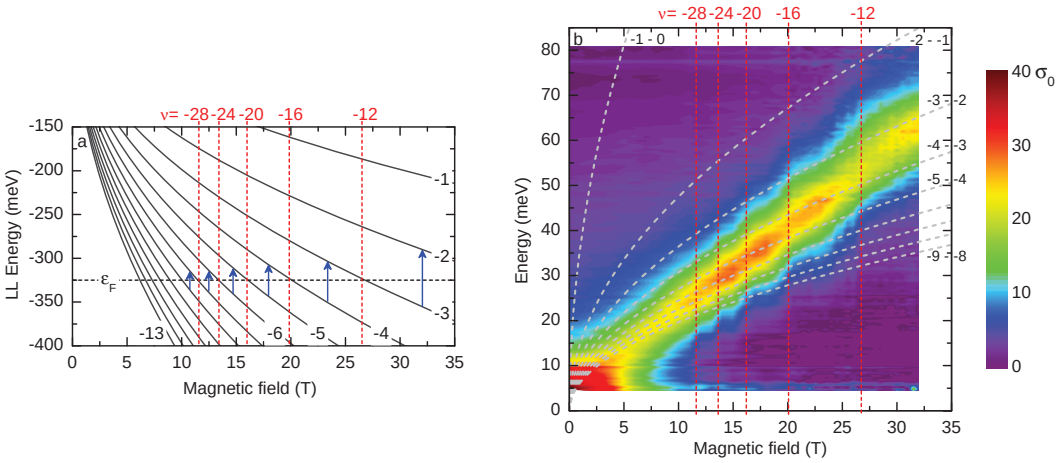

Figure 5.2: (a) Magnetic field dependence of the hole-like Landau levels (m = -1, -2,... -13), where v_F = 10^6 m/s. The Fermi energy (325 meV), indicated by the black dashed line, which was determined for this specific sample (see section 5.4.1). The blue arrows correspond to optical transitions between adjacent Landau levels. At integer filling factors, indicated by the red dashed lines, the Fermi energy crosses the Landau levels. (b) Color plot of the experimental conductivity spectra, the dashed red lines show the filling factors also indicated in (a). The grey dashed lines correspond to the excitation energies of optical transitions between the Landau levels.

5.3 Results: classical to quantum crossover

The substrate normalized transmission is shown in Fig. 5.1a, for fields from 0 to 32 T, where between 0 and 20 T the spectra were measured at every Tesla and between 20 and 32 T the spectra are taken at every half Tesla. However, for clarity only spectra at integer fields are shown in Fig. 5.1a and b. The red lines correspond to B = 0, 5, 10, 15, 20, 25 and 30 T. In Fig. 5.1b the real part of the optical conductivity extracted from the transmission spectra, is presented. The curves are offset with $5\sigma_0$ per Tesla, the red curves correspond to the same fields as the red curves in Fig. 5.1a: B = 0, 5, 10, 15, 20, 25 and 30 T. In agreement with previous studies on highly doped graphene [138, 169, 170], quasi-classical cyclotron resonance is observed; the cyclotron resonance energy, roughly corresponding to the peak position in $\sigma_{xx}(\omega)$, shows a linear dependence on the magnetic field. However, at low magnetic fields ($\sim$ B < 10 T), the peak position in $\sigma_{xx}(\omega)$ is strongly influenced by the plasmon energy, as was shown in the previous chapter.

At high magnetic fields, the resonance peak in $\sigma_{xx}(\omega)$ still follows an overall linear-in-B evolution. However, when studying the spectra in Fig. 5.1b closely one can see that the peak position shows some deviations from a linear evolution. Whereas for the low magnetic fields the Fermi energy is rapidly crossing the Landau levels when the field is increased, at higher fields ($\sim$13 T) the range of magnetic fields between

adjacent filling factors becomes much larger, so that the square-root dependence of the Landau levels can be observed. This gradual crossover between linear and square-root evolution is best seen in Fig. 5.2a and b. Figure 5.2a showd the energies of the hole-like Landau levels for index m = -1 to -13 as a function of magnetic field (with v_F = 10^6 m/s). The (constant) Fermi energy is indicated by a black dashed line. One can see that at low fields the Fermi energy often crosses Landau levels, selecting different optical transitions between the Landau levels. The crossing between ϵ_F and a Landau level corresponds to an integer filling factor, indicated by the red dashed lines. At high fields the magnetic field range between the adjecent integer filling factors becomes larger. In Fig. 5.2b the experimental conductivity spectra are plotted in a contour plot. For fields above $\sim$ 13 T, steps in the resonance energy are observed, which is a clear sign of the approaching quantum regime. The observed cyclotron resonance corresponds to optical transitions between adjacent Landau Levels, where the Landau level excitation energies have a $\sqrt{B}$-dependence. The energies of the hole-like transitions $L_{-m-1} \rightarrow L_{-m}$, indicated by the light grey dashed lines in Fig. 5.2b, are:

$$\omega_c = E_{-m-1} - E_{-m} = -E_1(\sqrt{m+1} - \sqrt{m}), \tag{5.1}$$

where $E_1 = \sqrt{2\hbar v_F^2 |eB|}$ is the energy of the first Landau level and m is a positive integer corresponding to the absolute number of the Landau levels.

The red dashed lines in Fig. 5.2b are placed at the magnetic fields where the cyclotron resonance energy shows a step-like structure: at B_m = 11.5, 13.5, 16, 20 and 27 T (placed at identical fields as the filling factors in Fig. 5.2a). This sequence of field values matches the simple rule $|m|B_m$ = constant (with $|m|$ = 7, 6, 5, 4 and 3) and allows us to identify the filling factors ν = -4m, which correspond to the half-filled last occupied Landau Level.

The conductivity spectra in Fig. 5.1b were fitted with the phenomenological Drude-Lorentz formula for the magneto-optical conductivity using one oscillator (eqn. (2.27), where $n = 1$). Although at B = 0 T no peak at finite energy is observed directly in the experimental spectra. The presence of a plasmonic resonance can be readily observed in Fig. 5.2; the peak energy does not extrapolate to zero energy at B = 0 T, but to about 5 meV. Therefore for the fits we used a field independent plasmon energy, ω_0, of 5 meV. From the fitting the cyclotron resonance energy, ω_c, the spectral weight and the broadening of the transition, γ, are extracted. Figure 5.3a shows ω_c as a function of field, the energy steps, also visible in the contour plot (Fig. 5.2b), are clearly present. The dashed lines correspond to the same fields are the lines in Fig. 5.2b. Figure 5.3b shows both the spectral weight of the resonance and the broadening as a function of field.

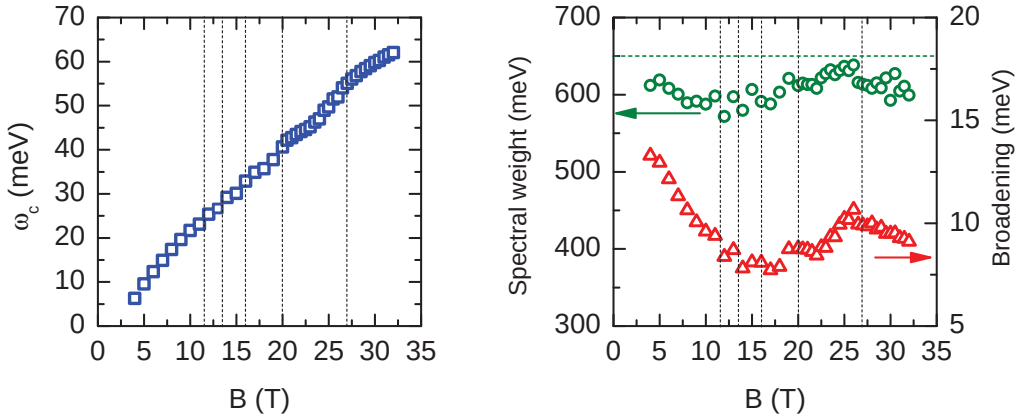

Figure 5.3: Results of the fitting with the phenomenological model for the magneto-optical conductivity; (a) the cyclotron resonance energy. Note that ω_c was obtained by fitting the optical spectra with the Drude-Lorentz model, while ω_0 was fixed at 5 meV. (b) The spectral weight and the broadening of the optical transition. The dashed lines in both graphs are placed at integer filling factors.

5.4 Discussion

5.4.1 Carrier concentration

The sequence of steps observed in the cyclotron resonance energy at $m\mathrm{B}_m$ = constant, is compatible with two possible scenarios. Either the Fermi level in graphene is pinned by electronic states in the SiC substrate, in other words, ϵ_F = const = $\sqrt{2\hbar v_F^2 |emB_m|}$, or alternatively, the carrier density remains constant with varying B. Even though charge transfer between the substrate and graphene cannot be excluded (ϵ_F = constant), one would expect to see a large influence of the charge transfer on the spectral weight of the cyclotron resonance. In epitaxial graphene on silicon terminated SiC, this effect has not been observed so far.

Importantly, for both scenarios, the carrier density at B = 0 and at every B_m is $n = 4emB_m/h$ = (7.9±0.2)×10^{12} cm^{-2}. This value of the carrier density was extracted entirely from the Landau level occupation, thus completely independent of v_F and ϵ_F. This represents a significant advantage over previous studies of graphene in the quasi-classical regime [138, 170].

5.4.2 Distribution of the Fermi energy

The observation of individual filling factors in the experimental data, revealed as well-defined steps in the position of the cyclotron resonance peak in Fig. 5.2 is a first indication of the high homogeneity of the Fermi energy. The conditions to observe the steps in the cyclotron resonance energy are that (i) the carrier scattering has to be low and (ii) the distribution of Fermi energy has to be small throughout the entire sample.

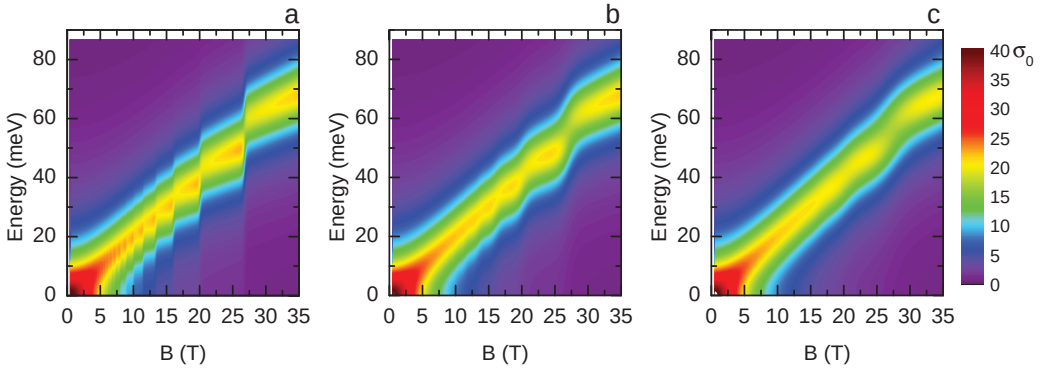

Figure 5.4: Color plot of the model conductivity for (a) T = 10 K, (b) T = 50 K and (c) T = 100 K.

In the previous chapter, we have seen that the broadening in this type of graphene is about 12 meV at 0 T and decreases to about 10 meV at 7 T. The fitting results obtained with the high magnetic field spectra show a similar trend for the broadening: at low fields the broadening is about 13 meV, while it drops down to almost 7 meV before stabilizing at high fields at around 10 meV. The decrease of the broadening at high fields is due to the smaller influence of the plasmon energy on the cyclotron resonance transition, therefore sample inhomogeneity plays a smaller role at high fields. However, the broadening could also be caused (for some part) by a distribution in the chemical potential across the graphene. Notably, strong doping inhomogeneity and electron-hole puddles were observed in graphene on a Si/SiO_2 substrate [171].

To visualize the influence of spatial variations in the chemical potential we modeled the magneto-optical conductivity of an isolated graphene layer using the Kubo formalism for single layer graphene (see sections 3.3.3 and 2.2.3), for fields from 0.4 to 35 T. The carrier scattering, γ, is assumed to be independent of Landau level number and energy. The Fermi energy of the graphene was fixed at 325 meV. In the model for the optical conductivity (eqn. (3.27)) the effects of plasmons and magneto-plasmons are not incorporated, however at high magnetic fields the cyclotron resonance energy is much larger than the plasmon energy and therefore the spectra are dominated by cyclotron resonance and Landau level transitions.

Figure 5.4 shows color plots of the model $\sigma_{xx}(\omega)$ for a fixed broadening of 10 meV. To account for a distribution in the Fermi energy in the graphene layer the temperature was varied from 10 to 50 and 100 K. The Fermi-Dirac distribution, which takes into account the effect the Fermi energy and the temperature, forms a linear term in the Kubo formula (eqn. (3.27)), therefore raising the temperature has a similar effect as introducing a distribution in Fermi energy (note that we assume the Fermi energy to be temperature independent).

In Fig. 5.4a, T=10 K, which corresponds to a variation in the Fermi energy of only about 0.9 meV. The step-like structures in the model are somewhat sharper than the ones observed in the experimental data, while γ corresponds to the average broaden-

ing extracted from the spectra. By increasing the temperature in the model the step-like structures become less sharp, as is observed in Fig. 5.4b, where T = 50 K, and Fig. 5.4c, where T = 100 K. In comparison with the experimental data, shown in Fig. 5.2, a temperature of about 50 K shows the best match between model and experiment, whereas 100 K clearly shows less sharp structures than observed in the experiment. The Fermi energy spread corresponding to 50 K is about 4.6 meV, which is remarkably small for graphene on a substrate and underlines once more the quality of epitaxial graphene. Note that the actual spread in Fermi energy might be somewhat smaller or larger since the exact distribution curve is not known.

5.4.3 Cyclotron mass, Fermi velocity and Fermi energy

Using the classical relation for cyclotron frequency, $\omega_c = eB/m_c$, the cyclotron mass can be extracted from the magnetic field dependence of the cyclotron resonance energy, plotted in Fig. 5.3a. From $\omega_c(B)$ we find that m_c = 0.058±0.01 m_e, where m_e is the free electron mass. This is in close agreement with the cyclotron mass extracted in the previous chapter (m_c = 0.055 m_e) from low field ($\leq$ 7 T) measurements on a similar sample.

Using the relation $|\epsilon_F| = m_c v_F^2$ (eqn. (3.24)), together with $|\epsilon_F| = \hbar v_F \sqrt{\pi |n|}$, we obtain an expression for v_F depending on m_c and the carrier density n: $v_F = \hbar\sqrt{\pi|n|}/m_c$. The carrier density, n = (7.9±0.2)×10^{12} cm^{-2}, was determined previously in section 5.4.1 and for the cyclotron mass we use m_c = 0.058±0.01 m_e. We find that v_F = (0.99±0.02)×10^6 m/s. In a next step, using either $|\epsilon_F| = m_c v_F^2$ or $|\epsilon_F| = \hbar v_F \sqrt{\pi|n|}$, the Fermi energy, $|\epsilon_F|$ = 325±5 meV, is extracted.

5.4.4 Spectral weight

The optical conductivity can be described using the simple model of non-interacting Dirac-fermion quasiparticles with the characteristic linear dispersion. Such an effective single-particle picture [31] correctly reproduces the measured strength of interband-absorption processes with the characteristic onset at $2|\epsilon_F|$ and the constant universal conductivity, $\sigma_0 = e^2/4\hbar$ [38–41, 172, 173]. In the light of the effective single-particle picture the Drude spectral weight, $D = \int_0^\infty \sigma_{intra}(\omega) d\omega$, can be expressed as:

$$D = \frac{E^2 v_F \sqrt{\pi|n|}}{2\hbar} = \frac{\pi|n|e^2}{2m_c} = \frac{2\sigma_0|\epsilon_F|}{\hbar} \tag{5.2}$$

where $m_c = |\epsilon_F|/v_F^2$. The experimental measurements available so far [99, 100] are in conflict with this prediction. They suggest a suppression of the Drude weight up to 40% (notably, in graphene samples with high carrier concentrations). Therefore, it is an open question whether the effective single-particle picture correctly describes the dynamical conductivity of graphene. These doubts are additionally fostered by a startling report on non-vanishing absorption below the $2|\epsilon_F|$ threshold for interband

processes [42, 174]. Importantly, a discrepancy between the experimental spectral weight and the weight expected based upon the effective single-particle picture could point at interactions between quasiparticles in graphene.

According to the effective single particle model, the expected Drude weight found from the experimentally obtained Fermi energy $D\hbar/\sigma_0 = 2|\epsilon_F| = 650\pm10$ meV. Additionally, the Drude weight can also be directly extracted from our data by estimating the area under optical excitation in $\sigma_{xx}(\omega)$. To account for the partial transfer of the Drude weight into the lower magneto-plasmon branch, the spectra were fitted with the Drude-Lorentz formula, assuming the confined-plasmon frequency of $\omega_0 = 5$ meV (see section 5.3). The fits directly reveal the spectral weight of the cyclotron resonance peak, which is plotted in Fig. 5.3b as a function of field. The spectral weight extracted from the fits is slightly varying around 600 meV, which is smaller than the expected spectral weight based on the Fermi energy. We note that the Drude weight is fully transformed into the strength of the cyclotron resonance absorption in the classical limit and, with a good precision, into the strength of inter-Landau-level transitions in the quantum limit.

In order to compare both estimates of the Drude weight, the following corrections should be taken into account: (i) the coverage of the substrate by graphene is probably not 100% but around 95% (see AFM measurements on the similarly prepared sample discussed in section 4.3.3 of the previous chapter), (ii) the hydrogenization process to passivate silicon dangling bonds is not always complete: a small part of the sample remains covered only by the 'Bufferlayer' [175], (iii) bilayer graphene may also appear at selected locations [76] and last (iv) the area below the experimental $\sigma_{xx}(\omega)$ spectra, extracted using the thin film relation (eqn. (2.47)), is suppressed with respect to the Drude weight, the underestimation for these spectral weights and fields could be up to 7%, see appendix B.1. All these considerations show that deducing the Drude weight from the fit could result in an underestimation of the real spectral weight by approximately 5 to even 15%. Therefore, we find that our two independent estimates of the Drude weight agree with each other and should conclude that we do not observe any significant deviation from the validity of the effective single particle model. These findings are in excellent agreement with a recent theoretical work [98], which predicted based on many-body diagrammatic perturbation theory that the Drude weight in doped graphene should be in close agreement with the effective single-particle picture due to a competition between self-energy and vertex corrections.

Our findings on the cyclotron resonance spectral weight thus do not support recent transmission studies [99, 100] in which a significant suppression of the Drude weight in comparison with the effective single particle expectation has been reported. The reason for this discrepancy remains unclear at the moment, although we believe that at least some part of the suppression of the Drude weight reported in [99] might stem from the normalization procedure used, in which the Drude-type absorption of graphene in the regime of electron-hole puddles (when the sample is neutral on average) is neglected [171]. For a more detailed discussion of the Drude spectral weight in single layer epitaxial graphene on SiC see Ref. [176].

5.5 Conclusion

To conclude, we observed the evolution of an optical transition in single layer epitaxial graphene from the quasi-classical cyclotron resonance into the quantum-like transitions between individual Landau levels. The optical spectra, plotted as a function of field, clearly reveal step-like structures at integer filling factors. The carrier density was extracted directly from the Landau level degeneracy at these filling factors.

The magneto-optical conductivity was fitted using the phenomenological Drude-Lorentz model, from which the cyclotron resonance energy, the broadening and the spectral weight were found for all magnetic fields. The cyclotron resonance energy shows the same step-like structures already observed in the conductivity, which are associated with the occupation level shifting from a high Landau level to a lower one. The broadening of the optical transition proves to be small. By using a model of the conductivity of graphene we show the effects of larger broadening and a possible distribution of the Fermi energy across the sample. From the modeling we conclude that this spread should be as small as $\sim$ 4 to 5 meV to observe the clear step-like structures, whereas the Fermi energy itself is about 325 meV. This incredibly small variation underlines the good quality of single layer epitaxial graphene.

Last, it was shown that the oscillator strength of the cyclotron resonance found from the fitting procedure is in a good agreement with the Drude weight expected from the effective single-particle picture, where $D = 2|\epsilon_F|\sigma_0$. Therefore, the single-particle-like picture is sufficient to account for our data. This stands in contrast with earlier optical studies of the Drude weight [99, 100], which observed a suppression of the weight.

6

Multi-component optical conductivity in multilayer graphene

6.1 Introduction

The electronic properties of epitaxial graphene grown on Si- and C-faces of SiC, are markedly different [86, 177]. Importantly, multilayer epitaxial graphene on the carbon face shows a number of electronic features typical of isolated monolayer graphene as revealed by infrared spectroscopy [53], scanning tunneling microscopy (STM) [57, 82], angle-resolved photoemission spectroscopy (ARPES) [85] and quantum Hall effect [128]. In particular, the Landau levels in this material demonstrate a square-root dependence on the perpendicular magnetic field B and the level index n.

It is generally believed that such an effective electronic decoupling of the layers is a result of a twisted, non-Bernal stacking of the C-face grown graphene layers. Significant progress in theoretical understanding of the influence of stacking on the electronic structure and Landau levels was made [4, 87–94]. However, no complete theory able to quantitatively predict the effect of twisting on the band structure at an arbitrary stacking angle exists at the moment even for bilayer graphene. In practise, many layers are present with a random rotation between each pair of neighboring layers. Moreover, the substrate induces a strong variation of the Dirac-point energy E_D with respect to the chemical potential and therefore a very different density and mobility of carriers in different layers. More experiments are needed to understand the complex electronic structure of this system and establish favorable conditions for applications.

In parts of this chapter we follow closely our work the published in I. Crassee *et al.*, Phys. Rev. B **84**, 035103 (2011).

In this chapter we present an extensive magneto-optical study of multilayer epitaxial graphene grown on the carbon side of SiC, by combining the Faraday rotation measurements with the transmission spectra and extracting both the diagonal and Hall optical conductivity. Spectra were measured on a 'thin' multilayer sample, with on average a coverage of 6 graphene layers (section 6.3) and a 'thick' multilayer sample, with about 17 rotationally stacked layers (section 6.4). For the 6 layer sample, also the dependence of optical spectra on temperature and environmental (surface) doping are studied. Different magneto-optical contributions, such as cyclotron resonance and Landau level transitions, are disentangled and studied quantitatively using a multi-component cyclotron model. This analysis allows us to analyze optical intensities of the various transitions and make comparison to theoretical models. The most unexpected result of this study is the anomalously small spectral weight found for the optical transitions between the lowest Landau levels (section 6.5.3), which clearly does not agree with the picture of multilayer graphene as a stack of isolated mono layers.

6.2 Experimental details

The type of epitaxial graphene under investigation in this chapter is rotationally stacked multilayer graphene grown on the carbon side of SiC. All samples are prepared on a SiC substrate with a typical thickness of about 370 μm and a surface area of 10×10 mm^2. The backsides of the samples were checked to be free of graphene by x-ray photoemission spectroscopy (XPS). The reference substrate is prepared from the same SiC wafer. The two samples from which experimental results are presented in this chapter have about 6 and 17 graphene layers, respectively. The layer thickness was determined by XPS and by mid infrared microscopy on random spots on the sample. The layer closest to the SiC interface is highly electron doped, while in subsequent layers the Dirac point is shifted towards the Fermi energy. The outmost layers are close to neutral doping. More details and the synthesis method of multilayer graphene on SiC were discussed in section 3.4.2.

The Faraday rotation $\theta(\omega)$ and magneto-optical transmission $T(\omega)$ were measured in the energy range between 8 and 85 meV. The optical transmission was measured with respect to the bare SiC substrate without graphene. The optical spot had a diameter of 5 mm. During the experiment both the field dependence (at T = 5 K) and the temperature dependence (at B = 3 T) of the optical spectra were measured.

6.3 Results on 6 layer graphene

The substrate normalized transmission and Faraday rotation observed in multilayer graphene, as plotted in Fig. 6.1a and b, are strikingly different from single layer graphene. Apart from the low energy resonance, both the Faraday angle and absorption spectra show additional, strongly field dependent resonance structures at higher ener-

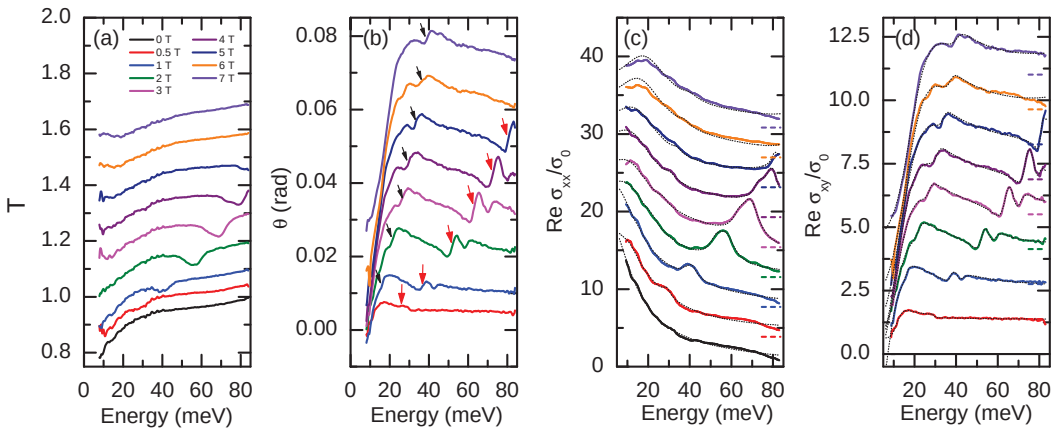

Figure 6.1: Magneto-optical spectra of 6 layer graphene at 5 K for several magnetic fields up to 7 T. The curves in all panels are offset. Larger offsets correspond to higher magnetic fields. Panels (a) and (b) show the measured substrate normalized transmission and the Faraday rotation spectra, respectively. The red and black arrows in panel (b) point at the $0 \rightarrow 1$ and the $1 \rightarrow 2$ Landau level transitions. In panels (c) and (d) the reals parts of $\sigma_{xx}(\omega)$ and $\sigma_{xy}(\omega)$ (solid lines) and multi-component fits (black dotted lines), normalized to the universal conductivity σ_0 are plotted. The curves are offset for clarity. The offset per curve is indicated by the straight dashed lines on the right hand side of the graphs.

gies, indicated by the arrows in Fig. 6.1b. As was found in previous studies [53, 54], these spectral features correspond to optical transitions between individual LLs. The series of transitions with energies $E_1 - E_0$ and $E_2 - E_1$ can be identified from the spectra.

The spectral features observed in the Faraday rotation show an antisymmetric structure, where the inflection point in the curve corresponds to the peak position observed in the transmission spectra, see section 3.3.3. The slope at this point coincides with the sign of the cyclotron frequency and reveals the polarity of the charge carriers involved in the transition [138]: a positive (negative) slope signals electron (hole) like carriers. For epitaxial graphene on the Si side of SiC we found a negative slope and hole doping. On the contrary, the sign of the slopes observed in the Faraday rotation measured on epitaxial graphene grown on the C side of SiC is (mostly) positive. Therefore the Faraday rotation results (mostly) from optical transitions between electron like Landau levels, such as the $0 \rightarrow 1$ and the $1 \rightarrow 2$ transitions indicated in Fig. 6.1b by the red and black arrows respectively. The low frequency part of the spectra features a cyclotron-resonance like structure, similar to the data on single layer graphene, but with opposite sign of the charge carriers.

The real parts of the diagonal, $\sigma_{xx}(\omega)$, and Hall, $\sigma_{xy}(\omega)$, optical conductivities can be directly obtained from the transmission and Faraday rotation spectra by using the general thin-film approximation, taking internal reflections in the substrate into account. For the details concerning the thin film relations, see sections 2.3.1 and 2.3.3. The spectral features observed in multilayer graphene are several times weaker than

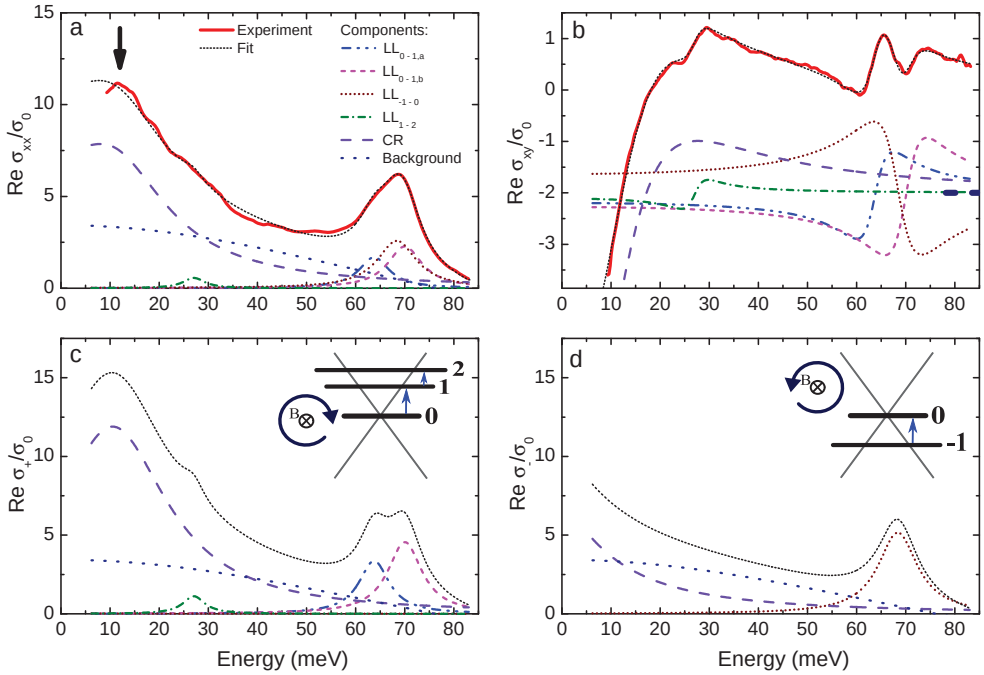

Figure 6.2: The diagonal (a) and Hall (b) optical conductivity at 3 T and 5 K, normalized to the universal conductivity σ_0, for 6 layer graphene. Also plotted: results of the multi-component modeling described in the text. The components in the graph are the individual contributions needed to create the total fit shown by the black dotted line on top of the data. The components in panel (b) have an offset indicated by the blue dashed line at the right side of the graph. Panels (c) and (d): the optical conductivities in the circular basis $\sigma_+(\omega)$ and $\sigma_-(\omega)$ corresponding to the absorption of right and left circular polarized light respectively. In the insets the low-index LL transitions allowed in the corresponding polarizations are shown.

the absorption observed in monolayer graphene, therefore we can use the linear thin film approximation, eqn. (2.49). We reduced the spectral resolution to 1 meV in order to suppress the Fabry-Perot interference in the substrate.

The obtained magneto-optical conductivities are plotted in Fig. 6.1c and d. The diagonal conductivity spectra clearly show a Drude like response at the low energies, which evolves into cyclotron resonance in magnetic field, signaling high doping. At higher energies a peak with a square-root dependence on field emerges, which originates from Landau level transitions. Similarly, the off-diagonal conductivity shows a large structure at the low energies corresponding to the cyclotron resonance. In addition, the Landau level transitions are clearly visible at higher energies.

6.3.1 Magneto-optical conductivity at 3 T and 5 K

Figure 6.2 shows the magneto-optical conductivity spectra at $B = 3$ T and $T = 5$ K. The diagonal and Hall conductivities, normalized by σ_0, are plotted as solid lines in Fig. 6.2a and 6.2b. The rich structure of the spectra indicates the presence of multiple optical transitions. The absorption at low energy, shown by the arrow, corresponds to quasi-classical CR coming from the highly doped graphene layer closest to the SiC substrate [138]. At about 60 to 70 meV, a strong peak in $\sigma_{xx}(\omega)$ is observed that matches the energy of the $0 \rightarrow 1$ or $-1 \rightarrow 0$ LL transitions at this field. The Hall conductivity displays a 'zig-zag' shape in this spectral range, suggesting that there are multiple components contributing to the optical response. In addition, a structure is present at about 27 meV, most clearly seen in $\sigma_{xy}(\omega)$, resulting from the $1 \rightarrow 2$ LL transition.

In order to disentangle different contributions to the magneto-optical spectra we used a multi-component model, eqn. (2.27) and eqn. (2.28), where the total conductivity is given by a sum of separate cyclotron resonances. Each of the i components has a cyclotron frequency, $\omega_{c,i}$, a spectral weight D_i and a broadening γ_i, while the resonance frequency $\omega_{0,i} = 0$. Physically speaking, each component can describe either a quasi-classical cyclotron resonance or a transition between individual Landau Levels separated by energy $|\hbar\omega_{c,i}|$. Notably, $\sigma_{xx}(\omega)$ does not depend on the sign of the charge carriers, unlike $\sigma_{xy}(\omega)$, where the sign can be derived directly from the spectral shape [138]. In $\sigma_{xx}(\omega)$ each component results in a peak centered at $|\omega_{c,i}|$. In $\sigma_{xy}(\omega)$ however, it shows an antisymmetric structure, where $|\omega_{c,i}|$ corresponds to the inflection point in the curve, see section 3.3.3. A negative slope at this point reveals hole doping, while a positive slope corresponds to electron like doping.

The spectra $\sigma_{xx}(\omega)$ and $\sigma_{xy}(\omega)$ were simultaneously fitted using eqns. (2.27) and (2.28), while allowing the parameters $\omega_{c,i}$, D_i and γ_i to change freely. The fitting curves are shown in Fig. 6.2a and 6.2b, as black dotted lines. We found that a minimal model describing satisfactorily the spectral structures contains six components, which are shown separately in the same panels by additional curves.

Interestingly, it was necessary to introduce at least three components with transition energies between 60 meV and 70 meV to describe the structure in this range. Two of the resonances are electron like, which we designate as $\mathrm{LL}_{0\rightarrow1,a}$ and $\mathrm{LL}_{0\rightarrow1,b}$, and one is hole like, referred to as $\mathrm{LL}_{-1\rightarrow0}$ (the symbol $\mathrm{LL}_{i\rightarrow j}$ is used to designate the LL transition between levels i and j). Note that all these transitions are actually at different energies, which is clearly seen already from the presence of three inflection points in the optical Hall conductivity. A fourth component is at about 27 meV and corresponds to the electron like $\mathrm{LL}_{1\rightarrow2}$ transition. The fifth component with a small value of $\hbar\omega_c$ = 9 meV originates from a quasi-classical electron like cyclotron resonance. Finally, there is a component with zero cyclotron frequency and large scattering, which forms a broad absorption background present in $\sigma_{xx}(\omega)$, but absent in $\sigma_{xy}(\omega)$. The possible origin of this background will be discussed in section 6.5.3.

6.3.2 Basis of circular polarized light

The absorption of right- and left-handed circular polarizations (which are shown in the insets of Fig. 6.2c and 6.2d) is described by the real parts of $\sigma_+(\omega)$ and $\sigma_-(\omega)$ respectively. This basis provides an intuitive way to present the magneto-optical conductivity showing individual LL transitions, which are active for strictly one circular polarization or the other [127, 131, 159]. In particular, for right circularly polarized light, transitions between electron like Landau levels with $n \geq 0$, such as $\mathrm{LL}_{0\to1}$, $\mathrm{LL}_{1\to2}$ etc, are active, provided that the chemical potential is in between the corresponding Landau Levels. Similarly, for left circularly polarized light, transitions between hole like Landau levels, ($\mathrm{LL}_{-1\to0}$, $\mathrm{LL}_{-2\to-1}$, etc.) are excited. (Note that also transitions between electron- and hole like Landau levels are optically allowed. However, for the magnetic fields used, these transitions are beyond the experimental spectral range, except at 0.5 T, where rather weak contributions from $\mathrm{LL}_{-1\to2}$ and $\mathrm{LL}_{-2\to1}$ could be observed.)

The magneto-optical conductivity in the basis of circular polarization can be obtained using eqn. (2.19), as discussed in section 2.2.2. From eqn. (2.19) one can see that the imaginary part of $\sigma_{xy}(\omega)$ is needed to obtain the real part of the magneto-optical conductivity in the circular basis. Experimentally, $\mathrm{Im}[\sigma_{xy}(\omega)]$ is directly related to the ellipticity of the transmitted light. However, in the present experiment the error bars on the ellipticity are larger than the ones on the Faraday angle. Therefore, we extract the imaginary part of $\sigma_{xy}(\omega)$ and the real part of $\sigma_{xx}(\omega)$ using the multi-component fitting discussed in section 6.3.1. Instead of directly applying eqn. (2.19) to the experimental data, we use the fitting results to plot $\sigma_\pm(\omega)$.

Figure 6.2c and 6.2d show the magneto-optical conductivity at 5 K and 3 T obtained from the fitting results shown in Figs. 6.2a and b. The electron like transitions $\mathrm{LL}_{0\to1,a}$, $\mathrm{LL}_{0\to1,b}$, $\mathrm{LL}_{1\to2}$ as well as the cyclotron resonance peak are visible in $\sigma_+(\omega)$, while the hole like $\mathrm{LL}_{-1\to0}$ transition manifests itself in $\sigma_-(\omega)$. Because of the small value of ω_c and a relatively large scattering, the cyclotron resonance component has also a tail in $\sigma_-(\omega)$. The absorption background contributes equally to $\sigma_+(\omega)$ and $\sigma_-(\omega)$.

6.3.3 Dependence on magnetic field

The magnetic field dependence of $\sigma_{xx}(\omega)$ and $\sigma_{xy}(\omega)$, measured at 5 K, is shown in Figs. 6.1c and 6.1d. Indeed a multi-component character of the spectra can be observed at the different fields, even though the resonances show a strong field dependence. The six component model described in section 6.3.1 was used to fit $\sigma_{xx}(\omega)$ and $\sigma_{xy}(\omega)$ simultaneously for every field. The multi-component fits, shown as black dotted lines in Figs. 6.1c and 6.1d, are used to calculate the magneto-optical conductivities in the basis of right and left handed circularly polarized light according to eqn. (2.19), which are plotted in Figs. 6.3a and 6.3b, respectively.

Similarly to what was already observed in Figs. 6.2c and 6.2d, one can see that

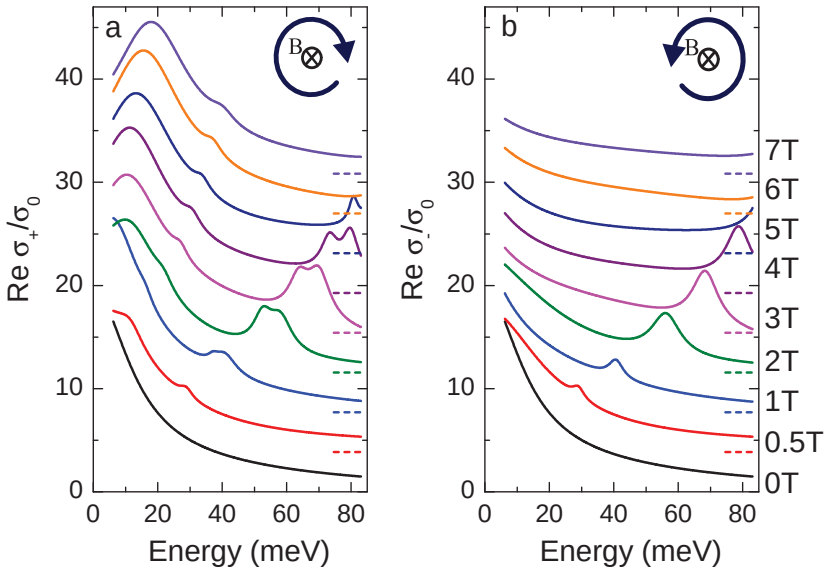

Figure 6.3: The model-derived magneto-optical conductivity of 6 layer graphene at 5 K, in the basis of right (a) and left (b) circular polarization normalized to the universal conductivity σ_0, for several magnetic fields up to 7 T. The curves in all panels are offset as indicated by the dashed lines. Larger offsets correspond to higher magnetic fields.

$\sigma_+(\omega)$ (Fig. 6.3a) shows a somewhat more rich structure than $\sigma_-(\omega)$ (Fig. 6.3b). Whereas in $\sigma_-(\omega)$ only one peak corresponding to the hole like $\mathrm{LL}_{-1\to0}$ transition is clearly distinguishable, in $\sigma_+(\omega)$ cyclotron resonance transitions linear in field and at least three Landau level transitions at higher energies are present.

6.3.4 Temperature dependence

The temperature dependence of $\sigma_{xx}(\omega)$ and $\sigma_{xy}(\omega)$ at a field of 3 T is shown in Fig. 6.4a and 6.4b, respectively. In both sets of curves, the low energy cyclotron resonance structure changes only weakly with temperature. The Landau level transitions however, show a very different temperature dependence. In $\sigma_{xx}(\omega)$ the structure originating from the combination of the $\mathrm{LL}_{0\to1,a}$, $\mathrm{LL}_{0\to1,b}$ and $\mathrm{LL}_{-1\to0}$ transitions is preserved at all temperatures, although at elevated temperatures the individual peaks are about 3 meV broader than at low temperatures as obtained from the multi component fits shown as the black lines in the same graphs. The spectral weight of the $\mathrm{LL}_{0\to1,a}$, $\mathrm{LL}_{0\to1,b}$ and $\mathrm{LL}_{-1\to0}$ transitions is almost temperature independent. However, in $\sigma_{xy}(\omega)$, the spectral features corresponding to the Landau level transitions are strongly diminished at high temperatures and almost disappear at room temperature.

The extinction of the spectral structures corresponding to the Landau level transitions in $\sigma_{xy}(\omega)$ with warming up is due to the simultaneous presence of electron and hole like Landau level transitions as seen in the graphs of $\sigma_+(\omega)$ and $\sigma_-(\omega)$, plotted in Fig. 6.4c and 6.4d. The separate Landau level transitions are not much affected by

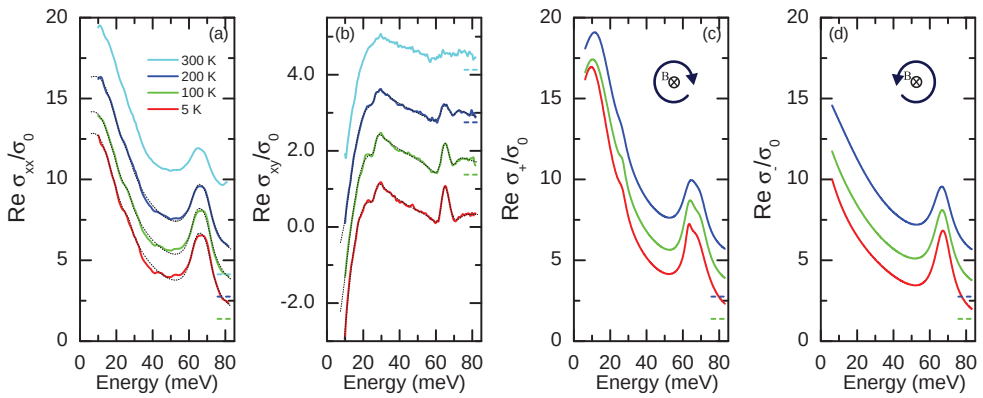

Figure 6.4: Magneto-optical conductivity of 6 layer graphene at 3 T, normalized to the universal conductivity σ_0, for several temperatures between 5 K and 300 K. The curves in all panels are offset as indicated by the dashed lines. Larger offsets correspond to higher temperatures. Panels (a) and (b) show the measured spectra of $\sigma_{xx}(\omega)$ and $\sigma_{xy}(\omega)$ (solid lines) and multi-component fits (black dotted lines, only at 5, 100 and 200 K). In panels (c) and (d) the model-derived $\sigma_+(\omega)$ and $\sigma_-(\omega)$ are shown.

temperature, but at high temperatures, the electron- and hole- like components that have slightly different Fermi velocities overlap more, due to the increased broadening. In $\sigma_{xy}(\omega)$ the contributions are subtractive and more overlap results in weaker spectral structures. On the other hand, in $\sigma_{xx}(\omega)$, which is unsensitive to the sign of the charge carriers, the contributions are additive and the transition peak appears less affected.

6.4 Results on 17 layer graphene

Similar to the magneto-optical measurements on the 6 layer graphene sample, we performed transmission and Faraday rotation measurements on 17 layer epitaxial graphene for fields up to 7 T and at a fixed temperature of 5 K. The real parts of the diagonal, $\sigma_{xx}(\omega)$, and Hall, $\sigma_{xy}(\omega)$, optical conductivities were obtained from the transmission and Faraday rotation spectra by using the general thin-film approximation, taking internal reflections in the substrate into account (see sections 2.3.1 and 2.3.3). As for the 6 layer sample, we used the linear thin film approximation, eqn. (2.49). Importantly, when measuring the transmission spectra, this time we did not reduce the spectral resolution in order to suppress the Fabry-Perot interference in the substrate, instead we used the best resolution to obtain the full interference spectra.

We locally fitted every inverse Fabry-Perot oscillation in the high resolution transmission spectra with a sine function. From the local fit we obtained the average transmission spectra without interference, which can be used to extract the real part of $\sigma_{xx}(\omega)$. Additionally, the fit to the interference fringes provides experimental access to the imaginary part of $\sigma_{xx}(\omega)$, as is described in section 2.3.2. The real parts of the obtained magneto-optical conductivities are plotted in Fig. 6.5a ($\mathrm{Re}\,\sigma_{xx}(\omega)$) and b

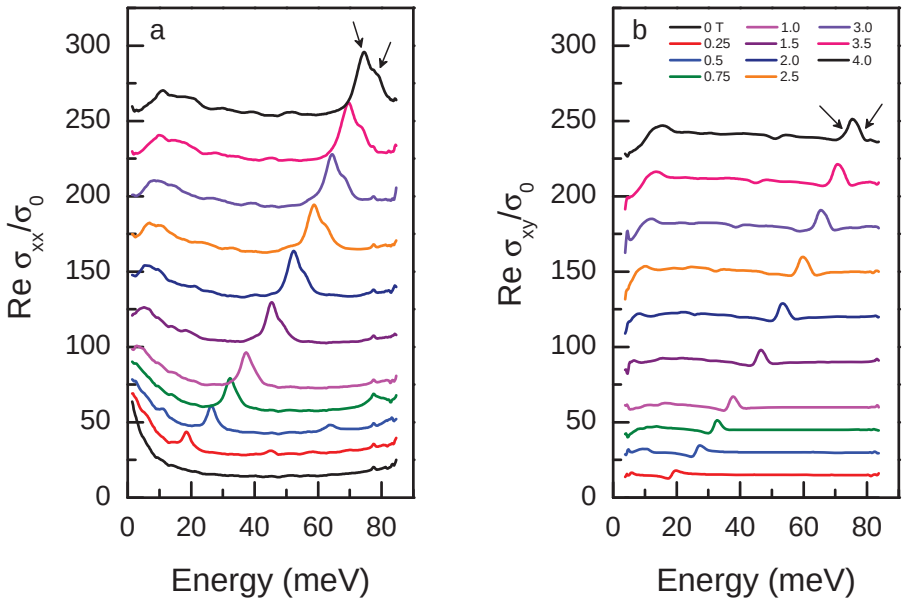

Figure 6.5: 17 layer epitaxial graphene: the real parts of the diagonal (a) and Hall (b) optical conductivity, normalized to the universal conductivity σ_0 at 5 K for fields up to 4 T, measured at 5 K. In (a) the arrows highlight the multi component character of the Landau level transition. In (b) the arrows point out the two inflections points with opposite slope. All curves are offset for clarity, with an offset of $60\sigma_0$ per Tesla.

(Re $\sigma_{xy}(\omega)$), for fields up to 4 T, at which the $\mathrm{LL}_{0\to1}$ and $\mathrm{LL}_{-1\to0}$ transitions are still fully resolved.

The real part of the diagonal conductivity, shown in Fig. 6.5a, clearly reveals quasi-classical cyclotron resonance at the low energies. Additionally, individual Landau level transitions, with a square-root dependence on field, are observed at the higher energies. Similar to the Landau level transitions seen in the 6 layer graphene sample, the structure in $\sigma_{xx}(\omega)$ consists of multiple peaks, most clearly seen at the high magnetic fields (as is pointed out by the arrows at 4 T). The multi component character of the Landau level transitions can also be seen from the Hall conductivity, shown in Fig. 6.5b: one can clearly see a structure with two inflections points (see the arrows at 4 T), indicating at least two Landau level transitions with opposite sign of the charge carriers and different Fermi velocity.

The imaginary part of the diagonal conductivity obtained from the interference analysis are plotted as the difference spectra between finite magnetic field and zero field, Im $(\sigma_{xx}(\omega, B) - \sigma_{xx}(\omega, 0))$, in Fig. 6.6. The solid lines correspond to the experimentally obtained data, for fields up to 4 T, at a temperature of 5 K. The dashed lines are obtained by a direct Kramers-Kronig transformation of the spectra of Re $\sigma_{xx}(\omega)$ (see section 2.2.4). Clearly, the experimental spectra of Im $(\sigma_{xx}(\omega, B) - \sigma_{xx}(\omega, 0))$ obtained independently from Re $\sigma_{xx}(\omega)$ and the curves obtained via the Kramers-Kronig relations match very well. However, around the cyclotron resonance at low

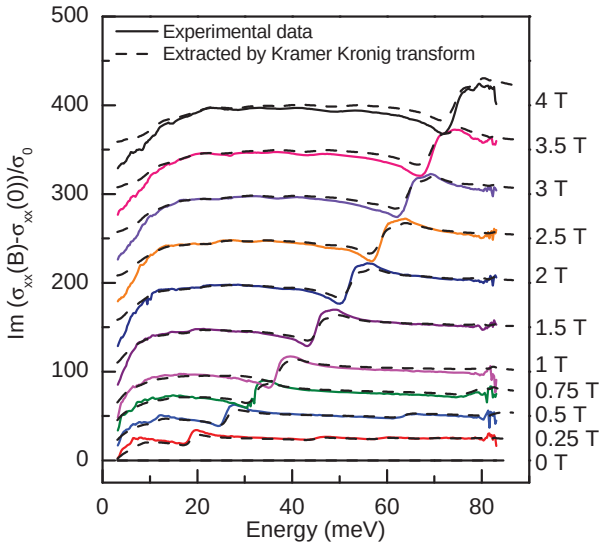

Figure 6.6: Spectra of the imaginary part of the diagonal conductivity, Im $(\sigma_{xx}(\omega, B) - \sigma_{xx}(\omega, 0))$, normalized to σ_0, of 17 layer epitaxial graphene. The solids lines are experimental spectra for fields op to 4 T, taken at 5 K, the dashed lines are obtained by Kramers-Kronig transformation of the real part of $\sigma_{xx}(\omega)$. All curves are offset for clarity, with an offset of $100\sigma_0$ per Tesla.

energies and at the structure corresponding to the Landau level excitations, the dashed lines show some deviations from the experimental spectra. This discrepancies could be caused by the extrapolation of Re $\sigma_{xx}(\omega)$ at the low and high energies, which can strongly affect the non-local Kramers-Kronig transformation. Therefore, whenever possible, an independent experimental determination of supplementing optical parameters such as transmission and interference fringes is highly beneficial for the complete extraction of the complex optical properties.

6.4.1 Basis of circular polarized light

To extract the magneto-optical conductivity in the circular basis, we followed a different approach than for the 6 layer graphene: instead of fitting the diagonal and Hall conductivity, we performed a direct Kramers-Kronig transformation (section 2.2.4) on the real part of the Hall conductivity to extract Im $\sigma_{xy}(\omega)$. With the use of eqn. (2.19) the conductivities in the basis of right- (revealing electron-like transitions) and left- (revealing hole-like transitions) handed circularly polarized light were found. $\sigma_+(\omega)$ and (b) $\sigma_-(\omega)$ are plotted in Fig. 6.7a and b, respectively.

In $\sigma_+(\omega)$ (Fig. 6.7a) both the cyclotron resonance, at low energy, and the $LL_{0\to1}$ transition at higher energies, are clearly present. Moreover, similarly to the 6 layer sample, the $LL_{0\to1}$ transition seems to consist of at least two components, which is most clearly seen at the high fields. However, in $\sigma_-(\omega)$ (Fig. 6.7b), in which the $LL_{-1\to0}$ transition can be observed, one can also see that the Landau level transition is

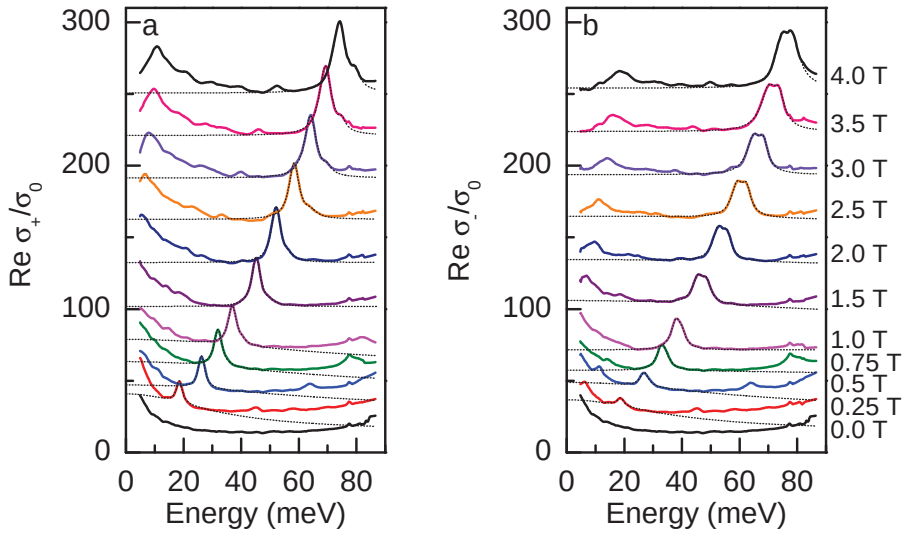

Figure 6.7: The magneto-optical conductivity in the basis of circular polarization of 17 layer graphene; with (a) $\sigma_+(\omega)$ and (b) $\sigma_-(\omega)$, normalized to the universal conductivity σ_0 at T = 5 K, for fields up to 4 T. The black dashed lines are fits to the $LL_{0\to1}$ (a) and $LL_{-1\to0}$ (b) transitions, using the Drude-Lorentz model for the magneto-optical conductivity. All curves are offset for clarity, with an offset of $60\sigma_0$ per Tesla.

clearly a superposition of at least two $LL_{-1\to0}$ transitions with different Fermi velocity. Whereas in the 6 layer graphene sample we observed only one single hole-like Landau level transition.

In order to analyze the multi component $LL_{0\to1}$ and $LL_{-1\to0}$ transitions, the magneto-optical conductivities were fitted in the region of those Landau levels using a multi component Drude-Lorentz model for the magneto-optical conductivity. We followed the same procedure as was detailed in section 6.3.1, with the exception that here we fitted $\sigma_+(\omega)$ and $\sigma_-(\omega)$ instead of $\sigma_{xx}(\omega)$ and $\sigma_{xy}(\omega)$. The fits to the Landau level transitions are shown in Fig. 6.7a and b as the black dashed lines. The results obtained from the fits are plotted in Fig. 6.11 and discussed in section 6.5.2.

6.5 Discussion

6.5.1 Cyclotron resonance transition and plasmonic resonance

The field dependence of fitting parameters associated with the quasi-classical cyclotron resonance observed in the 6 layer graphene sample are shown in Fig. 6.8. Like the cyclotron resonance observed in highly doped single layer graphene grown on the silicon face of SiC (see chapter 6.5.1), the energy of the cyclotron resonance is almost linear in field, as seen in Fig. 6.8a. However, at low fields a departure from the linear dependence can be seen, which is most likely due to the presence of plasmonic resonance.

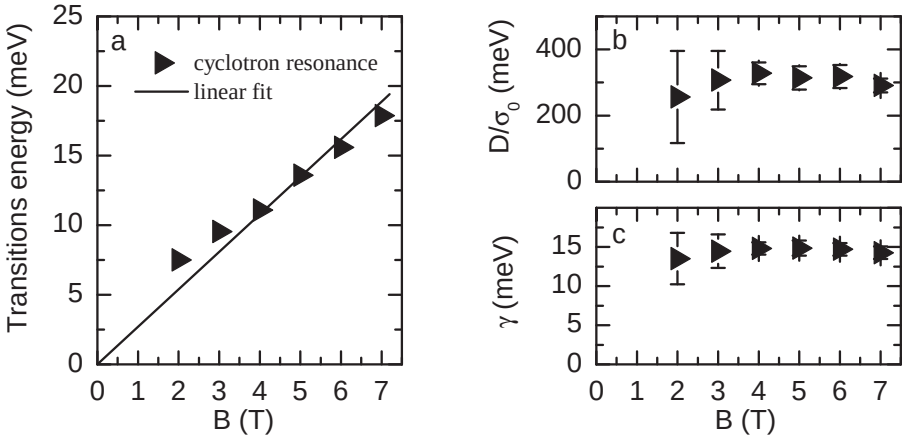

Figure 6.8: Parameters of the cyclotron resonance transition as a function of magnetic field obtained from the multi-component fits to $\sigma_{xx}(\omega)$ and $\sigma_{xy}(\omega)$ of Fig.6.3 (6 layer graphene). (a) The transition energies of the cyclotron resonance. The solid lines is a fit using eqn. (3.25). (b) Spectral weight of the cyclotron resonance peak. (c) The broadening of the cyclotron resonance transition. Errorbars in all figures are the standard deviation of several fitting results. The error bars in panel (a) are within the symbol size.

Note that the fitting was done with $\omega_0 = 0$. We will come back to plasmonic resonance in the end of this section.

The observation of cyclotron resonance in both the 6 layer and the 17 layer epitaxial graphene samples reveals a high doping in at least a part of the graphene layers. Like in single layer graphene, the Landau levels close to the Fermi energy have high index, so that when sweeping the magnetic field the transition energy follows a linear, instead of square-root, dependence on fields [30, 122]. In this case the cyclotron frequency is inversely proportional to the Fermi energy, as is see from eqn. (3.25). Using eqn. (3.25) and taking as an estimate $v_F = 1.0 \times 10^6$ m/s we obtain ϵ_F = 0.24 eV for this particular sample, which corresponds to a carrier concentration n $= \epsilon_F^2/\pi v_F^2\hbar^2 =$ 4.2×10^{12} cm^{-2}.

The spectral weight, D, of the cyclotron peak, shown in Fig. 6.8b, is field independent within the experimental accuracy. As was discussed in the previous chapter, in the absence of interactions, the Drude weight in a single graphene layer is related to ϵ_F: $\frac{\hbar D}{\sigma_0} = 2|\epsilon_F|$ (eqn. (5.2)). This provides ϵ_F = 0.16 eV and accordingly $n = 1.9\times$ 10^{12} cm^{-2}, which are significantly smaller than the values based on the linear dependence of the cyclotron frequency. Possibly, interactions renormalize the Drude weight and spread the missing weight over a large spectral range. In our fits this missing weight might be 'absorbed' by the broad background component mentioned above. On the other hand, we obtain a reduced Drude weight based on the assumption that for the bottom layer $v_F = 1.0 \times 10^6$ m/s. A smaller Fermi velocity (by about 20%) would make the cyclotron resonance and the Drude weight match according to eqn. (5.2) and eqn. (3.25).

The scattering rate, γ, (Fig. 6.8c) of the cyclotron peak is field independent and equal to about 14 meV. Using the semi-classical relation:

$$\mu = \frac{|\omega_c|}{\gamma|B|}, \tag{6.1}$$

we find a mobility of about 2000 cm^2/Vs, based on the experimental values of the scattering rate and the cyclotron frequency. Magneto-transport measurements show that the carrier density and mobility in multilayer graphene are correlated [178]. The values of n and μ that we obtain here for the cyclotron resonance fall on the generic dependence found in Ref. [178].

As mentioned above, the magnetic field dependence of the energy of the cyclotron resonance hints at the presence of plasmonic resonance in multilayer graphene grown on the carbon side of SiC. In chapter , the plasmon in single layer graphene was revealed by polarization dependent THz transmission spectroscopy, showing a clear absorption peak at finite energy, while the energy of the absorption peak was clearly correlated with the polarizer angle (section 4.3.2). Grain boundaries in the graphene layer were visualized using AFM topography images, and it was found that the polarization dependence of the plasmon energy matches the anisotropy revealed by the AFM maps. Unfortunately, AFM topography images made on multilayer graphene only reveal grain boundaries in the top most layer, but not the structure of the lowest graphene layer giving rise to the cyclotron resonance.

However, polarization dependent THz transmission measurements performed on the 6 layer graphene sample do indeed reveal an absorption peak at finite energy, as can be seen in Fig. 6.9. Two observations can be made: (i) the spectra are strongly polarization dependent and (ii) there is a transmission dip (absorption peak) between 3 and 5 meV depending on the polarization. Therefore this sample also shows a clear deviation from the Drude behavior at low enough frequencies, similar to graphene on the silicon face of SiC. The absorption peak is observed at somewhat lower energy than the plasmon resonance found in Si-face monolayer graphene. This peak might have a similar plasmon origin as in the case of monolayer graphene, however, the presence of many layers with different doping levels makes it difficult to tell from which layer this absorption peak is originating. Thus we cannot unambiguously conclude on its origin.

6.5.2 Landau level transitions

Next we discuss the field dependence of the lowest-index Landau level transitions in 6 layer graphene: the electron-like $\mathrm{LL}_{0\to1,a}$, $\mathrm{LL}_{0\to1,b}$ and the hole-like $\mathrm{LL}_{-1\to0}$. From $\sigma_+(\omega)$ and $\sigma_-(\omega)$, see Fig. 4.8, it is particularly evident that the two electron like and the hole like resonances have a similar magnetic field dependence. The energies of these Landau level transitions, shown in Fig. 6.10a, clearly follow the square-root dependence on magnetic field typical of massless Dirac fermions (eqn. (3.22)),

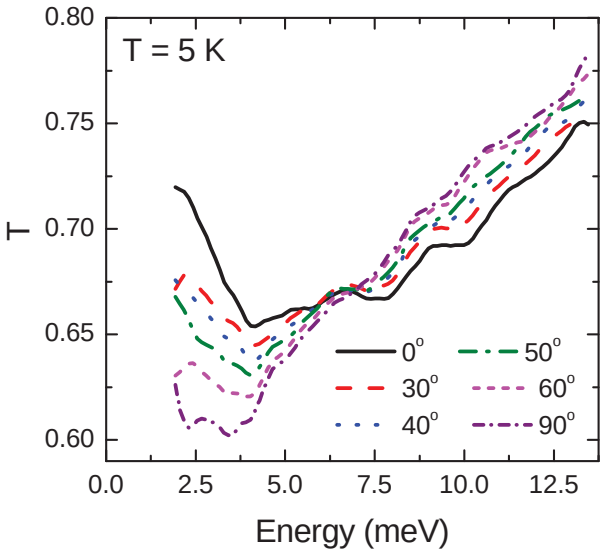

Figure 6.9: Terahertz transmission of 6 layer graphene on the C face of SiC for different polarizations at 5 K and 0 T. The zero position of the polarizer is chosen randomly.

in accordance with previous observations in similar epitaxial graphene samples [53] and exfoliated monolayer flakes [54, 55]. From $\sigma_+(\omega)$ and $\sigma_-(\omega)$ obtained on the 17 layer graphene, similar conclusions can be drawn. It is clear that the two electron like and two hole like resonances follow the typical square-root dependence on magnetic field (Fig. 6.7). The energies of all the low-index Landau level transitions observed in 17 layer graphene, namely $\mathrm{LL}_{0\to1,a}$, $\mathrm{LL}_{0\to1,b}$, $\mathrm{LL}_{-1\to0,a}$ and $\mathrm{LL}_{-1\to0,b}$, are shown in Fig. 6.11a and b.

Fitting the field dependence of the Landau level transition energies using eqn. (3.22) provides the Fermi velocities listed in Table 6.1; for both samples, they show a spread of about 10%. The difference between the Fermi velocities found from the electron like $\mathrm{LL}_{0\to1}$ and hole like $\mathrm{LL}_{-1\to0}$ transitions is only about 2%. However, the presence of multiple distinct inflection points in $\sigma_{xy}(\omega)$ corresponding to the energies of the Landau level transitions, is a clear sign that the transition energies and therefore the Fermi velocities are different.

6 layer graphene		17 layer graphene	
Transition	v_F (m/s)	Transition	v_F (m/s)
$\mathrm{LL}_{0\to1,a}$	1.02×10^6	$\mathrm{LL}_{0\to1,a}$	1.02×10^6
$\mathrm{LL}_{0\to1,b}$	1.11×10^6	$\mathrm{LL}_{0\to1,b}$	1.10×10^6
$\mathrm{LL}_{-1\to0}$	1.09×10^6	$\mathrm{LL}_{-1\to0,a}$	1.03×10^6
$\mathrm{LL}_{1\to2}$	1.01×10^6	$\mathrm{LL}_{-1\to0,b}$	1.09×10^6

Table 6.1: Fermi velocities found for different Landau level transitions in 6 layer and 17 layer graphene samples.

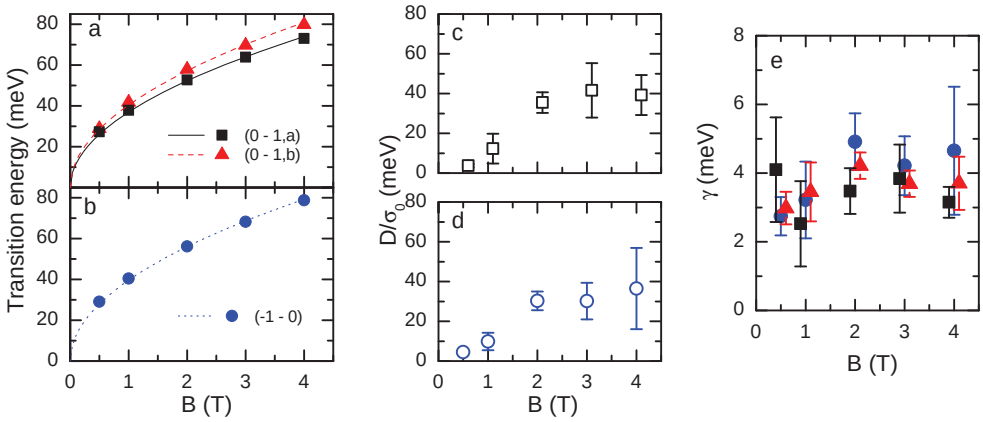

Figure 6.10: Parameters of various Landau level transitions as a function of magnetic field obtained from the multi-component fits to $\sigma_{xx}(\omega)$ and $\sigma_{xy}(\omega)$ shown in Fig.6.3 (6 layer graphene). (a) The transition energies of the $LL_{0\to1,a}$ (squares) and the $LL_{0\to1,b}$ (triangles) transitions. The lines are a fit using eqn. (3.22). (b) The transition energies of the hole-like $LL_{-1\to0}$ transition. The line is a fit using eqn. (3.22). (c) The sum of the spectral weights of the $LL_{0\to1,a}$ and the $LL_{0\to1,b}$ transitions. (d) Spectral weight of the $LL_{-1\to0}$ (circles) transition peaks. (e) The corresponding broadening of all the Landau level transitions. In (e) the colors and shapes of the dots correspond to the legend in (a) and (b). The errorbars in all figures are the standard deviation of several fitting results. The error bars in panel (a) are within the symbol size.

The spectral weights of the lowest-index Landau level transitions, plotted in Figs. 6.10c and d for 6 layer graphene (obtained by fitting σ_{xx}) and shown in Fig. 6.11c and d for 17 layer graphene (obtained by fitting σ_+ and σ_-), increase with magnetic field. Their magnetic field dependence is in qualitative agreement with an increase of the number of states within each Landau level with magnetic field [53, 127]. Consistently, the spectral weights observed in the 17 layer graphene is larger than the ones observed in 6 layer graphene. However, a closer look at the absolute values of the spectral weights reveals a strong reduction with respect to the theoretical expectation for ideal graphene monolayers, this will be discussed in more detail in the next section (section 6.5.3).

For both samples, the broadening of the Landau level transitions is about 2 to 4 meV and magnetic field independent (Fig. 6.10e and Fig. 6.11e).

6.5.3 Anomalous spectral weight of the Landau level transitions

Since only transitions between occupied and empty levels are allowed, the simultaneous presence of 0→1 and 1→2 transitions and the low-frequency cyclotron structure in multilayer graphene arises from a variation of the Fermi energy across different layers. The layer closest to the substrate is highly doped [73]; the doping in subsequent layers decreases exponentially with layer number. The most strongly doped innermost layer gives rise to cyclotron resonance, as in single layer graphene on the silicon terminated

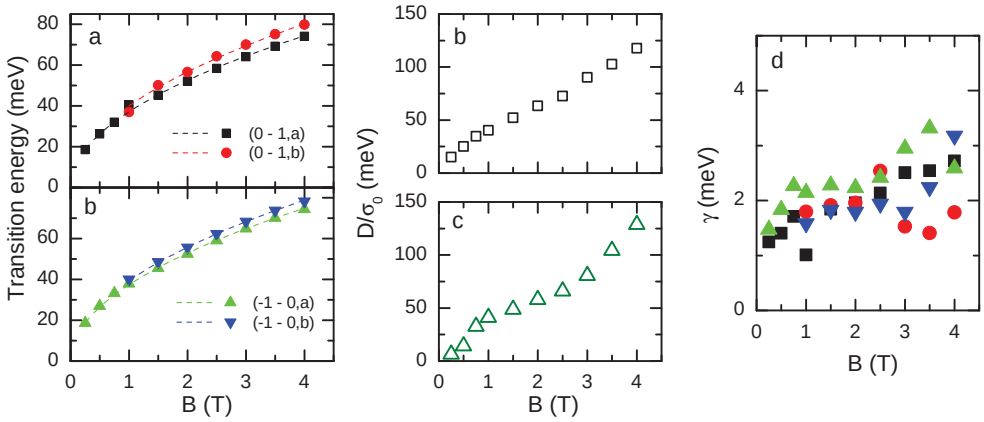

Figure 6.11: Parameters of various Landau level transitions as a function of magnetic field obtained from the multi-component fits to $\sigma_+(\omega)$ and $\sigma_-(\omega)$ shown in Fig.6.7 (17 layer graphene). (a) The transition energies of the electron-like $LL_{0\to1,a}$ (squares), $LL_{0\to1,b}$ (circles) transitions. (b) The transition energies of the hole-like $LL_{-1\to0,a}$ (triangles) and $LL_{-1\to0,b}$ (triangles down) transitions. The solid lines in (a) and (b) are fits using eqn. (3.22). (c) Sum of the spectral weights of the electron-like $LL_{0\to1,a}$ and $LL_{0\to1,b}$ transition peaks. (d) Sum of the spectral weights of the hole-like $LL_{-1\to0,a}$ and $LL_{-1\to0,b}$ transitions. (e) The broadening of the four Landau level transitions. In (e) the colors and shapes of the dots correspond to the legend in (a) and (b).

side of SiC. Meanwhile, the individual inter-LL transitions originate from the weakly doped layers, which are in the quantum regime, as can be seen from the square-root dependence of the transition energies on magnetic field. Note that the activation of different Landau level transitions may also be caused by a spatial doping inhomogeneity.

The maximum Faraday angle for multilayer epitaxial graphene on the carbon side of SiC is smaller than in the monolayer epitaxial graphene on the silicon side of SiC, because the innermost layer in multilayer graphene is weaker doped than the hydrogen intercalated graphene layer on the silicon terminated side of SiC.

The nearly perfect square-root dependence of the LL transition energies on magnetic field found in previous work [53, 159] and confirmed by the present measurements (Fig. 6.3a and Fig. 6.4a) is a signature of massless Dirac dispersion inherent to monolayer graphene. The same field dependence of the Landau levels is obtained by STM [57, 82]. Accordingly, ARPES measurements [85] show multiple Dirac cones from individual layers. As a result of these observations, multilayer graphene on the C-side of SiC is often regarded as a stack of twisted monolayers, electronically decoupled from each other due to random rotational stacking. However, some of our observations is difficult to fit into a simple picture of completely isolated monolayers. One of them is a significant (about 10%) spread of the Fermi velocity in the same sample. This issue we will discuss in more detail in section 6.5.4.

It is important to compare not only the energies but also the optical spectral weights D of the Landau level transitions with theoretical expectations [127, 131]. Experi-

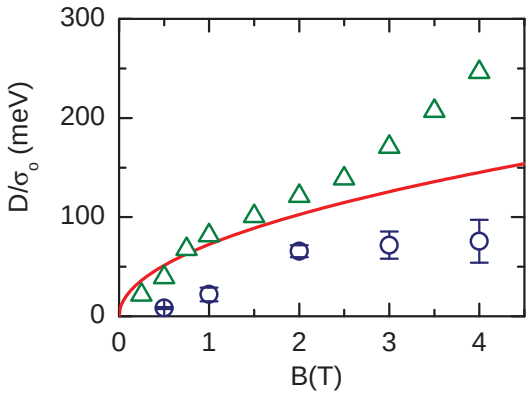

Figure 6.12: Total spectral weight of the $LL_{0\to1}$ and $LL_{-1\to0}$ transitions observed in 6 layer graphene (open circles) and the sum of the spectral weights of the $LL_{0\to1}$ and $LL_{-1\to0}$ transitions observed in 17 layer graphene (open triangles). The solid line is the theoretical prediction for the spectral weight of ideal monolayer graphene with the chemical potential between E_{-1} and E_1.

mentally, we obtain the weights from the multi-component spectra fitting, described in section 6.3.1. Let us consider the spectral weights of only the $LL_{0\to1}$ and $LL_{-1\to0}$ transitions. Assuming that the Fermi energy is between the first electron and hole Landau levels (E_{-1} and E_1), the total weight of these transitions in one single layer of graphene is given, according to the Kubo formalism for non-interacting Dirac fermions, by the transition energy itself [127]:

$$\hbar D/\sigma_0 = 2(E_1 - E_0) = 2\sqrt{2e\hbar v_F^2|B|} \tag{6.2}$$

This dependence on magnetic field for v_F = 1.0 $\times$ 10^6 m/s is plotted in Fig. 6.12 as a solid line. The symbols in Fig. 6.12 show the sum of the experimental spectral weights of the electron-like $LL_{0\to1}$ and hole-like $LL_{-1\to0}$ transitions, where the circles correspond to the total spectral weight observed for 6 layer graphene and the triangles to that observed in 17 layer graphene.

The total spectral weight observed in the low index LL transitions of the 6 layer sample is about two times smaller than the theoretical expectation for only a single graphene layer with its chemical potential is between E_{-1} and E_1. In reality it is likely that the number of layers in the 6 layer graphene sample that satisfy the condition for the chemical potential is larger, which would make the deviation even stronger. Similarly, the total spectral weight observed for the 17 layer sample is about equal to the theoretical expectation for a single graphene layer with its chemical potential is between E_{-1} and E_1. As sample has about 17 graphene layers, one would expect the largest part (at least more than half of the layers) to have its chemical potential between E_{-1} and E_1. Therefore also for this sample a considerable part of the spectral weight seems to be 'missing' from the $LL_{0\to1}$ and $LL_{-1\to0}$ transitions. At magnetic fields

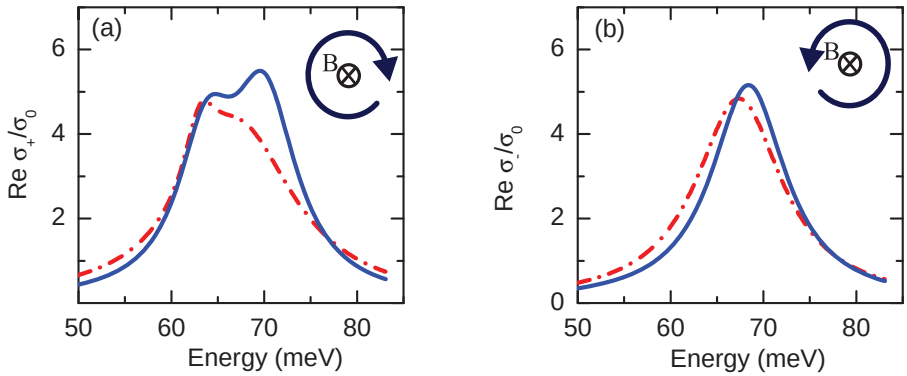

Figure 6.13: The effect of environmental doping on the Landau level transitions at B = 3 T and T = 5 K for 6 layer graphene. (a) The contributions of the $\mathrm{LL}_{0\to1,a}$ and $\mathrm{LL}_{0\to1,b}$ transitions to $\sigma_+(\omega)$. (b) The contribution of the $\mathrm{LL}_{-1\to0}$ transition to $\sigma_-(\omega)$. In both (a) and (b), the red dash-dotted lines correspond to the measurement series as a function of temperature at constant magnetic field (Fig. 6.4), while the blue solid lines correspond to the measurement series as a function of magnetic field at constant temperature (Fig. 6.3). The curves are derived from the multi-component fits of the experimental data.

above 2 T, the total spectral weight is increasing more rapidly than expected, which might be due to the fact that parts of the graphene with high doping start to contributed to the $\mathrm{LL}_{0\to1}$ and $\mathrm{LL}_{-1\to0}$ transitions.

Possibly related to the 'missing' spectral weight in the lowest index Landau level transitions is the presence of the optical absorption background found from the fitting results of the phenomenological cyclotron multi-component model, see section 6.3.1. This component has a substantial spectral weight spread over a broad frequency range. The existence of the background shows that a significant amount of the charge carriers in the graphene layers neither fall into well defined CR nor LL transitions and signals a departure from the isolated monolayer description. In terms of the optical sum rule, the missing spectral weight of the LL transitions is transferred to the background. An intriguing question is whether this transfer is caused by interlayer coupling or by many-body effects within individual layers, such as electron-electron and electron-phonon interactions.

One should notice that the mobility and density of carriers in epitaxial graphene show a large variation from sample to sample, even when they are prepared under similar conditions [178]. This shows that the interlayer twist angle, which is at the moment difficult to control experimentally, is a crucial parameter affecting the electronic and therefore optical properties of epitaxial graphene.

6.5.4 Effects of environmental doping

In the case of the 6 layer graphene sample, two separate measurement series were performed. Within each measurement series, the optical absorption and the Faraday

rotation were measured one after another with a shortest possible delay. During the experiments the sample was in a He gas flow; between the production and the experiments, as well as between the first and second series, it was stored in desiccated air.

A careful inspection of the two series of measurements (Figs. 6.3 and 6.4) shows that the spectra from the different series taken at the same experimental conditions (5 K and 3 T) are not precisely the same, especially close to the $LL_{0\to1,a}$, $LL_{0\to1,b}$ and $LL_{-1\to0}$ transition energies. It is reasonable to assume that the difference is due to the effect of the environmental molecular contamination [77]. In the case of multilayer graphene, the electronic properties of the outmost layer are most strongly modified, although one cannot exclude a certain effect on inner layers as well. Due to this surface contaminations, the data presented in this chapter, which were published in Ref. [168] differ somewhat from data presented in Ref. [138], although the same sample was used.

Fig. 6.13a shows the contributions of the $LL_{0\to1,a}$ and $LL_{0\to1,b}$ transitions to $\sigma_+(\omega)$, for both measurements at 5 K and 3 T. The low energy $LL_{0\to1,a}$ transition with v_F = 1.02 $\times$ 10^6 m/s is unaltered by the surface contamination. However, the high energy $LL_{0\to1,b}$ transition with v_F = 1.11 $\times$ 10^6 m/s shows a clear change: the structure is much sharper in the second measurement (blue line). In Fig. 6.13b the contribution of the $LL_{-1\to0}$ transition to $\sigma_-(\omega)$ is plotted for both measurements. Similar to $LL_{0\to1,b}$, it shows a sharpening in the second measurement (blue line). The fact that both $LL_{0\to1,b}$ and $LL_{-1\to0}$ transition peaks are changed with environmental doping suggests that these transitions originate from the bands in the outmost graphene layer, which is most affected by surface contamination. The $LL_{0\to1,a}$ transition with the lowest v_F is unchanged by the environmental doping, therefore it might come from deeper graphene layers. Thus we attribute the largest values v_F = 1.09 - 1.11 $\times$ 10^6 m/s to the outmost graphene layer, while the smallest values, v_F = 1.01 - 1.02 $\times$ 10^6 m/s, correspond to the inner layers, where the transitions $LL_{0\to1,a}$ and $LL_{1\to2}$ are active due to a weak electron doping. It was theoretically predicted [88, 90, 91] that in rotationally stacked graphene layers the effect of the interlayer interaction is to reduce the Fermi velocity with respect to its 'bare' value in monolayer graphene. The variation of v_F between the outer and inner layers can thus be attributed to the effect of layer twisting and a randomness of the rotation angles between various layers.

From Fig. 6.10c one can see that the spectral weights of the electron-like $LL_{0\to1,b}$ and the hole-like $LL_{-1\to0}$ transitions are approximately equal, which indicates a balance between electrons and holes in the top layer. The Fermi velocity of the electrons (1.11 $\times$ 10^6 m/s) in that layer is slightly larger than the one of the holes (1.09 $\times$ 10^6 m/s). Similar results were found for exfoliated monolayer graphene [55] and few layer CVD graphene [95] graphene.

The asymmetry between electrons and holes was experimentally shown to depend on the relative rotation between subsequent graphene layers [95], where a large (small) rotation between the layers gives a small (large) asymmetry. The electron-hole asymmetry found in both the 6 and the 17 layer graphene samples (about 2%) is much

smaller than the one found in Ref. [95], which might be due to different rotation angles between the layers in the used samples.

6.6 Conclusions

In conclusion, we used magneto-optical infrared Hall spectroscopy to study the charge dynamics in multilayer epitaxial graphene grown on the C-side of SiC in magnetic fields up to 7 T. Two samples were studies, one with 6 layers of graphene and the other with about 17 layers of graphene. The diagonal and the Hall conductivities were extracted from the absorption and the Faraday rotation spectra, respectively. The latter is sensitive to the sign of charge carriers that allowed us to distinguish electrons and hole-like transitions. For the 6 layer graphene, the mobility and charge density of electrons were found from the quasi-classical cyclotron resonance, which makes this technique a useful contactless characterization tool.

The spectra of the 6 layer sample were fitted using a multi-component model, eqn. (2.27) and eqn. (2.28), which provided excellent fits at each field to $\sigma_{xx}(\omega)$ and $\sigma_{xy}(\omega)$ simultaneously. This analysis revealed the coexistence of optical transitions between individual Landau levels with a square-root dependence of the transition energies on magnetic field as expected for isolated monolayer graphene and a quasi-classical cyclotron resonance showing a linear magnetic field dependence. The observation of both cyclotron resonance and individual Landau level transitions is a clear indication of the doping variation across the layers.

For the 17 layer sample, $\sigma_+(\omega)$ and $\sigma_-(\omega)$ were extracted by direct Kramers-Kronig transformation of the data. Similarly to the 6 layer sample, the magneto-optical conductivity revealed the coexistence of transitions between individual Landau levels with a square-root dependence of the transition energies on magnetic field and an electron-like cyclotron resonance.

For both samples, we found the simultaneous presence of at least two distinct peaks due to electron-like transitions between Landau levels 0 and 1. The separation between these peaks corresponds to a difference between the Fermi velocities of about 10%. Also hole-like transitions between Landau level -1 and 0 are observed. The effect of the surface contamination on the spectra tells that both electrons and holes are present in the top layer and that the electrons have slightly higher Fermi velocity than the holes (by 2%). The variation of the Fermi velocity is probably related to random twisting angles between graphene layers.

The spectral weight of the Landau level transitions is shown to be significantly reduced with respect to the theoretical expectation for a stack of fully decoupled graphene monolayers, assuming the picture of non-interacting electrons within each layer. This absence of spectral weight was detected in both the 6 and the 17 layer graphene sample. This missing spectral weight correlates with the presence of an unexpected broadband optical absorption, which is also inconsistent with this simplified theoretical model.

Although the transition energies of the Landau level transitions clearly follow the magnetic field dependence expected for isolated graphene, in order to come to a complete picture of the complex electronic structure of multilayer graphene we need to understand the variation of the Fermi velocity, and most importantly the small optical spectral weight of the Landau level transition and the broad absorption background in relation to the twist angle of the layers. Therefore, a systematic study of samples where this angle is experimentally controlled, is required.

6. MULTI-COMPONENT OPTICAL CONDUCTIVITY IN MULTILAYER GRAPHENE

Conventions

A.1 Summary of symbols and short-hand notations

Table (2) summarizes the short-hand notations used in the main text and sums up the meaning of symbols used.

Notation	Explanation	
T	substrate normalized transmission	or Temperature
B	magnetic field	
θ	Faraday rotation angle	
LL	Landau level	
n	Landau level number	or carrier density
m	Landau level number (only in chapter 5)	
E_n	Landau level energy	eqn. (3.22)
$\mathrm{LL}_{n\to n+1}$	Transition between electron like LLs	
$\mathrm{LL}_{-n-1\to -n}$	Transition between hole like LLs	
ω_c	Low doping: energy of the LL transition	$\omega_c = \lvert E_{n+1(-n)}\rvert - \lvert E_{n(-n-1)}\rvert$
	High doping: quasi-classical cyclotron resonance energy	eqn. (3.25)
v_F	Fermi velocity	
ϵ_F	Fermi energy	
m_c	cyclotron mass	
α	fine structure constant	
MIR	mid infrared	
FIR	far infrared	
THz	terahertz	
ARPES	Angle-Resolve Photoemission Spectroscopy	
XPS	X-ray Photoemission Spectroscopy	
AFM	Atomic Force Microscopy	
RCPL	Right handed circular polarized light	
LCPL	Left handed circular polarized light	
SiC(0001)	silicon terminated silicon carbide	
SiC($000\bar{1}$)	carbon terminated SiC	

Table 2: Clarification of the short-hand notations and symbols used in the discussions.

Appendices

B.1 Numerical check of the thin film relation for $\mathrm{Re}[\sigma_{xx}]$

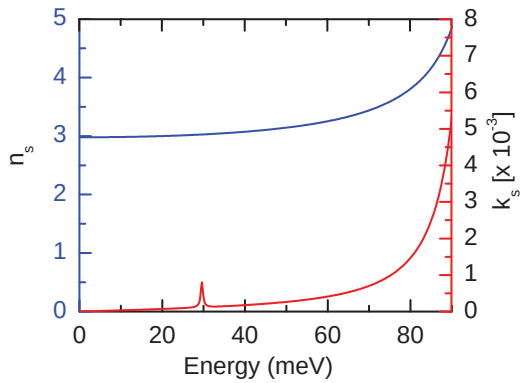

Figure 14: Refractive index, n_s, and extinction coefficient, k_s, of the SiC substrate, used in the multilayer model.

In the derivation of eqn. (2.47) we rely on the thin film approximation and, at zero magnetic field, neglect the imaginary part of σ_{xx}. At finite magnetic fields, the approximation becomes more severe by ignoring the influence of σ_{xy} on the transmission ratio. In order to estimate the difference between the exact optical conductivity and the one obtained from eqn. (2.47), here we introduce an exact optical model for a thick substrate and thin film. The model directly provides the exact optical conductivity of the thin film and with the use of the Fresnel equations the substrate normalized transmission T is found exactly. The exact transmission ratio T is used as an input for eqn. (2.47), from which the approximative thin film conductivity is obtained. The exact and the approximative result are then compared. This comparison is made for both zero and finite externally applied magnetic fields.

To start with, the Lorentz model (eqn. (2.30)) is used to model the optical properties of SiC, used as the thick substrate. From the model, the refractive index, n_s and extinction coefficient, k_s, can be extracted, which are shown in Fig. 14. The thick-

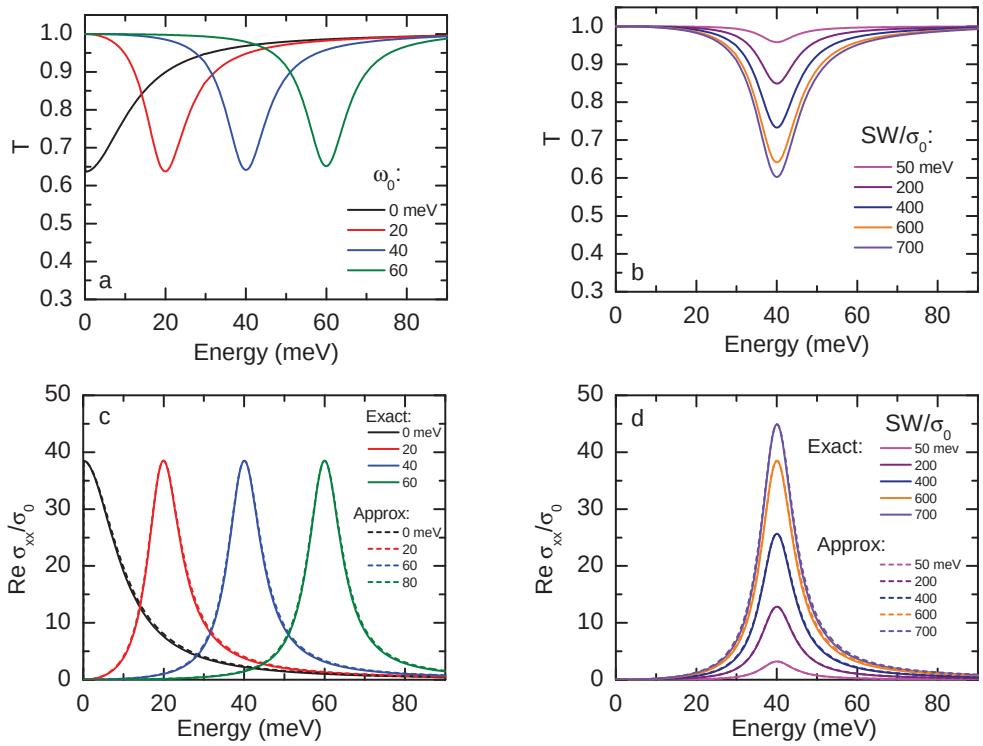

Figure 15: (a) $T = T_{f+s}/T_s$ for various peak positions and a constant weight of 600 meV, obtained from the model and used as input for eqn. (2.47). (b) $T = T_{f+s}/T_s$ for various weights and a fixed peak position of 40 meV, obtained from the model and used as input for eqn. (2.47). (c) The real part of the optical conductivity normalized to the universal conductivity $\sigma_0 = e^2/4\hbar$, for various peak positions. The solid curves are the exact model curves, the dashed lines are obtained from T shown in (a) using eqn. (2.47). (d) The real part of the optical conductivity for various peak weights, the solid curves are the exact model curves, the dashed lines are extracted using eqn. (2.47) and T shown in (b).

ness of the substrate was 360 μm. At zero field the optical properties of the thin film were modeled using one Lorentz oscillator (eqn. (2.30)) with ω_0 varied between 0 and 65 meV, the weight of the peak was varied between 0 and 700 meV and the broadening was fixed at γ = 10 meV. Next, we (use RefFit [179] to) solve the Fresnel equations for this model system and extract the transmission of the film on the substrate, T_f, the bare substrate, T_s to access $T = T_f/T_s$.

Figure 15a shows T for ω_0 = 0, 20, 40 and 60 meV, with fixed spectral weight (600 meV). In Fig. 15b T is shows for the peak weights of 50, 200, 400, 600 and 700 meV, with a fixed peak position (ω_0 = 40 meV). In Fig. 15c the results for $\mathrm{Re}[\sigma_{xx}/\sigma_0]$ are plotted for various ω_0, the solid line represents the exact conductivity, while the dashed line is the result obtained by eqn. (2.47). The positions and the shape of the peaks are accurately reproduced by the approximation. The results for varying spectral weight are shown in Fig. 15d.

To estimate the difference between the exact $\mathrm{Re}[\sigma_{xx}/\sigma_0]$ and result from eqn. (2.47)

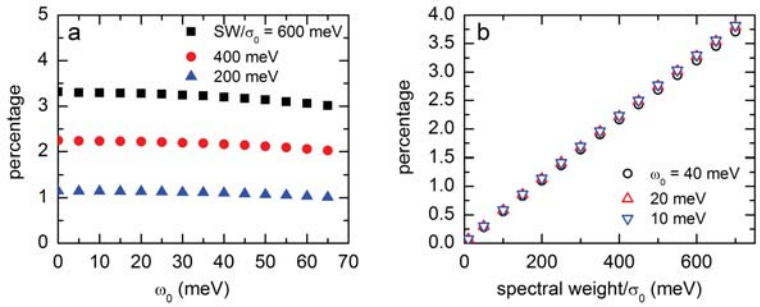

Figure 16: (a) Difference in the peak area from eqn. (2.47) with respect to the exact peak area in percentage for varying ω_0. (b) Difference in percentage for varying absorption strengths with a fixed peak position at ω_0 = 40 meV.

the area under the curve was integrated to obtain the spectral weight of the peak. Figure 16a shows the difference in area of eqn. (2.47) with respect to the exact area, as a function of ω_0, for a fixed peak intensity of 200, 400 and 600 meV. For all peak intensities the spectral weight is overestimated by eqn. (2.47) and almost independent of ω_0. In Fig. 16b, the deviation in the peak area is shown as a function of the weight of the peak in the exact model, for ω_0 = 10, 20 and 40 meV. It can be seen that the deviation indeed coincides for different ω_0. For small model peak intensities the spectral weight is clearly more accurately reproduced: at a spectral weight of 200 meV the overestimation is just a bit more than 1%. However, for a model peak intensity of 600 meV the deviation has increased to about 3%.

At finite magnetic field the approximation made is somewhat more prominent, due to the additional neglecting of σ_{xy}. Here we estimate the error made at finite magnetic fields. Firstly, the substrate + film model is expanded to include cyclotron resonance. For the model of the substrate the same parameters were used as above (see Fig. 14 for the substrate parameters). The optical properties of the thin film were modeled with a cyclotron resonance peak with ω_0 = 0 meV, ω_c was varied from 0 to 65 meV, the spectral weight was varied between 0 and 700 meV and γ = 10 meV.

Figure 17a shows T for ω_c = 0, 20, 40 and 60 meV, with a fixed spectral weight of 600 meV, while in Fig. 17b additional transmission spectra for the peak weights of 50, 200, 400, 600 and 700 meV, with a fixed cyclotron resonance energy (ω_c = 40 meV) are shown. Figure 17c shows $\mathrm{Re}[\sigma_{xx}/\sigma_0]$, plotted for various ω_c; the solid lines represent the exact solution, while the dashed lines are the results obtained from eqn. (2.47) and the transmission curves shown in (a). Like for zero magnetic field (Fig. 15), the positions of the peaks are accurately reproduced. On the contrary, the peak intensities are clearly underestimated by the approximation. The results for varying spectral weight, shown in Fig. 17c, show a similar underestimation of peak intensity.

The exact and approximated conductivity curves are integrated to estimate their deviation in the intensity of the peaks as a function of cyclotron resonance energy and absorption. Figure 18a shows the difference in peak intensity with respect to the exact intensity as a function of cyclotron resonance energy, for different exact

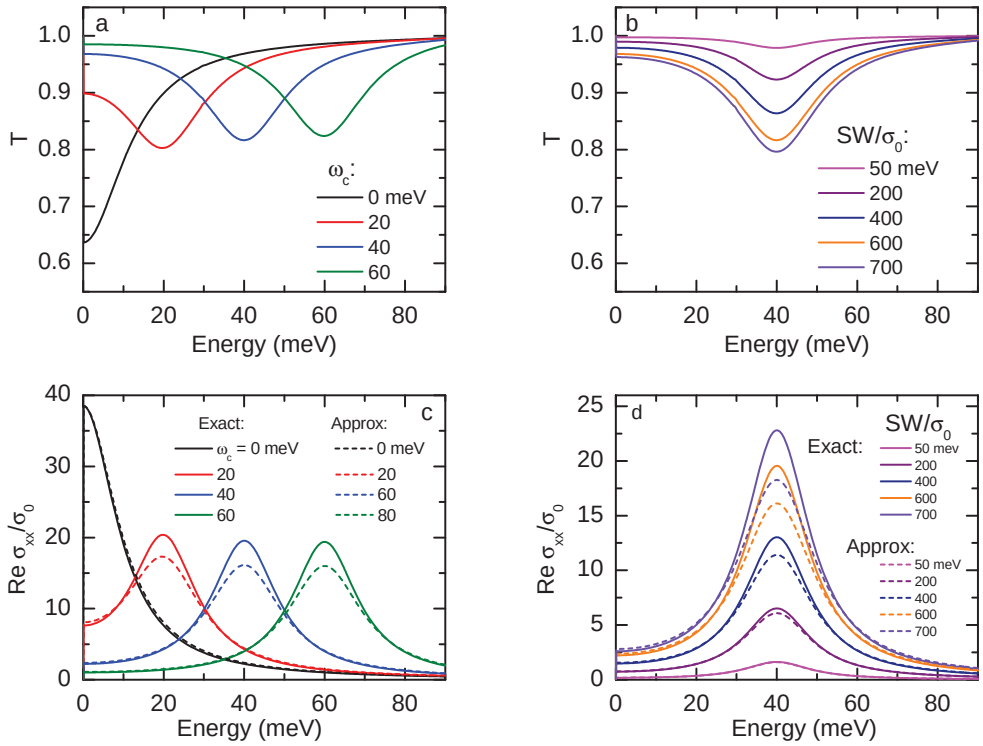

Figure 17: (a) $T = T_{f+s}/T_s$ for various magnetic fields and a constant peak intensity of 600 meV, obtained from the model and used as input for eqn. (2.47). (b) $T = T_{f+s}/T_s$ for a fixed magnetic field (ω_c = 40 meV) and various peak intensities, to be used as input for eqn. (2.47). (c) The real part of the optical conductivity normalized to the universal conductivity $\sigma_0 = e^2/4\hbar$, for various magnetic fields. The solid curves are the exact model curves, the dashed lines are obtained from the T spectra shown in (a) and eqn. (2.47). (d) The real part of the optical conductivity for various optical weights, the solid curves are the exact model curves, the dashed lines are obtained from the spectra shown in (b) and the approximation.

intensities 200, 400 and 600 meV. For all optical weights, eqn. (2.47) results in an overestimation of the optical spectral weight at small magnetic fields (small ω_c), as was also found for zero magnetic field (see Fig. 16a). However, with increasing ω_c the deviation due to neglecting σ_{xy} is growing and finally results in an underestimation of the optical spectral weight, which eventually saturates for high magnetic fields. The saturation value depends strongly on the weight of the cyclotron peak. In Fig. 18b the difference in peak intensities with respect to the exact intensity is plotted as a function of the model spectral weight, for ω_c = 10, 20 and 40 meV. For small peak weights the underestimation is small, however, the deviation grows steadily for larger absorption. This effect is most significant for higher cyclotron resonance energies. Therefore, the higher the magnetic field (is higher ω_c) and the larger the absorption, the more severe will be the error introduced by neglecting the influence of σ_{xy} on T.

In conclusion, the real part of the optical conductivity of a thin film on a sub-

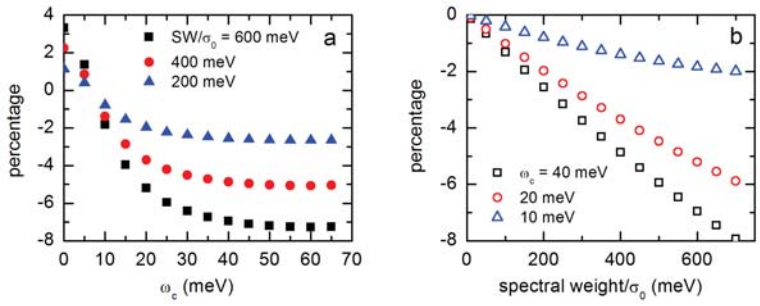

Figure 18: (a) Difference in percentage between the optical spectral weight of the conductivity extracted from the thin film approximation (eqn. (2.47)), compared to the exact optical weight, as a function of ω_c, for peak intensities of 200, 400 and 600 meV. (b) Difference in percentage between the approximative and exact optical spectral weight as a function of peak intensities, plotted for cyclotron resonance energies, $\omega_c = 10$, 20 and 40 meV.

strate can be extracted from the transmission ratio between film and substrate, when the complex refractive index and the thickness of the substrate are known. Equation (2.47) proves reasonably accurate, especially in reproducing the peak positions in the optical spectra. At zero or low magnetic fields the spectral weight will be slightly overestimated depending on the amount of absorption in the film. On the contrary, at higher magnetic fields, neglecting σ_{xy} result in an underestimation of the spectral weight, where the level of deviation strongly depends on the amount of absorption in the film and the cyclotron resonance energy.

B.2 Derivation of the thin film relation for $\mathrm{Im}[\sigma_{xx}]$

In section 2.3.2, the imaginary part of the optical conductivity is related to the period of Fabry Perot fringes in a spectrum. The shift in the period is linked to the conductivity of the film on top of the substrate, the condition for constructive interference then leads to the thin film approximation (eqn. (2.51)):

$$\Delta\mathrm{Im}\left(\frac{\sigma_{xx}}{\sigma_0}\right) = \frac{\xi}{\alpha}\frac{n_s^2-1}{n_s}, \tag{3}$$

where the ξ function is the shift of the Fabry-Perot period normalized to the period, α is the fine-structure constant and n_s is the real part of the refractive index of the substrate.

The condition for constructive interference is found from the phase:

$$\varphi = \frac{2\omega_M d_s N_s}{c} + \arg r_{sfv} = 2\pi M, \tag{4}$$

where ω_M are frequencies at which maxima (constructive interference) occurs (see Fig. 2.5b), d_s is the thickness of the substrate, N_s is the complex refractive index of the

substrate, r_{sfv} is the reflection coefficient of light reflecting from the substrate onto the film back to the substrate (see Fig. 2.1), and M is the integer number of the maximum. To obtain an expression for $\arg r_{sfv}$, the Fresnel relation for thin films is rewritten, using a linear approximation:

$$\begin{aligned} r_{sfv} &= \frac{N_s - 1 - Z_0\sigma_f}{N_s + 1 + Z_0\sigma_f} \\ &\approx \frac{N_s - 1}{N_s + 1}\left[1 - Z_0\sigma_f\left(\frac{1}{N_s - 1} + \frac{1}{N_s + 1}\right)\right] \\ &= \frac{N_s - 1}{N_s + 1} - Z_0\sigma_f\frac{2N_s}{(N_s + 1)^2}. \end{aligned} \tag{5}$$

To determine the argument of r_{sfv}, we use that $\arg r = \arctan[\frac{\mathrm{Im}r}{\mathrm{Re}r}] \approx \frac{\mathrm{Im}r}{\mathrm{Re}r}$, and neglect the real part of $Z_0\sigma_f$ in the second term of eqn. (5), which is valid for $Z_0\sigma_f \ll 1$.

$$\arg r_{sfv} \approx -\mathrm{Im}[Z_0\sigma_f]\frac{2N_s}{(N_s + 1)^2}\frac{N_s + 1}{N_s - 1} = -\mathrm{Im}[Z_0\sigma_f]\frac{2N_s}{N_s^2 - 1}. \tag{6}$$

The change in the interference condition with magnetic field is found by evaluating the field derivative:

$$\frac{2d_sN_s}{c}\frac{d\omega_M}{dB} + \frac{d}{dB}(\arg r_{sfv}) = 0, \tag{7}$$

and thus:

$$\frac{2d_sN_s}{c}\frac{d\omega_M}{dB} = Z_0\frac{2N_s}{N_s^2 - 1}\frac{d\mathrm{Im}[\sigma_f]}{dB}. \tag{8}$$

Assuming that the changes with field are small, we obtain:

$$\Delta\omega_M = \frac{cZ_0}{d_s}\frac{1}{N_s^2 - 1}\Delta\mathrm{Im}[\sigma_f]. \tag{9}$$

In order express the left hand side of eqn. (9) in terms of $\xi = \Delta\omega_M/\delta\omega_M$, the expression is divided by the period, $\delta\omega = \frac{\pi c}{d_sN_s}$ of the fringes:

$$\xi = \frac{\Delta\omega_M}{\delta\omega_M} = \frac{Z_0}{\pi}\frac{N_s}{N_s^2 - 1}\Delta\mathrm{Im}[\sigma_f]. \tag{10}$$

By substituting Z_0 with $4\pi/c$, expressing the conductivity of the film in terms of the universal conductivity, $\sigma_0 = e^2/4\hbar$ and introducing the fine-structure constant $\alpha = e^2/c\hbar$, eqn. (2.51) from section 2.3.2 is found.

B.3 Numerical check of the thin film relation for $\Delta\mathrm{Im}[\sigma_{xx}]$

In the derivation of eqn. (3) we rely on the thin film approximation, a linear approximation is utilized, the influence of σ_{xy} is neglected and we assume that the contribution

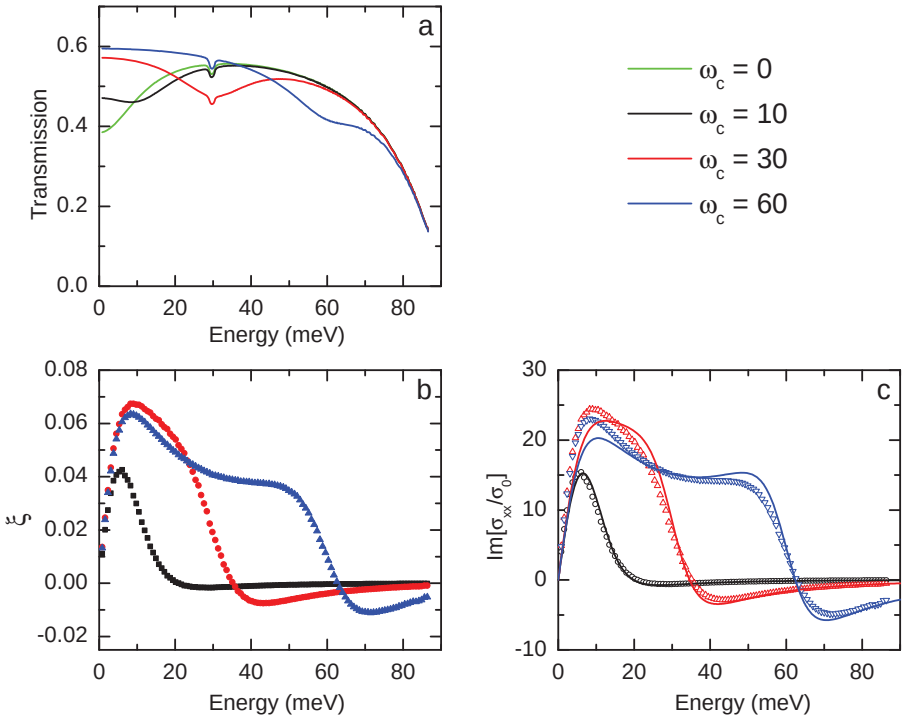

Figure 19: (a) Transmission of graphene on SiC with cyclotron resonance absorption at 0, 10, 30 and 60 meV, here the Fabry-Perot oscillations are unresolved. (b) ξ function for ω_c = 10, 30 and 60 meV. (c) $\Delta\mathrm{Im}[\sigma_{xx}]$ found from ξ for ω_c = 10, 30 and 60 meV, with respect to $\omega_c = 0$.

of $\mathrm{Re}[\sigma_{xx}]$ to the ratio $\frac{\mathrm{Im}r}{\mathrm{Re}r}$ is small enough to ignore. In this section we estimate the impact of these simplifications by comparing the exact optical conductivity, $\Delta\mathrm{Im}[\sigma_f]$, and the one obtained from eqn. (3), using the information of the Farbry-Perot oscillations in the transmission spectra.

The Lorentz model (eqn. (2.30)) is used to model the optical properties of SiC, used as the thick substrate. From the model, the refractive index, n_s can be extracted, which is shown in Fig. 15a. The thickness of the substrate was 360 μm. A Drude-Lorentz model with finite ω_c (eqn. (2.25)) was used to generate the magneto-optical conductivity of the thin film. The model directly provides the exact optical conductivity of the thin film and with the use of the Fresnel equations the transmission T of the film on the substrate is found. The substrate is treated as fully coherent, therefore Fabry-Perot oscillations dominate the transmission, an example can be seen in Fig. 2.5 (section 2.3.2). With the use of the fitting routine described in section 2.3.2, the Fabry-Perot fringes are fitted locally. From the fitting results the average transmission amplitude, the period of the fringes and the number of fringes as a function of energy are found. This procedure is followed for a number of different curves: the conductivity of the film is generated with varying cyclotron resonance energies (varied from 0 to 65 meV), while keeping the spectral weight of the resonance fixed at 600 meV. The broadening, γ, was

fixed to 10 meV.

Figure 19a shows the average transmission amplitude extracted from the fit to the Fabry-Perot oscillations for ω_c = 0, 10, 30 and 60 meV. At zero field a clear Drude response is recognized from the dip in the transmission centered around 0 meV. With increasing ω_c, the dip in the transmission shifts to higher energies. The small, stationary dip around 25 meV is caused by a weak phonon in the SiC substrate. At high energies the transmission is strongly decreased by a strong phonon in the SiC at around 100 meV. The average transmission extracted from the Fabry-Perot oscillations can be normalized to the transmission of bare SiC and subsequently serve as the input for eqn. (2.47) to extract $\mathrm{Re}[\sigma_f]$.

Figure 19b shows the ξ function for ω_c = 10, 30 and 60 meV, which serves as the input for eqn. (3) to obtain $\Delta\mathrm{Im}[\sigma_f]$, plotted in Fig. 19c as the open symbols. The solid lines in Fig. 19c correspond to the exact solution of $\Delta\mathrm{Im}[\sigma_f]$ which follows from the initial magneto-optical model.

Although $\Delta\mathrm{Im}[\sigma_f]$ extracted from the Fabry-Perot fringes shows some deviations from the exact result, the spectral features are very well reproduced. Even the absolute value is not significantly suppressed or enhanced. Keeping in mind that at the lower energies eqn. (3) generally results in an overestimate, while at the higher energies $\Delta\mathrm{Im}[\sigma_f]$ is underestimated, the experimentally obtained curves can be utilized, for example, to check the Kramers-Kronig consistency of difference data sets.

B.4 Maxwell-Garnett Approach

The effective medium approximation is a standard approach to calculate optical properties of inhomogeneous media. In the case of isolated quantum dots of a two dimensional electron gas, the Maxwell-Garnett effective medium model results in the following relation [146]:

$$\sigma_{\mathrm{eff}}(\omega) = \frac{f\,\sigma(\omega)}{1 + C\,i\sigma(\omega)/(d\omega\kappa)}. \tag{11}$$

Here $\sigma(\omega)$ is the intrinsic conductivity of the electron gas, $\kappa = (\epsilon_1 + \epsilon_2)/2$ is the average dielectric function of the surrounding media, f is the filling factor, d is the dot diameter and C is a geometrical parameter related to the depolarization factor of the dots. For the circular shape, the exact value for C is $3\pi^2/2$ [157, 160].

The optical conductivity of a homogeneous 2D electron gas or of highly doped graphene in magnetic field, assuming constant scattering, is given by:

$$\sigma_{\pm}(\omega) = \frac{ne^2}{m}\frac{i}{\omega \mp \omega_c + i\gamma}, \tag{12}$$

where n is the density, m is the mass, ω_c is the cyclotron frequency and γ is the scattering rate of the charge carriers. Using eqn. (11), we obtain the following effective

conductivity:

$$\sigma_{\text{eff},\pm}(\omega) = \frac{fne^2}{m}\frac{i}{\omega \mp \omega_c + i\gamma - \omega_0^2/\omega}, \tag{13}$$

which has a Lorentzian shape with a resonant energy given by:

$$\omega_0^2 = \frac{Cne^2}{md\kappa}. \tag{14}$$

One can see that the plasmon spectral weight, $D = \int_0^\infty \text{Re}\sigma_{xx}(\omega)d\omega = f\pi ne^2/2m$, in eqn. (13) is reduced with respect to the Drude weight in eqn. (12) by the filling factor.

Acknowledgements

I would especially like to thank the two people who gave me the possibility to start and complete my thesis, Alexey Kuzmenko and Dirk van der Marel. My years as a member of the Quantum Materials Group in Geneva were enriching, surprising at times and above all great fun. It has been the best learning opportunity I could have wished for.

The experience wouldn't have been so special and valuable without all my great (former) colleagues: Riccardo Tediosi, Erik van Heumen, Violeta Guritanu, Romain Viennois, Florence Levy, Dook van Mechelen, Jason Hancock, Verner Thorsmølle, Enrico Giannini, Jeremy Teyssier, Alberto Ubaldini, Julien Levallois, Ana Akrap, Nicolas Ubrig, Zhiwei Wang, Jacim Jacimovic, Iman Mirzaei, Michael Tran, Damien Stricker, Adrien Stucky, Julien Ruppen, Ievgeniia Nedoliuk, Davide Valentinis and Denise Borjon. Many thanks to all of you! And of course, thanks to Mehdi Brandt, Spiros Zanos and Roland Pellet for all the technical support and teaching me the practical sides of life in the lab.

Particularly important for my thesis were the people from outside of our group providing samples, experimental and theoretical expertise, encouragement and advice. Therefore, many thanks to: Marcus Ostler, Felix Fromm, Michl Kaiser, Thomas Seyller, Aaron Bostwick, Eli Rotenberg, Andrew Walter, Milan Orlita, Marek Potemski, Iaroslav Gaponenko and Jianing Chen.

Crucial for the successful completion of the thesis is the thesis committee. Thank you, Alberto Murpurgo, Andrei Pimenov and Francisco Guinea for agreeing to take part in the committee together with Alexey and Dirk. Many thanks for the nice comments and questions.

Surely the most important supporting role was played by Pieter. I want to thank you deeply for your everlasting patience and support, regardless the choices I made. Last, I would like to thank my parents and my brother for their support and enthusiasm throughout the years.

Many thanks to all of you
Iris

List of Publications

N. Ubrig, I. Crassee, J. Levallois, I. O. Nedoliuk, F. Fromm, M. Kaiser, T. Seyller, and A. B. Kuzmenko, "Fabry-Perot enhanced Faraday rotation in graphene", ArXiv e-prints 1303.1634 (2013), submitted.

M. Orlita, I. Crassee, C. Faugeras, A. B. Kuzmenko, F. Fromm, M. Ostler, T. Seyller, G. Martinez, M. Polini, and M. Potemski, "Classical to quantum crossover of the cyclotron resonance in graphene: a study of the strength of intraband absorption", New Journal of Physics **14**, 095008 (2012).

I. Crassee, M. Orlita, M. Potemski, A. L. Walter, M. Ostler, T. Seyller, I. Gaponenko, J. Chen, and A. B. Kuzmenko, "Intrinsic Terahertz Plasmons and Magnetoplasmons in Large Scale Monolayer Graphene", Nano Lett. **12**, 2470-2474 (2012).

J. L. M. van Mechelen, D. van der Marel, I. Crassee, and T. Kolodiazhnyi, "Spin Resonance in EuTiO3 Probed by Time-Domain Gigahertz Ellipsometry", Phys. Rev. Lett. **106**, 217601 (2011).

I. Crassee, J. Levallois, D. van der Marel, A. L.Walter, T. Seyller, and A. B. Kuzmenko, "Multicomponent magneto-optical conductivity of multilayer graphene on SiC", Phys. Rev. B **84**, 035103 (2011).

I. Crassee, J. Levallois, A. L. Walter, M. Ostler, A. Bostwick, E. Rotenberg, T. Seyller, D. van der Marel, and A. B. Kuzmenko, "Giant Faraday rotation in single- and multilayer graphene", Nature Phys. **7**, 48-51 (2011).

A. B. Kuzmenko, I. Crassee, D. van der Marel, P. Blake, and K. S. Novoselov, "Determination of the gate-tunable band gap and tight-binding parameters in bilayer graphene using infrared spectroscopy", Phys. Rev. B **80**, 165406 (2009).

A. B. Kuzmenko, L. Benfatto, E. Cappelluti, I. Crassee, D. van der Marel, P. Blake, K.

C. LIST OF PUBLICATIONS

S. Novoselov, and A. K. Geim, "Gate Tunable Infrared Phonon Anomalies in Bilayer Graphene", Phys. Rev. Lett. **103**, 116804 (2009).

Bibliography

[1] K. S. Novoselov, A. K. Geim, S. V. Morozov, D. Jiang, S. V. Dubonos, I. V. Grigorieva, and A. A. Firsov, "Electric Field Effect in Atomically Thin Carbon Films," Science **306,** 666–669 (2004).

[2] P. R. Wallace, "The Band Theory of Graphite," Phys. Rev. **71,** 622–634 (1947).

[3] C. Berger *et al.*, "Ultrathin Epitaxial Graphite: 2D Electron Gas Properties and a Route toward Graphene-based Nanoelectronics," The Journal of Physical Chemistry B **108,** 19912–19916 (2004).

[4] E. McCann and V. I. Fal'ko, "Landau-Level Degeneracy and Quantum Hall Effect in a Graphite Bilayer," Phys. Rev. Lett. **96,** 086805 (2006).

[5] E. McCann, "Asymmetry gap in the electronic band structure of bilayer graphene," Phys. Rev. B **74,** 161403 (2006).

[6] J. Nilsson, A. H. Castro Neto, F. Guinea, and N. M. R. Peres, "Transmission through a biased graphene bilayer barrier," Phys. Rev. B **76,** 165416 (2007).

[7] E. V. Castro, K. S. Novoselov, S. V. Morozov, N. M. R. Peres, J. M. B. L. dos Santos, J. Nilsson, F. Guinea, A. K. Geim, and A. H. C. Neto, "Biased Bilayer Graphene: Semiconductor with a Gap Tunable by the Electric Field Effect," Phys. Rev. Lett. **99,** 216802 (2007).

[8] T. Ohta, A. Bostwick, T. Seyller, K. Horn, and E. Rotenberg, "Controlling the Electronic Structure of Bilayer Graphene," Science **313,** 951–954 (2006).

[9] J. B. Oostinga, H. B. Heersche, X. Liu, A. F. Morpurgo, and L. M. K. Vandersypen, "Gate-induced insulating state in bilayer graphene devices," Nat Mater **7,** 151–157 (2008).

[10] L. A. Ponomarenko, F. Schedin, M. I. Katsnelson, R. Yang, E. W. Hill, K. S. Novoselov, and A. K. Geim, "Chaotic Dirac Billiard in Graphene Quantum Dots," Science **320,** 356–358 (2008).

[11] B. Wunsch, T. Stauber, F. Sols, and F. Guinea, "Dynamical polarization of graphene at finite doping," New Journal of Physics **8,** 318 (2006).

[12] E. H. Hwang and S. Das Sarma, "Dielectric function, screening, and plasmons in two-dimensional graphene," Phys. Rev. B **75,** 205418 (2007).

[13] S. A. Mikhailov and K. Ziegler, "New Electromagnetic Mode in Graphene," Phys. Rev. Lett. **99,** 016803 (2007).

[14] F. Rana, "Graphene Terahertz Plasmon Oscillators," Nanotechnology, IEEE Transactions on **7,** 91 –99 (2008).

[15] M. Jablan, H. Buljan, and M. Soljačić, "Plasmonics in graphene at infrared frequencies," Phys. Rev. B **80,** 245435 (2009).

[16] F. Xia, T. Mueller, Y.-m. Lin, A. Valdes-Garcia, and P. Avouris, "Ultrafast graphene photodetector," Nat Nano **4,** 839–843 (2009).

[17] F. Bonaccorso, Z. Sun, T. Hasan, and A. C. Ferrari, "Graphene photonics and optoelectronics," Nat Photon **4,** 611–622 (2010).

[18] Y. V. Bludov, M. I. Vasilevskiy, and N. M. R. Peres, "Mechanism for graphene-based optoelectronic switches by tuning surface plasmon-polaritons in monolayer graphene," EPL (Europhysics Letters) **92,** 68001 (2010).

[19] T. Echtermeyer, L. Britnell, P. Jasnos, A. Lombardo, R. Gorbachev, A. Grigorenko, A. Geim, A. Ferrari, and K. Novoselov, "Strong plasmonic enhancement of photovoltage in graphene," Nat Commun **2,** 458– (2011).

[20] L. Ju *et al.*, "Graphene plasmonics for tunable terahertz metamaterials," Nat Nano **6,** 630–634 (2011).

[21] F. H. L. Koppens, D. E. Chang, and F. J. Garcia de Abajo, "Graphene Plasmonics: A Platform for Strong Light Matter Interactions," Nano Letters **11,** 3370–3377 (2011).

[22] Z. Fei *et al.*, "Infrared Nanoscopy of Dirac Plasmons at the Graphene-SiO2 Interface," Nano Letters **11,** 4701–4705 (2011).

[23] A. Vakil and N. Engheta, "Transformation Optics Using Graphene," Science **332,** 1291–1294 (2011).

[24] A. Y. Nikitin, F. Guinea, F. J. Garcia-Vidal, and L. Martin-Moreno, "Fields radiated by a nanoemitter in a graphene sheet," Phys. Rev. B **84,** 195446 (2011).

[25] F. J. García de Abajo, "Graphene Nanophotonics," Science **339,** 917–918 (2013).

[26] J. W. McClure, "Band Structure of Graphite and de Haas-van Alphen Effect," Phys. Rev. **108,** 612–618 (1957).

[27] J. C. Slonczewski and P. R. Weiss, "Band Structure of Graphite," Phys. Rev. **109,** 272–279 (1958).

[28] G. W. Semenoff, "Condensed-Matter Simulation of a Three-Dimensional Anomaly," Phys. Rev. Lett. **53,** 2449–2452 (1984).

[29] F. D. M. Haldane, "Model for a Quantum Hall Effect without Landau Levels: Condensed-Matter Realization of the "Parity Anomaly"," Phys. Rev. Lett. **61,** 2015–2018 (1988).

[30] T. Ando, Y. Zheng, and H. Suzuura, "Dynamical Conductivity and Zero-Mode Anomaly in Honeycomb Lattices," Journal of the Physical Society of Japan **71,** 1318–1324 (2002).

[31] A. H. Castro Neto, F. Guinea, N. M. R. Peres, K. S. Novoselov, and A. K. Geim, "The electronic properties of graphene," Rev. Mod. Phys. **81,** 109–162 (2009).

[32] A. H. Castro Neto, F. Guinea, and N. M. R. Peres, "Edge and surface states in the quantum Hall effect in graphene," Phys. Rev. B **73,** 205408 (2006).

[33] M. I. Katsnelson, K. S. Novoselov, and A. K. Geim, "Chiral tunnelling and the Klein paradox inăgraphene," Nature Physics **2,** 620–625 (2006).

[34] M. Katsnelson and K. Novoselov, "Graphene: New bridge between condensed matter physics and quantum electrodynamics," Solid State Communications **143,** 3–13 (2007).

[35] A. Bostwick, T. Ohta, T. Seyller, K. Horn, and E. Rotenberg, "Quasiparticle dynamics in graphene," Nat Phys **3,** 36–40 (2007).

[36] S. Y. Zhou, G.-H. Gweon, A. V. Fedorov, P. N. First, W. A. de Heer, D.-H. Lee, F. Guinea, A. H. Castro Neto, and A. Lanzara, "Substrate-induced bandgap opening in epitaxial graphene," Nat Mater **6,** 770–775 (2007).

[37] V. P. Gusynin, S. G. Sharapov, and J. P. Carbotte, "Unusual Microwave Response of Dirac Quasiparticles in Graphene," Phys. Rev. Lett. **96,** 256802 (2006).

[38] A. B. Kuzmenko, E. van Heumen, F. Carbone, and D. van der Marel, "Universal Optical Conductance of Graphite," Phys. Rev. Lett. **100,** 117401 (2008).

[39] R. R. Nair, P. Blake, A. N. Grigorenko, K. S. Novoselov, T. J. Booth, T. Stauber, N. M. R. Peres, and A. K. Geim, "Fine Structure Constant Defines Visual Transparency of Graphene," Science **320,** 1308 (2008).

[40] K. F. Mak, M. Y. Sfeir, Y. Wu, C. H. Lui, J. A. Misewich, and T. F. Heinz, "Measurement of the Optical Conductivity of Graphene," Phys. Rev. Lett. **101,** 196405 (2008).

[41] F. Wang, Y. Zhang, C. Tian, C. Girit, A. Zettl, M. Crommie, and Y. R. Shen, "Gate-Variable Optical Transitions in Graphene," Science **320,** 206–209 (2008).

[42] Z. Q. Li, E. A. Henriksen, Z. Jiang, Z. Hao, M. C. Martin, P. Kim, H. L. Stormer, and D. N. Basov, "Dirac charge dynamics in graphene by infrared spectroscopy," Nat Phys **4,** 532–535 (2008).

[43] A. B. Kuzmenko, I. Crassee, D. van der Marel, P. Blake, and K. S. Novoselov, "Determination of the gate-tunable band gap and tight-binding parameters in bilayer graphene using infrared spectroscopy," Phys. Rev. B **80,** 165406 (2009).

[44] K. F. Mak, C. H. Lui, J. Shan, and T. F. Heinz, "Observation of an Electric-Field-Induced Band Gap in Bilayer Graphene by Infrared Spectroscopy," Phys. Rev. Lett. **102,** 256405 (2009).

[45] V. P. Gusynin and S. G. Sharapov, "Unconventional integer quantum Hall effect in graphene," Phys. Rev. Lett. **95,** 146801– (2005).

[46] N. M. R. Peres, F. Guinea, and A. H. Castro Neto, "Electronic properties of disordered two-dimensional carbon," Phys. Rev. B **73,** 125411 (2006).

[47] K. S. Novoselov, A. K. Geim, S. V. Morozov, D. Jiang, M. I. Katsnelson, I. V. Grigorieva, S. V. Dubonos, and A. A. Firsov, "Two-dimensional gas of massless Dirac fermions in graphene," Nature **438,** 197–200 (2005).

[48] Y. Zhang, Y.-W. Tan, H. L. Stormer, and P. Kim, "Experimental observation of the quantum Hall effect and Berry's phase in graphene," Nature **438,** 201–204 (2005).

[49] K. S. Novoselov, Z. Jiang, Y. Zhang, S. V. Morozov, H. L. Stormer, U. Zeitler, J. C. Maan, G. S. Boebinger, P. Kim, and A. K. Geim, "Room-Temperature Quantum Hall Effect in Graphene," Science **315,** 1379 (2007).

[50] G. Dresselhaus, A. F. Kip, and C. Kittel, "Cyclotron Resonance of Electrons and Holes in Silicon and Germanium Crystals," Phys. Rev. **98,** 368–384 (1955).

[51] T. Ando, "Theory of Cyclotron Resonance Lineshape in a Two-Dimensional Electron System," Journal of the Physical Society of Japan **38,** 989–997 (1975).

[52] M. Prasad and S. Fujita, "Comparison between the two theories of cyclotron resonance lineshape for a two-dimensional electron-impurity system," Solid State Communications **23,** 551 – 553 (1977).

[53] M. L. Sadowski, G. Martinez, M. Potemski, C. Berger, and W. A. de Heer, "Landau level spectroscopy of ultrathin graphite layers," Phys. Rev. Lett. **97,** 266405– (2006).

[54] Z. Jiang, E. A. Henriksen, L. C. Tung, Y.-J. Wang, M. E. Schwartz, M. Y. Han, P. Kim, and H. L. Stormer, "Infrared Spectroscopy of Landau Levels of Graphene," Phys. Rev. Lett. **98,** 197403 (2007).

[55] R. S. Deacon, K.-C. Chuang, R. J. Nicholas, K. S. Novoselov, and A. K. Geim, "Cyclotron resonance study of the electron and hole velocity in graphene monolayers," Phys. Rev. B **76,** 081406 (2007).

[56] G. Li and E. Y. Andrei, "Observation of Landau levels of Dirac fermions in graphite," Nat Phys **3,** 623–627 (2007).

[57] D. L. Miller, K. D. Kubista, G. M. Rutter, M. Ruan, W. A. de Heer, P. N. First, and J. A. Stroscio, "Observing the Quantization of Zero Mass Carriers in Graphene," Science **324,** 924–927 (2009).

[58] M. Orlita *et al.*, "Approaching the Dirac Point in High-Mobility Multilayer Epitaxial Graphene," Phys. Rev. Lett. **101,** 267601 (2008).

[59] M. Orlita, C. Faugeras, R. Grill, A. Wysmolek, W. Strupinski, C. Berger, W. A. de Heer, G. Martinez, and M. Potemski, "Carrier Scattering from Dynamical Magnetoconductivity in Quasineutral Epitaxial Graphene," Phys. Rev. Lett. **107,** 216603 (2011).

[60] M. Orlita, L. Z. Tan, M. Potemski, M. Sprinkle, C. Berger, W. A. de Heer, S. G. Louie, and G. Martinez, "Resonant Excitation of Graphene K-Phonon and Intra-Landau-Level Excitons in Magneto-Optical Spectroscopy," Phys. Rev. Lett. **108,** 247401 (2012).

[61] A. K. Geim, "Graphene: Status and Prospects," Science **324,** 1530–1534 (2009).

[62] B. C. Banerjee, T. J. Hirt, and P. L. Walker, "Pyrolytic Carbon Formation from Carbon Suboxide," Nature **192,** 450–451 (1961).

[63] P. R. Somani, S. P. Somani, and M. Umeno, "Planer nano-graphenes from camphor by CVD," Chemical Physics Letters **430,** 56 – 59 (2006).

[64] A. Obraztsov, E. Obraztsova, A. Tyurnina, and A. Zolotukhin, "Chemical vapor deposition of thin graphite films of nanometer thickness," Carbon **45,** 2017 – 2021 (2007).

[65] K. S. Kim, Y. Zhao, H. Jang, S. Y. Lee, J. M. Kim, K. S. Kim, J.-H. Ahn, P. Kim, J.-Y. Choi, and B. H. Hong, "Large-scale pattern growth of graphene films for stretchable transparent electrodes," Nature **457,** 706–710 (2009).

[66] X. Li *et al.*, "Large-Area Synthesis of High-Quality and Uniform Graphene Films on Copper Foils," Science **324,** 1312–1314 (2009).

[67] G. Brumfiel, "Nanotubes cut to ribbons," Nature News (2009).

[68] Y. Hernandez *et al.*, "High-yield production of graphene by liquid-phase exfoliation of graphite," Nature Nanotechnology **3,** 563–568 (2008).

[69] T. Seyller, A. Bostwick, K. V. Emtsev, K. Horn, L. Ley, J. L. McChesney, T. Ohta, J. D. Riley, E. Rotenberg, and F. Speck, "Epitaxial graphene: a new material," physica status solidi (b) **245,** 1436–1446 (2008).

[70] K. V. Emtsev, F. Speck, T. Seyller, L. Ley, and J. D. Riley, "Interaction, growth, and ordering of epitaxial graphene on SiC0001 surfaces: A comparative photoelectron spectroscopy study," Phys. Rev. B **77,** 155303 (2008).

[71] C. Riedl, C. Coletti, T. Iwasaki, A. A. Zakharov, and U. Starke, "Quasi-Free-Standing Epitaxial Graphene on SiC Obtained by Hydrogen Intercalation," Phys. Rev. Lett. **103,** 246804 (2009).

[72] F. Speck, M. Ostler, J. Röhrl, J. Jobst, D. Waldmann, M. Hundhausen, L. Ley, H. B. Weber, and T. Seyller, "Quasi-freestanding graphene on SiC(0001)," Mat. Sci. Forum **645-648,** 629–632 (2010).

[73] T. Ohta, A. Bostwick, J. L. McChesney, T. Seyller, K. Horn, and E. Rotenberg, "Interlayer Interaction and Electronic Screening in Multilayer Graphene Investigated with Angle-Resolved Photoemission Spectroscopy," Phys. Rev. Lett. **98,** 206802 (2007).

[74] C. Riedl, A. A. Zakharov, and U. Starke, "Precise in situ thickness analysis of epitaxial graphene layers on SiC(0001) using low-energy electron diffraction and angle resolved ultraviolet photoelectron spectroscopy," Applied Physics Letters **93,** 033106 (2008).

[75] K. V. Emtsev *et al.*, "Towards wafer-size graphene layers by atmospheric pressure graphitization of silicon carbide," Nature Mater. **8,** 203–207 (2009).

[76] S. Forti, K. V. Emtsev, C. Coletti, A. A. Zakharov, C. Riedl, and U. Starke, "Large-area homogeneous quasifree standing epitaxial graphene on SiC(0001): Electronic and structural characterization," Phys. Rev. B **84,** 125449 (2011).

[77] F. Schedin, A. K. Geim, S. V. Morozov, E. W. Hill, P. Blake, M. I. Katsnelson, and K. S. Novoselov, "Detection of individual gas molecules adsorbed on graphene," Nat Mater **6,** 652–655 (2007).

[78] T. Shen, J. J. Gu, M. Xu, Y. Q. Wu, M. L. Bolen, M. A. Capano, L. W. Engel, and P. D. Ye, "Observation of quantum-Hall effect in gated epitaxial graphene grown on SiC (0001)," Applied Physics Letters **95,** 172105 (2009).

[79] J. Jobst, D. Waldmann, F. Speck, R. Hirner, D. K. Maude, T. Seyller, and H. B. Weber, "Quantum oscillations and quantum Hall effect in epitaxial graphene," Phys. Rev. B **81,** 195434 (2010).

[80] K. S. Novoselov, E. McCann, S. V. Morozov, V. I. Fal'ko, M. I. Katsnelson, U. Zeitler, D. Jiang, F. Schedin, and A. K. Geim, "Unconventional quantum Hall effect and Berry/'s phase of 2[pi] in bilayer graphene," Nat Phys **2,** 177–180 (2006).

[81] E. A. Henriksen, Z. Jiang, L.-C. Tung, M. E. Schwartz, M. Takita, Y.-J. Wang, P. Kim, and H. L. Stormer, "Cyclotron Resonance in Bilayer Graphene," Phys. Rev. Lett. **100,** 087403 (2008).

[82] Y. J. Song *et al.*, "High-resolution tunnelling spectroscopy of a graphene quartet," Nature **467,** 185–189 (2010).

[83] C. Berger *et al.*, "Electronic Confinement and Coherence in Patterned Epitaxial Graphene," Science **312,** 1191–1196 (2006).

[84] X. Wu, X. Li, Z. Song, C. Berger, and W. A. de Heer, "Weak Antilocalization in Epitaxial Graphene: Evidence for Chiral Electrons," Phys. Rev. Lett. **98,** 136801 (2007).

[85] M. Sprinkle *et al.*, "First Direct Observation of a Nearly Ideal Graphene Band Structure," Phys. Rev. Lett. **103,** 226803 (2009).

[86] J. Hass, F. Varchon, J. E. Millán-Otoya, M. Sprinkle, N. Sharma, W. A. de Heer, C. Berger, P. N. First, L. Magaud, and E. H. Conrad, "Why Multilayer Graphene on $4H$-SiC$(000\bar{1})$ Behaves Like a Single Sheet of Graphene," Phys. Rev. Lett. **100,** 125504 (2008).

[87] F. Guinea, A. H. Castro Neto, and N. M. R. Peres, "Electronic states and Landau levels in graphene stacks," Phys. Rev. B **73,** 245426 (2006).

[88] J. M. B. Lopes dos Santos, N. M. R. Peres, and A. H. Castro Neto, "Graphene Bilayer with a Twist: Electronic Structure," Phys. Rev. Lett. **99,** 256802 (2007).

[89] S. Shallcross, S. Sharma, and O. A. Pankratov, "Quantum Interference at the Twist Boundary in Graphene," Phys. Rev. Lett. **101,** 056803 (2008).

[90] G. Trambly de Laissardière, D. Mayou, and L. Magaud, "Localization of Dirac Electrons in Rotated Graphene Bilayers," Nano Letters **10,** 804–808 (2010), pMID: 20121163.

[91] S. Shallcross, S. Sharma, E. Kandelaki, and O. A. Pankratov, "Electronic structure of turbostratic graphene," Phys. Rev. B **81,** 165105 (2010).

[92] E. J. Mele, "Commensuration and interlayer coherence in twisted bilayer graphene," Phys. Rev. B **81,** 161405 (2010).

[93] R. Bistritzer and A. H. MacDonald, "Transport between twisted graphene layers," Phys. Rev. B **81,** 245412 (2010).

[94] R. Bistritzer and A. H. MacDonald, "Moiré butterflies in twisted bilayer graphene," Phys. Rev. B **84,** 035440 (2011).

[95] A. Luican, G. Li, A. Reina, J. Kong, R. R. Nair, K. S. Novoselov, A. K. Geim, and E. Y. Andrei, "Single-Layer Behavior and Its Breakdown in Twisted Graphene Layers," Phys. Rev. Lett. **106,** 126802 (2011).

[96] M. Suzuki, K. Fujii, T. Ohyama, H. Kobori, and N. Kotera, "Far-Infrared Resonant Faraday Effect in Semiconductors," Journal of the Physical Society of Japan **72,** 3276–3285 (2003).

[97] L. Yang, J. Deslippe, C.-H. Park, M. L. Cohen, and S. G. Louie, "Excitonic Effects on the Optical Response of Graphene and Bilayer Graphene," Phys. Rev. Lett. **103,** 186802 (2009).

[98] S. H. Abedinpour, G. Vignale, A. Principi, M. Polini, W.-K. Tse, and A. H. MacDonald, "Drude weight, plasmon dispersion, and ac conductivity in doped graphene sheets," Phys. Rev. B **84,** 045429 (2011).

[99] J. Horng *et al.*, "Drude conductivity of Dirac fermions in graphene," Phys. Rev. B **83,** 165113 (2011).

[100] H. Yan, F. Xia, W. Zhu, M. Freitag, C. Dimitrakopoulos, A. A. Bol, G. Tulevski, and P. Avouris, "Infrared Spectroscopy of Wafer-Scale Graphene," ACS Nano **5,** 9854–9860 (2011).

[101] M. Dressel and G. Grüner, *Electrodynamics of solids: Optical Properties of Electrons in Matter* (Cambridge University Press, 2002).

[102] F. Wooten, *Optical Properties of Solids* (Academic Press, 1972).

[103] E. van Heumen and D. van der Marel, "Lectures On The Physics Of Strongly Correlated Systems XI: Eleventh Training course in the Physics of Strongly Correlated systems," AIP Conference Proceedings 918 (2006).

[104] M. Born and E. Wolf, *Principles of Optics: Electromagnetic Theort of Propagation, Intereference and Diffraction of Light* (Cambridge University Press, 1999).

[105] L. Onsager, "Reciprocal Relations in Irreversible Processes. II.," Phys. Rev. **38,** 2265–2279 (1931).

[106] P. M. Oppeneer, in *Handbook of Magnetic Material*, K. H. J. Buschow, ed., (Alsevier, 2001).

[107] W. P. Healy, "Dispersion Relations for Optically Active Media," American Journal of Physics **42,** 1070 (1974).

[108] D. Y. Smith, "Superconvergence and sum rules for the optical constants: Natural and magneto-optical activity," Phys. Rev. B **13,** 5303–5315 (1976).

[109] J. Kunes and P. M. Oppeneer, "Exact many-body sum rule for the magneto-optical spectrum of solids," Phys. Rev. B **61,** 15774–15777 (2000).

[110] Bruker, "Bruker FT-IR spectrometers,".

[111] CryogenLimited, "7 Tesla split coil magnet,".

[112] B. J. Feenstra, Ph.D. thesis, Rijksuniversiteit Groningen, 1997.

[113] M. Faraday, "On the magnetization of light and the illumination of magnetic lines of force," Phil. Trans. R. Soc. **136,** 104–123 (1846).

[114] J. L. M. van Mechelen, D. van der Marel, I. Crassee, and T. Kolodiazhnyi, "Spin Resonance in $\mathrm{EuTiO_3}$ Probed by Time-Domain Gigahertz Ellipsometry," Phys. Rev. Lett. **106,** 217601 (2011).

[115] N. Ubrig, I. Crassee, J. Levallois, I. O. Nedoliuk, F. Fromm, M. Kaiser, T. Seyller, and A. B. Kuzmenko, "Fabry-Perot enhanced Faraday rotation in graphene," ArXiv e-prints (2013).

[116] A. A. Balandin, S. Ghosh, W. Bao, I. Calizo, D. Teweldebrhan, F. Miao, and C. N. Lau, "Superior Thermal Conductivity of Single-Layer Graphene," Nano Letters **8,** 902–907 (2008), pMID: 18284217.

[117] J. W. McClure, "Diamagnetism of Graphite," Phys. Rev. **104,** 666–671 (1956).

[118] M. V. Berry, "Quantal Phase Factors Accompanying Adiabatic Changes," Proceedings of the Royal Society of London. A. Mathematical and Physical Sciences **392,** 45–57 (1984).

[119] A. B. Fowler, F. F. Fang, W. E. Howard, and P. J. Stiles, "Magneto-Oscillatory Conductance in Silicon Surfaces," Phys. Rev. Lett. **16,** 901–903 (1966).

[120] A. K. Geim and K. S. Novoselov, "The rise of graphene," Nature Mater. **6,** 183–191 (2007).

[121] L. A. Falkovsky and A. A. Varlamov, "Space-time dispersion of graphene conductivity," Eur. Phys. J. B **56,** 281–284 (2007).

[122] V. P. Gusynin, S. G. Sharapov, and J. P. Carbotte, "On the universal AC optical background in graphene," New J. Phys. **11,** 095013– (2009).

[123] V. G. Kravets, A. N. Grigorenko, R. R. Nair, P. Blake, S. Anissimova, K. S. Novoselov, and A. K. Geim, "Spectroscopic ellipsometry of graphene and an exciton-shifted van Hove peak in absorption," Phys. Rev. B **81,** 155413 (2010).

[124] K. F. Mak, J. Shan, and T. F. Heinz, "Seeing Many-Body Effects in Single- and Few-Layer Graphene: Observation of Two-Dimensional Saddle-Point Excitons," Phys. Rev. Lett. **106,** 046401 (2011).

[125] G. Abstreiter, P. Kneschaurek, J. P. Kotthaus, and J. F. Koch, "Cyclotron Resonance of Electrons in an Inversion Layer on Si," Phys. Rev. Lett. **32,** 104–107 (1974).

[126] S. J. Allen, D. C. Tsui, and J. V. Dalton, "Far-Infrared Cyclotron Resonance in the Inversion Layer of Silicon," Phys. Rev. Lett. **32,** 107–110 (1974).

[127] V. P. Gusynin, S. G. Sharapov, and J. P. Carbotte, "Magneto-optical conductivity in graphene," J. Phys. Condens. Matter **19,** 026222– (2007).

[128] X. Wu, Y. Hu, M. Ruan, N. K. Madiomanana, J. Hankinson, M. Sprinkle, C. Berger, and W. A. de Heer, "Half integer quantum Hall effect in high mobility single layer epitaxial graphene," Applied Physics Letters **95,** 223108 (2009).

[129] M. O. Goerbig, "Electronic properties of graphene in a strong magnetic field," Rev. Mod. Phys. **83,** 1193–1243 (2011).

[130] N. W. Ashcroft and N. D. Mermin, *Solid State Physics* (Harcourt College Publishers, 1976).

[131] D. S. L. Abergel and V. I. Fal'ko, "Optical and magneto-optical far-infrared properties of bilayer graphene," Phys. Rev. B **75,** 155430 (2007).

[132] V. P. Gusynin, S. G. Sharapov, and J. P. Carbotte, "Anomalous Absorption Line in the Magneto-Optical Response of Graphene," Phys. Rev. Lett. **98,** 157402 (2007).

[133] A. Ferreira, J. Viana-Gomes, Y. V. Bludov, V. Pereira, N. M. R. Peres, and A. H. Castro Neto, "Faraday effect in graphene enclosed in an optical cavity and the equation of motion method for the study of magneto-optical transport in solids," Phys. Rev. B **84,** 235410 (2011).

[134] C. R. Dean *et al.*, "Boron nitride substrates for high-quality graphene electronics," Nat Nano **5,** 722–726 (2010).

[135] Y. y. Wang, Z. h. Ni, T. Yu, Z. X. Shen, H. m. Wang, Y. h. Wu, W. Chen, and A. T. Shen Wee, "Raman Studies of Monolayer Graphene: The Substrate Effect," The Journal of Physical Chemistry C **112,** 10637–10640 (2008).

[136] W. A. de Heer *et al.*, "Epitaxial graphene," Solid State Communications **143,** 92 – 100 (2007).

[137] A. Tzalenchuk, S. Lara-Avila, A. Kalaboukhov, S. Paolillo, M. Syvajarvi, R. Yakimova, O. Kazakova, J. J. B. M., V. Fal'ko, and S. Kubatkin, "Towards a quantum resistance standard based on epitaxial graphene," Nat Nano **5,** 186–189 (2010).

[138] I. Crassee, J. Levallois, A. L. Walter, M. Ostler, A. Bostwick, E. Rotenberg, T. Seyller, D. van der Marel, and A. B. Kuzmenko, "Giant Faraday rotation in single- and multilayer graphene," Nat Phys **7,** 48–51 (2011).

[139] V. A. Volkov and S. A. Mikhailov, "Quantization of the Faraday-effect in systems with a quantum Hall-effect," JETP Lett. **41,** 476–478– (1985).

[140] T. Morimoto, Y. Hatsugai, and H. Aoki, "Optical Hall Conductivity in Ordinary and Graphene Quantum Hall Systems," Phys. Rev. Lett. **103,** 116803 (2009).

[141] I. V. Fialkovsky and D. V. Vassilevich, "Parity-odd effects and polarization rotation in graphene," J. Phys. A **42,** 442001– (2009).

[142] Y. Ikebe, T. Morimoto, R. Masutomi, T. Okamoto, H. Aoki, and R. Shimano, "Optical Hall Effect in the Integer Quantum Hall Regime," Phys. Rev. Lett. **104,** 256802 (2010).

[143] I. Crassee, M. Orlita, M. Potemski, A. L. Walter, M. Ostler, T. Seyller, I. Gaponenko, J. Chen, and A. B. Kuzmenko, "Intrinsic Terahertz Plasmons and Magnetoplasmons in Large Scale Monolayer Graphene," Nano Lett. **12,** 2470–2474 (2012).

[144] H. Yan, X. Li, B. Chandra, G. Tulevski, Y. Wu, M. Freitag, W. Zhu, P. Avouris, and F. Xia, "Tunable infrared plasmonic devices using graphene/insulator stacks," Nat Nano **7,** 330–334 (2012).

[145] S. J. Allen, D. C. Tsui, and R. A. Logan, "Observation of the Two-Dimensional Plasmon in Silicon Inversion Layers," Phys. Rev. Lett. **38,** 980–983 (1977).

[146] S. J. Allen, H. L. Störmer, and J. C. M. Hwang, "Dimensional resonance of the two-dimensional electron gas in selectively doped GaAs/AlGaAs heterostructures," Phys. Rev. B **28,** 4875–4877 (1983).

[147] D. Heitmann, K. Kern, T. Demel, P. Grambow, K. Ploog, and Y. Zhang, "Spectroscopy of quantum dots and antidots," Surface Science **267,** 245 – 252 (1992).

[148] I. V. Kukushkin, J. H. Smet, S. A. Mikhailov, D. V. Kulakovskii, K. von Klitzing, and W. Wegscheider, "Observation of Retardation Effects in the Spectrum of Two-Dimensional Plasmons," Phys. Rev. Lett. **90,** 156801 (2003).

[149] S.-H. Ji, J. B. Hannon, R. M. Tromp, V. Perebeinos, J. Tersoff, and F. M. Ross, "Atomic-scale transport in epitaxial graphene," Nat Mater **11,** 114–119 (2012).

[150] C. Dimitrakopoulos, A. Grill, T. J. McArdle, Z. Liu, R. Wisnieff, and D. A. Antoniadis, "Effect of SiC wafer miscut angle on the morphology and Hall mobility of epitaxially grown graphene," Applied Physics Letters **98,** 222105–222105–3 (2011).

[151] Z. G. Cambaz, G. Yushin, S. Osswald, V. Mochalin, and Y. Gogotsi, "Noncatalytic synthesis of carbon nanotubes, graphene and graphite on SiC," Carbon **46,** 841 – 849 (2008).

[152] N. Camara, J.-R. Huntzinger, G. Rius, A. Tiberj, N. Mestres, F. Pérez-Murano, P. Godignon, and J. Camassel, "Anisotropic growth of long isolated graphene ribbons on the C face of graphite-capped $6H$-SiC," Phys. Rev. B **80,** 125410 (2009).

[153] B. Sepulveda, J. B. Gonzalez-Diaz, A. Garcia-Martin, L. M. Lechuga, and G. Armelles, "Plasmon-Induced Magneto-Optical Activity in Nanosized Gold Disks," Phys. Rev. Lett. **104,** 147401 (2010).

[154] D. B. Mast, A. J. Dahm, and A. L. Fetter, "Observation of Bulk and Edge Magnetoplasmons in a Two-Dimensional Electron Fluid," Phys. Rev. Lett. **54,** 1706–1709 (1985).

[155] D. C. Glattli, E. Y. Andrei, G. Deville, J. Poitrenaud, and F. I. B. Williams, "Dynamical Hall Effect in a Two-Dimensional Classical Plasma," Phys. Rev. Lett. **54,** 1710–1713 (1985).

[156] A. L. Fetter, "Edge magnetoplasmons in a bounded two-dimensional electron fluid," Phys. Rev. B **32,** 7676–7684 (1985).

[157] S. A. Mikhailov, "Radiative decay of collective excitations in an array of quantum dots," Phys. Rev. B **54,** 10335–10338 (1996).

[158] J. Perruisseau-Carrier, "Graphene for Antenna Applications: Opportunities and Challenges from Microwaves to THz," arXiv:1210.3444 (2012).

[159] M. Orlita and M. Potemski, "Dirac electronic states in graphene systems: optical spectroscopy studies," Semiconductor Science and Technology **25,** 063001 (2010).

[160] R. P. Leavitt and J. W. Little, "Absorption and emission of radiation by plasmons in two-dimensional electron-gas disks," Phys. Rev. B **34,** 2450–2457 (1986).

[161] I. Romero, J. Aizpurua, G. W. Bryant, and F. J. G. D. Abajo, "Plasmons in nearly touching metallic nanoparticles: singular response in the limit of touching dimers," Opt. Express **14,** 9988–9999 (2006).

[162] J. B. Lassiter, J. Aizpurua, L. I. Hernandez, D. W. Brandl, I. Romero, S. Lal, J. H. Hafner, P. Nordlander, and N. J. Halas, "Close Encounters between Two Nanoshells," Nano Letters **8,** 1212–1218 (2008), pMID: 18345644.

[163] A. Y. Nikitin, F. Guinea, F. J. Garcia-Vidal, and L. Martin-Moreno, "Surface plasmon enhanced absorption and suppressed transmission in periodic arrays of graphene ribbons," Phys. Rev. B **85,** 081405 (2012).

[164] S. A. Mikhailov, "Nonlinear cyclotron resonance of a massless quasiparticle in graphene," Phys. Rev. B **79,** 241309 (2009).

[165] C.-H. Park, F. Giustino, M. L. Cohen, and S. G. Louie, "Electron-Phonon Interactions in Graphene, Bilayer Graphene, and Graphite," Nano Letters **8,** 4229–4233 (2008).

[166] J. P. Carbotte, E. J. Nicol, and S. G. Sharapov, "Effect of electron-phonon interaction on spectroscopies in graphene," Phys. Rev. B **81,** 045419 (2010).

[167] V. Bonanni, S. Bonetti, T. Pakizeh, Z. Pirzadeh, J. Chen, J. Nogués, P. Vavassori, R. Hillenbrand, J. Akerman, and A. Dmitriev, "Designer Magnetoplasmonics with Nickel Nanoferromagnets," Nano Letters **11,** 5333–5338 (2011).

[168] I. Crassee, J. Levallois, D. van der Marel, A. L. Walter, T. Seyller, and A. B. Kuzmenko, "Multicomponent magneto-optical conductivity of multilayer graphene on SiC," Phys. Rev. B **84,** 035103 (2011).

[169] J. Schliemann, "Cyclotron motion in graphene," New Journal of Physics **10,** 043024 (2008).

[170] A. M. Witowski, M. Orlita, R. Stępniewski, A. Wysmołek, J. M. Baranowski, W. Strupiński, C. Faugeras, G. Martinez, and M. Potemski, "Quasiclassical cyclotron resonance of Dirac fermions in highly doped graphene," Phys. Rev. B **82,** 165305 (2010).

[171] J. Martin, N. Akerman, G. Ulbricht, T. Lohmann, J. H. Smet, K. v. Klitzing, and A. Yacoby, "Observation of electron-hole puddles in graphene using a scanning single-electron transistor," Nature Physics **4,** 144–148 (2008).

[172] T. Stauber, N. M. R. Peres, and A. K. Geim, "Optical conductivity of graphene in the visible region of the spectrum," Phys. Rev. B **78,** 085432 (2008).

[173] Z. Fei, Y. Shi, L. Pu, F. Gao, Y. Liu, L. Sheng, B. Wang, R. Zhang, and Y. Zheng, "High-energy optical conductivity of graphene determined by reflection contrast spectroscopy," Phys. Rev. B **78,** 201402 (2008).

[174] M. van Schilfgaarde and M. I. Katsnelson, "First-principles theory of nonlocal screening in graphene," Phys. Rev. B **83,** 081409 (2011).

[175] D. Heitmann and J. P. Kotthaus, "The Spectroscopy of Quantum Dot Arrays," Physics Today **46,** 56–63 (1993).

[176] M. Orlita, I. Crassee, C. Faugeras, A. B. Kuzmenko, F. Fromm, M. Ostler, T. Seyller, G. Martinez, M. Polini, and M. Potemski, "Classical to quantum crossover of the cyclotron resonance in graphene: a study of the strength of intraband absorption," New Journal of Physics **14,** 095008 (2012).

[177] P. N. First, W. A. de Heer, T. Seyller, C. Berger, J. A. Stroscio, and J.-S. Moon, "Epitaxial Graphenes on Silicon Carbide," MRS Bulletin **35,** 296–305 (2010).

[178] Y.-M. Lin *et al.*, "Multicarrier transport in epitaxial multilayer graphene," Applied Physics Letters **97,** 112107 (2010).

[179] A. B. Kuzmenko, "Kramers–Kronig constrained variational analysis of optical spectra," Review of Scientific Instruments **76,** 083108 (2005).